Electrical Properties of Rocks

By

Tariq Eamon Mohammed

A thesis submitted in partial fulfillment of the requirements for the degree of

Doctor of Philosophy

in

Geophysics

Department of Physics

University of Alberta

Abstract

The electrical conductivity of fluid-saturated porous sediments is influenced by a variety factors such as fractures, texture, and clay content whose behavior, in turn, depends on conditions of saturation, pressure, and temperature. This work attempts to provide new insights on the effect of some of these factors on electrical properties through novel controlled laboratory measurements on natural and artificial sediments; specifically examining three related aspects. First, do pressure-dependent changes in resistivity and velocity correlate with each other and can they be jointly modeled? Second, to what degree does an isolated fracture within an isotropic porous material affect the electrical conductivity anisotropy, and subsequently are such fractures likely to be detectable by electrical measurements in the field? Finally, what factors control the frequency dependent complex conductivity in porous sands containing small amounts of clay? Unique laboratory tests were developed to answer these questions. In the first, the electrical conductivities and ultrasonic wave speeds were measured as functions of confining and pore pressure through two rock samples of differing compressibilities Pressure-dependent variations in velocity and resistivity correlated well in the compressible sample suggesting both data can be jointly used to make inferences on the nature of the porosity in the material. In the second experiment, a new procedure to construct a porous sample containing a single, small aperture fractures was conceived. The electrical anisotropy of these samples was measured revealing that it strongly correlated ($r = 0.94$) with the relative fracture porosity. However, the samples were only weakly anisotropic (2% to 10%) suggesting that this effect may not readily be detected under actual field conditions. For the third experiment, complex resistivities were measured from 0.01 Hz to 100 Hz on porous mixtures of natural clays and glass beads. The characteristic relaxation times derived from the observed imaginary component correlated strongly with the diameters of the glass beads and were

not related to the physical properties of the different clay materials used. This, taken together with the fact that the clay-free glass bead samples displayed no dispersion provides evidence that membrane polarization dominates over Stern-layer polarization.

Preface

This thesis submitted for the degree of Doctor of Philosophy in Geophysics at the University of Alberta.

A version of chapter 2 is in preparation for submission to a peer reviewed journal. The laboratory work for this chapter was done jointly with Simon Gonzalez-Sirois from the Institute National de al Researche Scientifique (INRS). I was responsible for the modeling, scripting and manuscript development. Dr. Schmitt was the supervisory author and assisted with manuscript preparation and concept formation

A version of chapter 3 is in preparation for submission to the Journal of Applied Geophysics. I was responsible for the laboratory work, data analysis and manuscript preparation. Dr. Schmitt was the supervisory author and assisted with manuscript preparation and concept formation

A version of chapter 4 is in preparation for submission to Geophysics. I was responsible for the laboratory work and curve fitting. Dr. Schmitt was the supervisory author and assisted with manuscript preparation and concept formation

Acknowledgements

I would like to thank my supervisor for his continued support and patience throughout my research and writing. I have never felt under any pressure by him and was given the freedom to explore my own research interests as they arose and changed. I would like to thank all the people I have shared the EGG lab with over the years, of whom there are too many to give a full list. Your company, conversation and advice were always appreciated. I would especially like to thank Randy Kofman who was always available to help in a number of different ways. I would also like to thank my parents and girlfriend for their continued support.

I would finally like to thank the various funders who made this project possible including Carbon Management Canada (CMC) and Natural Sciences and Engineering Research Council (NSERC).

Contents

Abstract ii
Preface iv
Acknowledgements v
List of Tables ix
List of Figures xi
List of Symbols xviii
Chapter 1 1
Introduction 1
1.1) Background 1
1.2) Contributions 5
1.3) Thesis outline 7
Chapter 2 10
Constraint of crack properties in rocks by joint inversion of ultrasonic and electrical laboratory measurements. 10
2.1) Introduction 10
2.2) Background 14
2.2.1) Effective pressure 14
2.2.2) Pressure dependence of wave velocities 16
2.2.3) Pressure dependent electrical conductivities 19
2.3) Experimental set up 25
2.3.1) Ultrasonic measurements 26
2.3.2) Electrical measurements 27
2.3.3) Sample Description 30
2.4) Experimental procedure 32
2.4.1) Dry measurements 32
2.4.2) Saturated measurements 32
2.5) Results 33
2.5.1) Inversion Implementation 37
2.5.2) Inversion results 40
2.6) Discussion 46
2.7) Conclusions 56

2.8) Appendix 57
Chapter 3 71
Preliminary experiments towards understanding the influence of fractures on the anisotropy of electrical conductivity 71
3.1) Introduction 71
3.2) Theory 75
3.3) Experimental method 78
3.3.1) Synthetic samples 78
3.3.2) Conductivity Measurements 86
3.4) Results 90
3.4.1) Absolute conductivity variation 92
3.4.2) Anisotropy ratios 93
3.5) Discussion 96
3.6) Conclusions 98
3.7) References 100
Chapter 4 103
Induced polarization in artificial sediments 103
4.1) Introduction 103
4.2) Background 105
4.2.1) Electric Double Layer (EDL) 108
4.2.2) Models 110
4.2.3) Characteristic Spectra 114
4.2.4) Spectra Decomposition 116
4.2.5) Previous work 118
4.3) Methods 121
4.3.1) Sample construction 126
4.3.2) Debye Decomposition 130
4.4) Results 134
4.5) Discussion 143
4.5.1) Membrane polarization models 144
4.5.2) Stern layer polarization models 148
4.5.3) Comparison to Experimental results 149
4.6) Conclusion 151

Appendix 153
4.7) References 158
Chapter 5 162
Conclusions and directions for future research 162
5.1) Contributions of Work Described Here 162
5.2) Suggestions for Future Research 163
5.3) Bibliography 165

List of Tables

Table 2.1. Petrophysical properties of 2 samples used in this study

Table 2.2. Summary of inversions carried out on different data

Table 2.3. Summary of parameters obtained for results shown in Figs. 2.9 and 2.13.

Table 2.A1- Measured velocity and resistivities for saturated samples at various confining pressure and pore pressure. Note Cycle indicates weather the Pore pressure was being increased (up) or decreased (down) during the run.

Table 2.A2- Dry rock velocities measured for Berea Sandstone and the alumina ceramic

Table 3.1. Geometries of the constructed samples

Table 3.2. Observed conductivities for measurements taken parallel and perpendicular to the fracture strike. The average anisotropy ratio is the average of the individual ratios that can be calculated from the individual measurements.

Table 3.3. Summary of formation factors (F), cementation exponents (m) and tortuosities (τ) in parallel and perpendicular directions

Table 4.1. Characteristics of clay samples employed

Table 4.2. Summary table for samples measured in this work. Glass beads diameter ranges are 0.420 - 0.841 mm for #1, 0.074 - 0.125 mm for #2.

Table 4.3. Summary of the relaxation times obtained from hand picking and from fitting real and imaginary spectra.

Table 4.A1. Measured in-phase and quadrature resistivities at various frequencies for sample S1

Table 4.A2. Measured in-phase and quadrature resistivities at various frequencies for sample S2
Table 4.A3. Measured in-phase and quadrature resistivities at various frequencies for sample S3
Table 4.A4. Measured in-phase and quadrature resistivities at various frequencies for sample S4
Table 4.A5. Measured in-phase and quadrature resistivities at various frequencies for sample S5
Table 4.A6. Measured in-phase and quadrature resistivities at various frequencies for sample S6
Table 4.A7. Measured in-phase and quadrature resistivities at various frequencies for sample S7
Table 4.A8. Measured in-phase and quadrature resistivities at various frequencies for sample S8

List of Figures

Figure 2.1. a) Hypothetical crack-like porosity within the rock mass showing two points of contact. b) Composite topographic representation of the cracks (after Brown and Scholz, 1985), c) Reduction of the composite topography to representative half-spheres. As the crack closes at higher pressure more asperity spheres will be in contact with the overlying elastic half-space.

Figure 2.2. Schematic of fracture geometry to describe conduction through a cross section of fractured rock. (Following Stesky (1986)). A is the cross-sectional area of the cylinder normal to its axis. L is the axial length. a and w are the aperture and width of the fracture respectively. J is the current density vector.

Figure 2.3. a) Experimental set up for electrical resistivity and ultrasonic wave velocity measurements in a pressure vessel. b) Measurement circuit used for electrical resistivity measurement

Figure 2.4. Filtered waveform from ultrasonic velocity measurement with an arrow indicating arrival time determination.

Figure 2.5. Impedance magnitude as a function of frequency for multiple 2 electrode measurements and a single 4 electrode measurement on a ceramic sample.

Figure 2.6. Samples used in the laboratory tests. a) sintered alumina. b) Berea sandstone. Canadian ten cent coin with 18.03 mm diameter for scale.

Figure 2.7. P and S-wave velocities as a function of confining pressure under dry conditions for a) Berea sandstone and b) alumina ceramic

Figure 2.8. a) Saturated P- wave velocities, b) saturated S-wave velocities, and c) saturated electrical resistivity as a function of differential pressure for all confining pressure runs.

Figure 2.9. Berea sandstone comparison of measured results to modeled results for (a) P wave velocities under dry and saturated conditions, (b) S wave velocities under dry and saturated conditions and (c) electrical resistivity for measurements under saturated conditions.

Figure 2.10 Alumina ceramic comparison of measured results to modeled results for (a) P wave velocities under dry and saturated conditions, (b) S wave velocities under dry and saturated conditions and (c) electrical resistivity for measurements under saturated conditions.

Figure 2.11. Berea sandstone comparison of measured results to modeled results for (a) P wave velocities under dry and saturated conditions and (b) S wave velocities under dry and saturated conditions.

Figure 2.12. Berea sandstone comparison of Modeled to measured P electrical resistivity under saturated conditions.

Figure 2.13. M_e distributions when inverting (a) velocity data, (b) conductivity data and (c) both velocity and conductivity data. Histograms were calculated from the 400 inversions done for each dataset.

Figure 2.14 φ_c distributions when inverting (a) velocity data, (b) conductivity data and (c) both velocity and conductivity data. Histograms were calculated from the 400 inversions done for each dataset.

Figure 2,15 n distributions when inverting (a)velocity data, (b) conductivity data and (c) both velocity and conductivity data. Histograms were calculated from the 400 inversions done for each dataset.

Figure 2.16 B_e distributions when inverting (a) velocity data and (b) velocity and conductivity data. Histograms were calculated from the 400 inversions done for each dataset.

Figure 2.17 K_0 distributions when inverting (a) velocity data and (b) both velocity and conductivity data. Histograms were calculated from the 400 inversions done for each dataset.

Figure 2.18 μ_0 distributions when inverting (a) velocity data and (b) both velocity and conductivity data. Histograms were calculated from the 400 inversions done for each dataset.

Figure 2.19. p distributions when inverting (a) conductivity data and (b) both velocity and conductivity data. Histograms were calculated from the 400 inversions done for each dataset.

Figure 3.1. Illustration of the effect of cracks on flow paths Le shows the usual path current would have to travel, and L_{int} shows the length of that path that is short circuited by the crack.

Figure 3.2. Result of simulation on a circular cross-section with colour bar indicating Electric potential. Electrodes are shown in brown with red arrows indicating the direction of current density vectors.

Figure 3.3. Simplified sample geometry containing a) single crack, and b) two separated cracks.

Figure 3.4. Photograph of a broken and cleaved sample showing clear fracture surface alongside an intact sample. Canadian quarter with 23.81 mm diameter for scale.

Figure 3.5. Sample total porosity versus the glass bead: epoxy mass mixing ratio.

Figure 3.6. Experimental configuration consisting of sample shown oriented parallel to current flow between two strap-electrodes mounted in acrylic blocks. The clamp pushes the electrodes against the sample.

Figure 3.7. Photograph of acrylic blocks and copper electrodes. Canadian quarter with 23.81 mm diameter for scale.

Figure 3.8. 1/F variation with porosity. Archie's law plotted for m=1.5 and m=2.

Figure 3.9. Anisotropy ratio as a function of crack porosity/total porosity ratio. Line of best fits excludes the outlier datapoint. Error bars are shown in grey.

Figure 3.10. Change in the inverse formation factor (difference between 1/F in the two measurement directions) vs crack porosity.

Figure 4.1. (a) Formation of electrical double layer at and near the mineral surface. Stern layer immediately adjacent to mineral surface in dark green. Diffuse layer shown as lighter shaded green area. Bulk electrolyte as grey region. (b) In the region between the mineral grains (i.e. the pore throat), the Stern layers are disconnected but the diffuse layers overlap and would be continuous throughout the porous medium. (c) Two polarisation mechanisms at work under an applied electric field. The Stern layer polarisation occurring simultaneously with membrane polarisation as clay counterions are displaced as current flows through the narrow pore throat.

Figure 4.2. a) Simplified microscopic cross-section through a porous rock with solid portions in grey, surface charge layers in orange and electrolyte liquid (blue) saturated pore space. b) Equivalent circuit for the rock in which the overall complex conductivity $\sigma^*(\omega)$ consists of parallel conductive pathways through the electrolyte liquid and along grain boundaries. The rock mass in grey is considered to be insulating.

Figure 4.3. End member responses for different distribution of length scales. See text for details.

Figure 4.4. In-phase (solid line) and quadrature (dotted line) resistivity spectrum of a material with a single Debye characteristic relaxation relaxation time $\tau_c = 1/2\pi f_p$.

Figure 4.5. a) Simplified diagram of the experimental 4-electrode configuration with the sample (black) sandwiched between two saline buffers that inject current. The voltage difference is measured by a lock in amplifier between the two red electrodes separated a distance L axially along the sample. The constant current source is connected to the lock in amplifier to provide phase references. The various impedances that need to be considered include those for the current electrodes including the saline buffer Z_C, the lock-in-amplifier Z_I, the voltage electrodes Z_V. the portions of the sample between the saline buffers and the voltage electrodes Z_{IV}, and the desired sample impedance Z_S. b) Simplified equivalent circuit showing the arrangement of the expected impedances in the system.

Figure 4.6. (a) Phase spectrum for two water samples with different conductivities. (b) Phase spectra of clay-free glass bead packs.

Figure 4.7. SEM image of a sample constructed using a mixture of glass beads with varying sizes and 10% clay by weight.

Figure 4.8- Cole-Cole diagram for sample S5 showing Debye and Cole-Cole models for comparison.

Figure 4.9. Data and Debye decomposition result for samples incorporating clay 1. (a) In-phase resistivity spectrum for sample using larger glass beads. (b) Quadrature resistivity spectrum for sample using larger glass beads. (c) Relaxation time distribution for sample using larger glass beads. (d) In-phase resistivity spectrum for sample using smaller glass beads. (e) Quadrature

resistivity spectrum for sample using smaller glass beads. (f) Relaxation time distribution for sample using smaller glass beads. Arrow indicates the location of the “hand picked” characteristic frequency.

Figure 4.10. Data and Debye decomposition result for samples incorporating clay 2 (a) In-phase resistivity spectrum for sample using larger glass beads. (b) Quadrature resistivity spectrum for sample using larger glass beads. (c) Relaxation time distribution for sample using larger glass beads. (d) In-phase resistivity spectrum for sample using smaller glass beads. (e) Quadrature resistivity spectrum for sample using smaller glass beads. (f) Relaxation time distribution for sample using smaller glass beads. Arrow indicates the location of the “hand picked” characteristic frequency.

Figure 4.11. Data and Debye decomposition result for samples incorporating clay 3. (a) In-phase resistivity spectrum for sample using larger glass beads. (b) Quadrature resistivity spectrum for sample using larger glass beads. (c) Relaxation time distribution for sample using larger glass beads. (d) In-phase resistivity spectrum for sample using smaller glass beads. (e) Quadrature resistivity spectrum for sample using smaller glass beads. (f) Relaxation time distribution for sample using smaller glass beads. Arrow indicates the location of the “hand picked” characteristic frequency.

Figure 4.12. Data and debye decomposition result for samples incorporating clay 4. (a) In-phase resistivity spectrum for sample using larger glass beads. (b) Quadrature resistivity spectrum for sample using larger glass beads. (c) Relaxation time distribution for sample using larger glass beads. (d) In-phase resistivity spectrum for sample using smaller glass beads. (e) Quadrature resistivity spectrum for sample using smaller glass beads. (f) Relaxation time distribution for

sample using smaller glass beads. Arrow indicates the location of the “hand picked” characteristic frequency.

Figure 4.13. Comparison of relaxation times estimated using different inversions of the complex resistivity versus mean glass bead diameter by (a) hand picking and (b) Debye decomposition of the in-phase and quadrature resistivity spectrum.

Figure 4.14. Ratio of relaxation times for samples with the same clay type but different glass bead sizes for (a) hand picked values and (b) fitting both real and imaginary spectra.

Figure 4.15. Relaxation time vs the clay specific surface area for relaxation times calculated by (a) hand picking and (b) Debye decomposition of the in-phase and quadrature resistivity spectrum. Filled and open symbols represent the samples composed of the larger and smaller beads, respectively.

Figure 4.16. Idealized pore system (top) and concentration distribution when electric current flows (bottom). C0 – equilibrium concentration, C* additional concentration under electric field. J is the current density vector. Region A denotes large open pores while region B denotes narrow, ion-selective pores.

List of Symbols

P_c – Confining pressure (Pa)

P_p – Pore pressure (Pa)

P_e – Effective pressure (Pa)

P_d - Differential Pressure (Pa)

P_i- Atmospheric pressure (Pa)

b - effective stress cooefficient

V_p – P wave velocity (m/s)

V_s – S wave velocity (m/s)

K – Bulk Modulus (GPa)

μ – Shear modulus (GPa)

Q_{ijkl}- Stiffness tensor for elastic solid

B_N – Normal crack compliance (1/GPa)

B_T – Tangential crack compliance(1/GPa)

M_e- Closure modulus (GPa)

B_e- Unnamed crack parameter (1/GPa)

n- Power law exponent

A_c- Contact area

p – unnamed crack parameter

K_0- uncracked bulk modulus (GPa)

μ_0- uncracked shear modulus (GPa)

φ – Fractional porosity

φ_c- Fractional crack porosity

σ – Electrical conductivity (s/m)

σ^* – Complex electrical conductivity (s/m)

σ' – real part of σ^*(s/m)

σ'' – Imaginary part of σ^*(s/m)

σ_{fr} – Electrical conductivity attributed to cracks and fractures(s/m)

σ_r – Bulk rock electrical conductivity (s/m)

σ_w – Electrolyte electrical conductivity (s/m)

σ_T – Total conductivity (s/m)

σ_s – Surface conductivity (s/m)

ρ – Electrical resistivity (ohm-m)

ρ^* – Complex electrical resistivity (ohm-m)

ρ' – real part of ρ^* (ohm-m)

ρ'' – Imaginary part of ρ^* (ohm-m)

ρ_0- DC resistivity (ohm-m)

n_c- Number of cracks

F – Formation factor

m – Cementation exponent

$\Delta\gamma$- Local electrical potential gradient (V/m)

E- Electrcic Field (V/m)

J – Current density (A/m)

I – Current (A)

R – Resistance (ohm)

R^*- Complex resistance (ohm)

R_w – Electrolyte resistance (ohm)

A – Surface area (m^2)

L – Sample length (m)

d – diameter (m)

e_b- Normalized electric field

Δt – Time of flight (s)

V – Voltage (V)

ω – Angular frequency (rad/s)

f – Frequency (hz)

Z – Impedance (ohm)

Z^* - Complex impedance |(ohm)

G- geometric factor

τ_c – Characteristic relaxation time (s)

M – Chargeability

V_{samp} – volume of a sample (m^3)

M_t- Total mass (Kg)

M_s – Sediment mass (Kg)

ρ_f – Density of electrolyte (Kg/m^3)

ρ_g- Grain density (Kg/m^3)

ρ_b – Bulk density (Kg/m^3)

ρ_a – Air density (Kg/m^3)

t – Transference number

D – Diffusivity (m^2/s)

β – Ionic mobility ($m^2/V\text{-}s$)

μ_+- Bulk concentration of cations ($mols/m^3$)

Δn – Difference in ion transport numbers for different types of pores

τ – Tortuosity

T_{ij}- Connectivity tensor

L_e- effective length (m)

q – current source (A)

i,j - indices

Chapter 1

Introduction

1.1) Background

The electrical properties of rocks and soils, particularly those free of electronically conductive minerals, are largely controlled by their saturating liquids. Conversely, this means that fluid contents of materials in the earth can be inferred from measurements of their electrical properties. This is quite useful in an exploration context where the existence of fluids, be they hydrocarbons, fresh or saline waters, or geologically sequestered CO_2, are often the target. The electrical resistivity, too, reveals information about porosity and the complexity of pore structures; information that can be usefully combined with other geological and geophysical observations and which is key to understanding subsurface fluid motions. Specifically, these petrophysical properties include pore volume, pore "connectivity", pore shape and pore space anisotropy.

The work in this thesis takes an experimental laboratory approach to examine some of the pertinent issues that relate rock structure to electrical conductivity be it through fracture induced anisotropy, correlation of pressure dependence of conductivity and mechanical wave speeds, or the influence of clays.

The relationships between the electrical and the petrophysical properties are almost exclusively discussed in the contexts of either Archie's (1942) empirical law or of Differential Effective Medium theory (DEM) (Bruggemann 1935; Hanai, 1968; Sen et al, 1981; Bussiann 1983). Both approaches have had wide empirical success in describing certain aspects of the electrical properties of rocks and soils. For instance, Archie's law successfully describes the apparent power

law relationship between porosity and electrical conductivity. Although this relation does not strictly hold for every rock (See Liu and Katinadis 2013 for a discussion on how this breaks down in anisotropic environments), it is a property that is common enough in sedimentary rocks that, at least in an isotropic environment, it is thought that any theoretical models describing electrical conductivities of porous mediums should reproduce this behavior. This is achieved by DEM (See Chelidze and Gueguen, 1999 for an example of how it is derived). Sen et al., (1981) and Bussian (1983) derived expressions that were similar to Archie's law and were identical in the limit of a nonconductive matrix which is usually a good assumption in sedimentary rocks assuming that there are no conductive minerals. This was further extended by Mendelson and Cohen (1982) for the case of a medium with anisotropic conductivity, a complicating characteristic that is scarcely covered in detail in the literature.

It is now known that rocks commonly assumed to be isotropic are in fact anisotropic (North and Best, 2014). Yet, little work has been done to isolate the extent to which various mechanisms of anisotropy may contribute to it. Fracture induced anisotropy is an important mechanism to consider since fractures can control the direction of fluid flow in the subsurface. However, to extract useful information from electrical data, one must understand how different anisotropy mechanisms such as compaction/grain alinement and fracture induced anisotropy may interact with each other. This is difficult to measure since it difficult to isolate the two effects in real rock samples.

Additionally, there is a pressure dependence in the electrical resistivity that is introduced by cracks and fractures. This pressure dependence is also seen in the elastic properties when measured in terms of wave velocities. Modeling the effects of micro-cracks and fractures on the elastic stiffness tensor is common (e.g. Kachanov, 1992) but the pressure dependence is seldom modeled. Both elastic and electric pressure dependences have been modeled using Hertzian contact theory,

however, these models have never been tested against each other. Indeed, if the pressure dependence stems from the fracture properties then they should be explained by similar models for crack compliance. It should be noted that the terms crack and fracture may both be used to describe nominally flat defects in general but appropriate distinctions are made on the terminology in Chapters two and three.

All the topics just mentioned deal with how the electric conductivities of the different solid and fluid constituents making the porous rock affect its bulk conductivity. In the case of a non-conductive matrix, this allows an investigator to characterize the rock in terms of the fluid content (conductive vs non- conductive fluids) and pore space interconnectedness and volume. The fluid phase and the rock phase are therefore binary components of this mixture. However, there are regions in the rock where the rock and fluid can be viewed as a mixed phase. These regions are the electrical double layers that form at the interface of mineral grains and pore fluid.

Some mineral grains can be viewed as electrically active in that their surfaces retain charge. This is true for silica grains (Leroy et al., 2008) and clay minerals (Brady et. al.,1996) for reasons discussed later. The existence of an electrical double layer on charged surfaces immersed in electrolytes has long been known about and was previously modeled by the Poisson Boltzmann Equation (PBE) (Honig and Nicholls, 1995) which produces a surface potential that is generally recognized as the "diffuse layer" or Zeta potential in electrochemistry. Advancements in computing have prompted the rise to prominence of molecular dynamics simulation and the use of nonequilibrium molecular dynamics (NEMD). A relevant theoretical difference between these two methods is that the PBE uses a continuum-based approach whereas NEMD is an atomic based approach. The difference in the results of these two approaches is the existence of the Stern Layer which is too thin to be detected in the continuum-based approach.

For years since the work of Marshall and Madden (1959) the electrical diffuse layer was thought to be responsible for the observed weak polarization of sandy/clayey sediment at low frequencies. While some of the polarization at low frequencies (100Hz to 100K Hz) has been explained by Maxwell-Wagner polarization that may be described by DEM, polarization persisting down to low frequencies of 1 mHz is commonly observed and occur at length scales that are longer than those used to explain Maxwell-Wagner polarization (Chelidze and Gueguen, 1999). This has typically been explained as "membrane polarization"(Marshall and Madden,1959; Waxman and Smits,1968; Vinegar and Waxman 1980; Klien and Sill, 1982; Titov et al., 2002). The idea being that the diffuse layer acts as a cation selective membrane so that cations, under an applied electric field, accumulate at one end of the pore throat resulting in a concentration gradient of cations that creates a membrane potential. In recent years since Revil and Glover (1998) discussed the relevance of the Stern layer to surface conduction (i.e. the migration of charges adsorbed to grain boundaries in the direction of an applied electric field) the idea of Stern layer polarization has gained increasing popularity along with similar grain-based models (Schwarz, 1962; de Lima and Sharma, 1992; Leroy et al.,2008; Revil, 2012; Jougnout et al., 2010 Revil et al., 2013). In these models the grains themselves are polarized as ions migrate along grain boundaries but do not move perpendicular to the grain. Under an applied electric field this results in a surplus of cations on one side and a deficiency on the other that produces a potential difference between either side of the grain. As to which of these is true (assuming one of them is true or both of them are true), it is difficult to assess given that these processes are not observed but investigated indirectly. Both have been successfully used to describe data but given the similar controls on the models this is not surprising. Both are controlled by the parameter of "grain size" (Titov et al., 2002; Revil and Florsch ,2010) which is typically thought of as grain diameter. However, this parameter in turn

exercises control over the average length of pore throats and so they are indistinguishable from each other from an indirect measurement without examining the individual constituents of the material.

Compounding this problem is that the only measurable parameter that can reliably be used to predict the frequency at which polarization is maximum (thought to correspond to the dominant length scale in the rock) is pore throat diameter which can be measured via mercury injection (Scott and Barker 2003; Scott,2006). This parameter will obviously exercise control over both grain size and pore throat length but more importantly can be used to predict permeability. This has therefore been one of the main drivers for development of induced polarization methods. The ability to identify dominant relaxation times would effectively allow for field scale permeability tomography for sandy/ clayey aquifers (Vanhalla 1997; Revil, 2012; Revil and Florsch, 2014; Revil et al., 2015; Karaoulis et al., 2011). That said, it is still unclear exactly why the dominant relaxation time corresponds so closely to the pore throat diameter although many have speculated and used models of the type described above to explain data.

The work here is motivated by the need for improved rock physics models to aid in processing and interpreting geophysical data. Specifically, we seek to quantitatively investigate how crack and fractures affect the electrical properties of a rock, and identify the dominant length scale associated with induced polarization.

1.2) Contributions

As noted, the thesis examines through laboratory measurements aspects of electrical conductivity anisotropy, pressure dependence, and clays. This is accomplished in the three following chapters.

Because each chapter focusses on its own aspect of electrical conductivity, they are relatively self-contained with the expectation of future publication.

In the next Chapter 2, we examine the effect of crack-like porosity on the pressure dependence of electrical and elastic properties. We attempt to integrate formulations proposed by different authors for pressure dependent electrical conductivity and elastic wave velocity into a unified model. This is done assuming an isotropic distribution of crack orientations. Pressure sensitivity of cracks is modeled using Hertzian contact theory (Greenwood and Williamson, 1966) and the corresponding change to electric properties due to crack deformation under pressure is subsequently predicted. This is compared to a new experimental dataset where ultrasonic P and S wave velocities are measured almost simultaneously with electrical conductivity under a range of confining and pore pressures. P and S waves were recorded when the rock was unsaturated provide five different individual datasets to constrain the model parameters. This is important since integrating information from multiple datasets is among the best approaches to reducing uncertainty in an exploration context. It is therefore important to understand exactly what relates the two properties and corresponding changes in either.

Chapter 3 is a preliminary experimental study of the influence of fractures on electrical anisotropy. Here we provide electrical measurements on synthetic porous material specially constructed to contain well geometrically defined fractures. The corresponding anisotropy in typical electrical rock physics parameters is reported, and how they vary with crack and background porosity. This is important for understanding how much fractures are expected to affect the anisotropy in electrical conductivity and fluid flow in reservoirs.

Finally, in Chapter 4 we conduct an experiment using clay and glass beads to shed light on what is the dominant mechanism behind the spectral induced polarization (SIP) response in sandy

sediments. The experiment is designed in such a way that a relaxation time corresponding to the size of the glass beads suggest membrane polarization to be the controlling mechanism and a relaxation time corresponding to the clay size (specific surface area) would suggest Stern layer polarization.

The main contributions can be summarized as:

1) Furthering the understanding of how electrical and elastic properties are related in rocks using a novel experimental data set. To this end we use a theoretical description of the effects of cracks and fractures on a porous matrix to jointly model the pressure-dependence of both elastic and electrical properties.

2) An experimental investigation of fracture induced electrical anisotropy. We quantitatively investigate how ratio of crack porosity to total porosity affects the observed anisotropy in an environment with aligned cracks or fractures.

3) Strong experimental evidence that membrane polarization and not Stern layer polarization is responsible for the observed low frequency electrical relaxation time in sandy/clayey sediments.

1.3) Thesis outline

The thesis is structured so that the first two contributions deal with the effects fractures and cracks have on pore space electrical conduction. In Chapter 2 we look at the effect of pressure on electrical conductivity and elastic parameters. It includes a description of the experimental method in addition to theoretical work. We integrate the model of Stesky (1986) with a description for pressure dependent elastic properties of cracks given by Gao and Gibson (2012). The hypothesis here is that if the changes in both ultrasonic velocity and conductivity are due to the same thing

(opening and closing of cracks), then it should be possible to describe them using a common theoretical framework. The benefit of this is that it provides a logically consistent model that can be used to model both elastic and electrical properties, specifically their pressure dependence. While the model is complicated this represents an attempt to mechanistically link the two properties instead of relying on combinations of empirical relations that relate the elastic and electrical properties to porosity.

In Chapter 3, experimental results are presented for electrical conductivity anisotropy in a porous material with an oriented fracture. Much of the chapter is dedicated to describing how the samples were prepared and how measurements were made in multiple directions for each sample. A simplified sample and measurement geometry allow us to treat the problem as if it were a 2D conductivity problem. The benefit of using these synthetic samples is that they allow us to remove the confounding effect of surface conductivity and to focus solely on the effects of the pore space so that we can gain a better understanding of how background porosity interacts with crack porosity to control electrical conductivity anisotropy.

Chapter 4 examines the topic of Spectral Induced Polarization in sandy/ clayey material where we attempt to answer the question as to what mechanism is controlling the dominant low frequency electrical relaxation time in rocks. This is a topic that has become contentious in recent years with many recent works favoring Stern Layer polarization as the mechanism. The beginning of the chapter is used to describe the experimental method as well as give a detailed explanation for the existing theoretical models. We give experimental evidence that it is, apparently, membrane polarization that is dominating the response if not being solely responsible for it. This chapter also includes an exercise in using Debye decomposition to fit the entire spectrum and we attempt to

identify a best practice for how to use this method to automatically pick relaxation times as opposed to picking them “by hand” which is common (Revil et al., 2015).

In chapter 5 we summarize what we believe to be the main takeaways from this work and outline future directions for research.

Chapter 2

Constraint of crack properties in rocks by joint inversion of ultrasonic and electrical laboratory measurements.

2.1) Introduction

Nearly a century ago, Adams and Williamson (1923) observed that the linear compressibilities of a variety of different rock types depended nonlinearly on confining pressure. This behaviour was later confirmed in ultrasonic wave speeds (e.g., Wyllie et al, 1956), permeability (e.g. Fatt and Davis, 1952), and electrical resistivity (e.g. Brace et al, 1965). The properties vary nonlinearly with pressure due to the progressive closure of the compliant, crack-like pore space. A large literature has developed over the last 50 years that examines this problem from experimental, theoretical, and numerical modelling perspectives.

Further, numerous field studies have noted linkages between electrical conductivity and seismic wave speed in the deep crust (e.g., Marquis and Hyndman, 1992; Moorkamp et al, 2010), in upper crystalline cratonic crust (e.g., Yan et al, 2017), and in sedimentary basins (e.g., Brown et al, 2012). The use of time-lapse geophysical surveys in recent decades to remotely monitor subsurface fluid motions and pressures (e.g., MacBeth et al, 2006), too, has intensified the need to better understand how electrical and seismic properties might be jointly used to provide for more informed interpretations.

Theoretical and empirical models describing rock physical properties usually focus on a single characteristic without consideration of changing pressure. Numerous theoretical models attempting to describe elastic (e.g., Cheng and Toksoz, 1979; Kachanov, 1992; Sarger and Shapiro,

2002; Hashin, 1988) or the electrical properties of rocks (e.g., Archie, 1942; Sen et. al, 1981; Bussian, 1983; Bernabe, 1991; Durr et al., 2002; Han, 2018a) have largely been independently developed. However, electrical and elastic properties are seldom integrated or tested against each other. This is unfortunate because, although the basic physical mechanisms controlling these properties may differ, the basis for their pressure dependency relies on the same closing of compliant pores and on the fluids they contain. Consequently, the electrical and elastic properties can complement one another in attempts to better understand the in situ physical conditions and structure.

That said, there are a number of notable exceptions where the linkages between the pressure dependencies of both properties are examined. Various authors (e.g., Carcione et al, 2007) have employed simple effective medium models to link seismic wave speeds to electrical conductivity through porosity and saturation state, although the validity of such approaches has been questioned (Han et al, 2016). Aquino-Lopez et al. (2011) employed an effective medium approximation approach that assumed both the pores and grains were triaxial ellipsoids. Han et al. (2011) developed a three-component model by combining a self-consistent approximation with a Differential Effective Medium model to predict the electrical and elastic properties of an extensive series of laboratory measurements on reservoir sandstones. Bacharach (2011) similarly used an effective medium paradigm to calculate the joint properties of shales. Kazatchenko et al (2006) inverted acoustic and electrical logs in a carbonate aquifer to infer the dual porosity structure. Most recently, Han (2018b) successfully modelled weak P-, SH-, and SV-wave and electrical anisotropies observed in artificial samples with controlled crack geometries using elastic (Chapman, 2003) and dielectric (Asami, 2002) models, with the two properties linked via an angle taken with respect to the textural symmetry. A number of authors, too, have developed empirical

cross-relations from laboratory experiments (e.g. Jensen et al, 2013; Gomez et al, 2010; Wang and Gelius, 2010). However, none of this work takes into account the joint changes to resistivity and elastic wave velocities induced by varying the effective pressure on the material, nor takes further advantage of it with a goal of better understanding the compliant pore structure.

There have been many studies that have looked at pressure dependent elastic moduli from numerous perspectives (see recent review in Schmitt, 2015). A number of these have inverted observed velocities or elastic moduli to obtain information regarding the pore structure, and all of these of course depend on the model used to describe the pressure dependence. A great deal of attention has been paid to models in which the compressible pores are simplified to oblate spheroids. Cheng and Toksöz (1979) obtained distributions of the frequency of range of pore aspect ratios based on an ellipsoidal inclusion model, various inversion schemes have been based on their concepts (e.g., Burns et al, 1990; Izutani and Onozuka, 2013; Zhang et al., 2019)). David and Zimmerman (2012) developed a scheme to invert wave speeds for pore structure using a dual porosity model of compliant cracks and stiff equant pores. Glubokovskikh et al, (2016) develop expressions based on a donut shape consisting of an oblate spheroid with a welded center to simulate a single asperity and found this model was able to describe the pressure varying wave speeds. Other workers attempted statistical descriptions that attempted to consider complicated and realistic crack geometries; almost all of these account for pressure dependence using Hertzian contact theories (Greenwood and Williamson, 1966). The major difference between these studies depends on the manner in which the statistics of the contacting asperities were quantified with polynomial (Mavko and Nur, 1978), exponential (Walsh and Grosenbaugh, 1979; Carlson and Gangi, 1985), Gaussian (Brown and Scholz, 1985; Stesky and Hannan, 1989), fractal (Wong et al, 1989), and power law (Gao and Gibson, 2012) distributions all having been used. Zaitsev et al

(2017) invert directly for pressure dependent crack stiffnesses avoiding entirely having to assume specific crack geometry.

There are fewer studies that relate to the pressure dependence of electrical conductivity. Brace and Orange (1968) looked at the effect of pressure on resistivity for a large number crystalline and sedimentary rocks. Although he did not look at electrical conductivity directly, Gangi (1978) developed a bed-of-nails asperity model for the analogous transport property of permeability. Stesky (1986) extended similar measurements to crystalline rocks some of which contained more macroscopic fractures. Glover and Vine (1995) carried out difficult high-pressure, high-temperature measurements on a series of metamorphic rocks obtained from scientific drilling programs. In these studies, the nonlinear pressure dependence of the electrical properties was found to be similar to that seen for elastic properties. Recently, Han (2018a) modelled the pressure dependency of electrical conductivity using an effective medium approach that incorporated a dual porosity model with stiff and compliant pore; this model was used to provide information about the pore structure from laboratory electrical measurements.

Doyen (1987) is one rare example in which the pore structure was deduced from joint inversion of wave speeds, electrical conductivity, and permeability in a granite under the assumption of long tube-like pores with elliptical cross-section. Pride et al, (2017) suggest analytical models that describe how wave speeds, electrical conductivity, and permeability vary with pressure with particular focus on low porosity crystalline rocks.

In this work we describe a series of simultaneous ultrasonic velocity and electrical resistivity measurements on two samples subject to a range of pore and confining pressures. The samples are selected on the basis of differences in their pore structures with one a clean natural sandstone and the other a highly porous sintered alumina. The aim was to see how the wave speeds and

electrical conductivity of the two petrophysically distinct samples responded to changes in pore and confining pressure. The electrical and elastic wave responses of the sandstone samples are then jointly used in an inversion procedure to produce information by combining Gao and Gibson's (2012) elastic and Stesky's (1986) electrical models of pressure dependency.

2.2) Background

In porous sediments free of clay and conductive minerals, electrical measurements are primarily sensitive to the electrolytic liquid conductivity, the saturation state, the porosity, and the pore space topology all of which is reflected in Archie's (1942) empirical relation. The bulk elastic moduli of these same sediments are also controlled by porosity, saturation state, and pore space topology, but fluid and solid moduli and density must be considered if seismic velocities are used as proxy measures of the material's elasticity. Consequently, the electrical and mechanical sediment properties complement one another in characterizing a rock. The successful integration of these two measures, however, is limited due to the lack of precisely controlled experiments that seek to unwrap individual dependences on mineralogy, pore topology and fluid type. Overcoming this requires careful experimental design where most factors can be held constant while a single parameter is varied. In the following subsection we describe the concept of effective pressure, the dependence of wave velocities and resistivity with pressure and conclude with a brief note on Differential Effective Medium theory and why it is not used here.

2.2.1) Effective pressure

As already noted, many of the physical properties are nonlinearly dependent on the confining pressure P_c or stress that the material is subject to. More properly the influence of the pore fluid pressure P_p must also be included as, typically, it acts against P_c through effective pressure rules.

Specifically, a rock in the earth is subject to tectonic and overburden stresses, that for the sake of simplicity is considered here as a uniform confining pressure P_c. At the same time and assuming that the system is in equilibrium (i.e., drained conditions) the pores of the rock will be filled with fluid that has the independent pressure P_P. Generally, a given physical property (e.g., wave speeds, electrical conductivity) does not vary if the differential pressure $P_d = P_c - P_p$ remains the same. This means that, to a first approximation, the value of the physical property at any combination of P_c and P_p can be predicted if it has already been measured in the saturated sample over a range of P_c while P_p =0. The differential pressure is often also called the effective pressure P_e and

$$P_e = P_d = P_c - P_p \tag{2.1}$$

The effective pressure is defined such that a given physical property should have the same value, at the same effective pressure, for any combination of pore and confining pressure. While Eqn. 2.1 generally holds for material failure, seismic wave speeds, permeability, and electrical conductivity there are conditions where the P_p term must be modified. When pore pressure does not exactly cancel out the effects of confining pressure then the effective stress coefficient b is introduced so that

$$P_e = P_c - bP_p \tag{2.2}.$$

A value of $b \neq 1$ might be required in cases where chemical effects, such as swelling clays, may affect the pores space. In poroelasticity, the effective stress for volumetric strain, too, must include a value of b that is less than 1 except for highly compressible sediments. In the analyses below, we assume that the simple, or Terzhaghi, effective pressure law of Eqn. 2.1 applies (e.g., Gangi and Carlson, 1996).

2.2.2) Pressure dependence of wave velocities

Compressional (V_p) and Shear (V_s) wave velocities for isotropic materials as a function of differential pressure are described as

$$V_p(P_d) = \sqrt{\frac{K(P_d) + \frac{4}{3}\mu(P_d)}{\rho_b}} \tag{2.3}$$

$$V_s(P_d) = \sqrt{\frac{\mu(P_d)}{\rho_b}} \tag{2.4}$$

where $K(P_d)$ is the pressure dependent bulk modulus, $\mu(P_d)$ is the pressure dependent shear modulus and ρ_b is the bulk density which can be assumed to be constant for the pressures encountered here. The non-linear pressure dependence of $K(P_d)$ and $\mu(P_d)$ are generally attributed to crack closure at low differential pressures.

Effective medium theory has proven to be a useful tool for modeling the effects of fractures on elastic wave velocities. Particularly the approximation of small crack density (or approximation of non-interacting cracks) has been commonly used to analyse anisotropy introduced by cracks (Kachanov, 1992; Sayers and Kachanov, 1995). This theory expresses the elastic compliance tensor of the rock as

$$Q_{ijkl} = Q^0_{ijkl} + \Delta Q_{ijkl} \tag{2.5}$$

where Q^0_{ijkl} is the compliance tensor for the rock in the "uncracked" state and ΔQ_{ijkl} represents the perturbation in these compliances that is introduced by cracks. This term is generally derived by considering the normal B_N and tangential B_T compliances of a single crack and summing the effects of many of these cracks for a given distribution of orientations. B_N and B_T are typically

determined using elliptical integrals (Kachanov,1992), but this does not give any explicit dependence on pressure.

Instead, Gao and Gibson (2012) derived analytic expressions for the crack compliances based on Gangi and Carlson's (1996) "bed of nails" asperity deformation model. They used Hertzian contact theory to provide an explicit pressure dependence to their crack compliance. Their model treats the cracks as nominally flat defects including asperities modelled as elastic half-spheres following the composite topography concepts (Fig. 2.1) developed by Greenwood and Williamson (1966) and later applied to rocks by Brown and Scholz (1985).

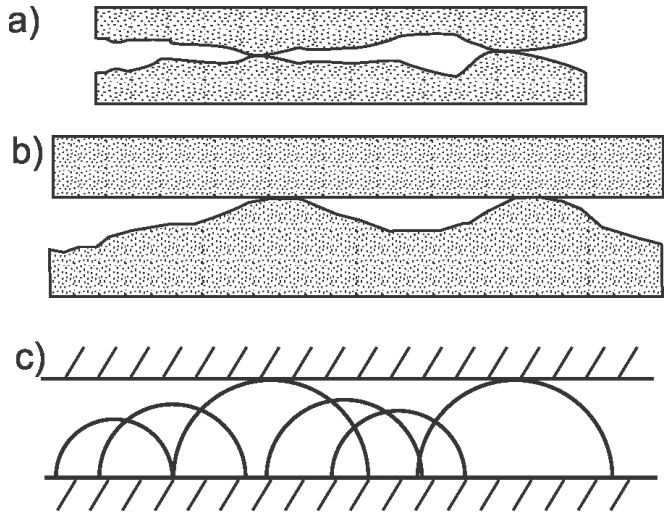

Figure 2.1. a) Hypothetical crack-like porosity within the rock mass showing two points of contact. b) Composite topographic representation of the cracks (after Brown and Scholz, 1985), c) Reduction of the composite topography to representative half-spheres. As the crack closes at higher pressure more asperity spheres will be in contact with the overlying elastic half-space.

Guo and Gibson (2012) consider the statistics of their spherical asperities and derive relationships for the drained crack moduli as a function of P_c:

$$B_N(P_c) = \left[\left(n + \frac{3}{2}\right) M_e \left(\frac{P_c + P_i}{M_e}\right)^{\frac{n+\frac{1}{2}}{n+\frac{3}{2}}}\right]^{-1} \quad (2.6a),$$

and

$$B_T(P_c) = \left[\frac{1}{B_e}\left(\frac{P_c + P_i}{M_e}\right)^{\frac{n+\frac{1}{2}}{n+\frac{3}{2}}}\right]^{-1} \quad (2.6b),$$

where P_i is the atmospheric pressure, M_e is defined as the closure modulus (i.e., the normal compliance of the crack that is equal to the stress normal to the crack when it completely closes) and n is the exponent in a power law describing the statistical distribution of asperity heights on the crack surfaces. Gao and Gibson (2012) introduce B_e as a shorthand for simplicity, but do not give it a name. As can be seen in their Eqn. 46, it is inversely proportional to the shear modulus of the material making up the contacting hemispheres (Fig. 2.1) with the remaining terms arising from the statistics of the asperity heights and locations. Once pore fluid is introduced a pore fluid pressure P_p exists and the corresponding compliances (undrained compliances) becomes

$$B_{N,sat}(P_c, P_p) = \left[\left(1 - P_p \frac{dA_c}{dP}\right) M_n + (1 - A_c) M_f\right]^{-1} \quad (2.7a),$$

and

$$B_{T,sat}(P_c, P_f) = \left[\frac{1}{B_e}\left(P_c - P_p + P_i\right)^{\frac{n+\frac{1}{2}}{n+\frac{3}{2}}}\right]^{-1} \quad (2.7b).$$

where $M_n = {B_N}^{-1}$ and M_f is the bulk modulus of the fluid. A_c is the relative contact area of asperities between the walls of the cracks and is given as

$$A_c = \left(\frac{P + P_i}{M_e}\right)^{\frac{n+1}{n+\frac{3}{2}}} \left[\left(1 + \frac{n}{2}\right) - \frac{n}{2}\left(\frac{P + P_i}{M_e}\right)^{\frac{1}{n+\frac{3}{2}}}\right] \quad (2.8).$$

The values used in Eqns. 2.6 to 2.8 are taken to be the average value of these parameters over all the cracks or linear defects in the rock.

The pressure dependent elastic moduli can therefore be expressed as

$$K(P_d) = \left(d1 + \frac{1}{K_0}\right)^{-1} \quad (2.9a)$$

and

$$\mu(P_d) = \left(d2 + \frac{1}{\mu_0}\right)^{-1} \quad (2.9b)$$

where

$$d1 = B_N \varphi_c \quad (2.10a)$$

and

$$d2 = \frac{2}{15}(2B_N + 3B_T)\varphi_c \quad (2.10b)$$

where φ_c denotes the crack porosity. Eqns. 2.9a and 2.9b can then be substituted into Eqns. 2.3 and 2.4 to yield pressure dependent velocities with knowledge of M_e, B_e, and n.

2.2.3) Pressure dependent electrical conductivities

Stesky (1986) attempted to use similar ideas to model the pressure dependence of crystalline rocks with fractures. He considered a rock shown in Fig. 2.2 with cross-sectional area A and length L.

The rock has a single fracture going through it with aperture *a* and width *w*. He considers conduction in the direction parallel to the crack.

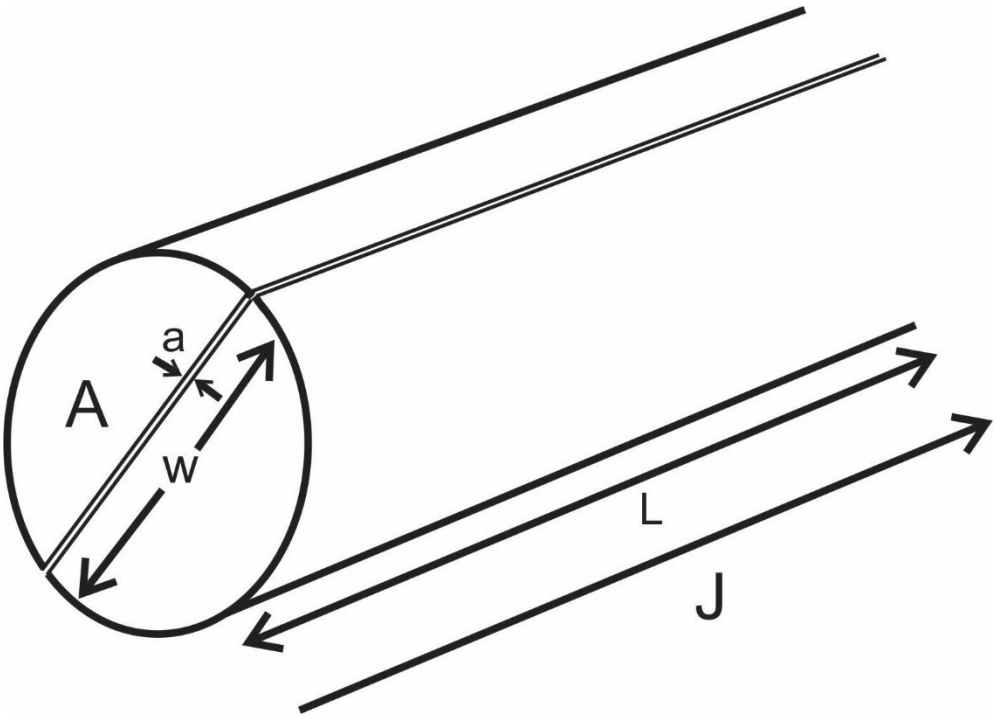

Figure 2.2. Schematic of fracture geometry to describe conduction through a cross section of fractured rock. (Following Stesky (1986)). A is the cross-sectional area of the cylinder normal to its axis. L is the axial length. a and w are the aperture and width of the fracture respectively. J is the current density vector.

Conduction through the rock is modeled as a parallel circuit with conduction through the fracture acting in parallel to conduction through the pore space as indicated in Eqn. 2.11

$$\sigma_T = \sigma_{fr} + \sigma_r \tag{2.11}$$

Where σ denotes conductivity and subscripts *T, fr* and *r* indicate conductivities of the whole rock, crack or fracture like pores and porous matrix respectively.

In the following we only consider σ_{fr} since the matrix porosity is assumed to essentially be pressure independent. This means that all pressure dependence is attributed to fractures which will be true for rocks free of clay and conductive minerals. A small note on terminology is probably necessary here. Cracks and fractures can both be thought of as nominally flat defects in rocks. However, the term crack is generally used when referring to small crack like pores, whereas the term fracture generally refers to a larger scale feature. The difference can be understood here in terms of the material that makes up the "wall" of the defect. In the case of a fracture there is matrix porosity in the wall rock. In the case of a microcrack, the wall rock is the mineral that makes up the grain, which can be assumed to have negligible porosity. σ_{fr} refers to the conductivity attributable to pressure dependent porosity, which in the case of the samples examined here are micro cracks. The following model was developed for fractured crystalline rocks. The low porosity of those rocks (.04% -.4 %) means the fracture walls in those rocks can be treated similarly to the mineral surfaces although the scale of the asperities modeled will be different.

According to Stesky (1986), the electrical conductivity σ_{fr} through a fracture of aperture a and width w (Fig. 2.2) is given by:

$$\sigma_{fr} = \sigma_w \frac{a\, w}{A} \tag{2.12}$$

where σ_w is the conductivity of the saturating electrolyte. The aperture is a function of differential pressure (i.e., $a = a(P_d)$) with a_0 taken as the aperture at zero pressure. Eqn. 2.12 can be generalized to the case of multiple fractures by multiplying the number of fractures n_c by the average crack aperture and width averaged using the geometric mean for all fractures involved in conduction. This leads to

$$\sigma_{fr} = \frac{\sigma_w n_c}{A} \bar{a}(P_d)\, \bar{w} \tag{2.13}$$

were bars over a quantity indicate that they are a geometric mean of those quantities.

In order to model the pressure dependence of the crack aperture, Stesky (1986) uses semi-empirical relations (see his Eqns. 2.9 and 2.10). Here, the pressure dependence is instead incorporated by consideration of the normal fracture compliance (Eqn. 2.6a).

To begin, we define the number of cracks (n_c) as

$$n_c = \frac{\varphi_c A}{a_0\, w} \tag{2.14}$$

where a_0 is the crack aperture at the atmospheric pressure. The pressure dependent crack aperture is simply expressed as:

$$a(P_d) = a_0\, f(P_d) \tag{2.15}$$

where $0 \leq f(P_d) \leq 1$ is a pressure dependent function to be developed. This is accomplished by considering the definition for the normal crack compliance:

$$\frac{1}{B_n(P_d)} = -a\, \frac{dP_d}{da} \tag{2.16}$$

Rearranging and integrating gives

$$-\int_{a_0}^{a(P_d)} \frac{da}{a} = \int_{P_0}^{P} B_n(P)\, dP_d \tag{2.17}.$$

then defining the right-hand side as Cp and integrating gives:

$$a(P_d) = a_0\, \frac{1}{e^{Cp}} \tag{2.18}$$

so that

$$f(P_d) = e^{-Cp} \tag{2.19}$$

Now, using Eqn. 2.6a Cp can be shown to be

$$Cp = Me^{-\frac{1}{n+\frac{3}{2}}}\left(P^{\frac{1}{n+\frac{3}{2}}} - P_0^{\frac{1}{n+\frac{3}{2}}}\right) \tag{2.20}$$

Note that using Eqn. 2.6a instead of Eqn. 2.7a means that the fractures are drained (i.e., any excess pore pressure induced by application of the confining stress is allowed to decay by flow out of the sample). This condition is applicable to our experiments below for predicting the change in aperture at the different measurement pressures. If instead the pore pressure was held constant and the confining pressure was increased, Eqn. 2.17 would have to use Eqn. 2.7a instead of equation 6a to define the normal crack compliance. Substituting Eqns. 2.14 and 2.19 into Eqns. 2.13 gives

$$\sigma_{fr} = \sigma_w \, \varphi_c \, f(P) \tag{2.21}.$$

Stesky (1986) adds an additional term to account for the increasing tortuosity of the flow channels with the changing relative asperity contact area A_c defined in Eqn. 2.6. Walsh (1981) developed a form using analogies between electrical and thermal conductivities. Clennell (1997) commented, however, that molecular diffusion (which is analogous to movement of ions under a potential gradient) can be retarded by the roughness of the pore wall, and this retardation would be especially pronounced in cracks whose two rough opposing faces are almost in contact. This effect is not expected to influence thermal transport and as such Walsh's (1981) analogy may not be adequate. It is difficult to obtain exact expressions that might describe the influence of the crack roughness, and instead this effect was included in an *ad hoc* fashion by incorporating another parameter

incorporated as an exponent $0 \leq p \leq 1$ on the A_c term. Including this effect as an exponent maintains that, as A_c tends to zero the entire term, $\frac{1-{A_c}^p}{1+{A_c}^p}$, tends to 1. In a physical sense, the exponent causes the electrical conductivity to decrease more rapidly at lower differential pressures. This exponent p was determined by including it as an additional parameter to be fit along with. Including this term in Eqn. 2.21 gives:

$$\sigma_{fr} = \sigma_w \, \varphi_c \, f(P) \frac{1 - {A_c}^p}{1 + {A_c}^p} \tag{2.22}.$$

Substituting this expression back into Eqn. 2.11 results in

$$\sigma_T = \sigma_w \, \varphi_c \, f(P) \frac{1 - {A_c}^p}{1 + {A_c}^p} + \sigma_r \tag{2.23}$$

The conductivity of the matrix rock can be modeled using Archie's (1942) equation

$$\sigma_r = \frac{1}{F} = \sigma_w \varphi^m \tag{2.24}$$

where φ is the connected porosity and F is the formation factor. However, for heavily cracked rocks, Revil and Cathles (1999) explain that the formation factor may simply be equal to the crack porosity. As they point out, this is due to the physical meaning of the inverse formation factor. Following Avellaneda and Torquato (1991) the formation factor can be expressed as

$$\frac{1}{F} = \frac{1}{Vol} \int_{V_p} |e_b|^2 \, dV_{pore} \tag{2.25}$$

where Vol is the volume of the rock V_{pore} is the pore volume and $e_b = \frac{\Delta\gamma}{|E|}$ is the normalized electrical field inside the interconnected pore space which is equal to the ratio of the local electrical potential gradient ($\Delta\gamma$) and the electric field magnitude ($|E|$). As is explained in Revil

and Cathles (1999), $|e_b|^2$ acts as a weighting function for the total interconnected porosity $\varphi = \frac{V_{pore}}{Vol}$. This means that the inverse formation factor is a measure of the porosity that excludes dead end pores and pores not involved in transport. They go on to explain that the electrical potential gradients are most concentrated in the pore throats. In rocks with many cracks, all of the cracks may be thought to be involved in transport. This, coupled with the fact that the inverse formation factor (as a measure of the porosity dynamically connected by lines of current flux) weights the crack porosity highest for rocks that consist of mostly crack porosity, means that for heavily fractured rocks, Eqn. 2.23 can be expressed as

$$\sigma_T = \sigma_w \, \varphi_c \, f(P) \frac{1 - {A_c}^p}{1 + {A_c}^p} \approx \sigma_w \frac{1}{F} f(P) \frac{1 - {A_c}^p}{1 + {A_c}^p} \qquad (2.26).$$

We later apply this assumption to our inversions of a heavily microcracked Berea Sandstone and a very intact alumina ceramic. Using Eqns. 2.3,2. 4, and one of 2.23 or 2.26, measured wave velocities (under dry and saturated conditions) and electrical conductivities are inverted to obtain model parameters (defined earlier) Me, n , B_e, φ_c, K_0, μ_0,m, $and\ p$ using a genetic algorithm described later.

2.3) Experimental set up

Both the ultrasonic and electrical measurement methods are described here with the experimental configuration summarized in Fig. 2.3a. A thermocouple housed inside the vessel is connected to a digital read out outside the vessel (Fig. 2.3a) allowing the temperature to be monitored to within 0.1°C. The confining pressure is regulated by a computer-controlled pump (Quizix Q5000 metering pump). The pore pressure is manually controlled by a pressure intensifier outside the pressure vessel. The pore pressure was set based on an analog pressure gauge with 1 MPa resolution. A temperature of 22°-23°C was maintained for each measurement.

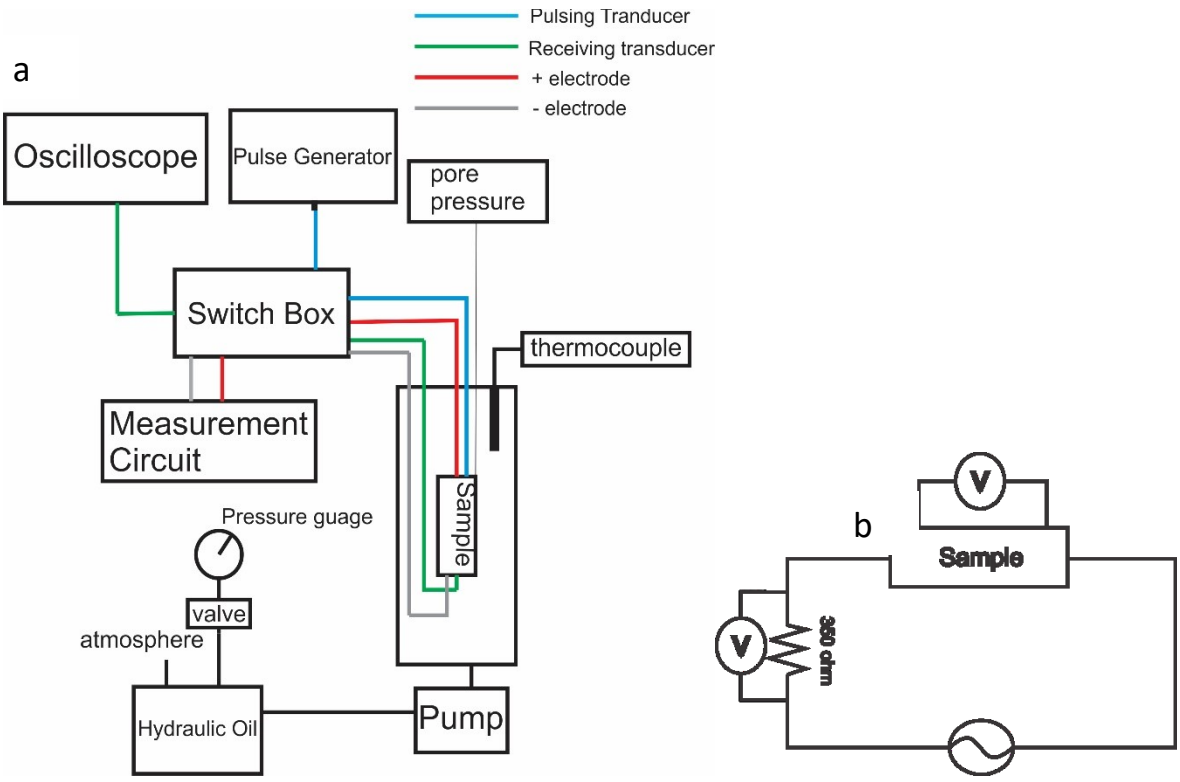

Figure 2.3. a) Experimental set up for electrical resistivity and ultrasonic wave velocity measurements in a pressure vessel. b) Measurement circuit used for electrical resistivity measurement

2.3.1) Ultrasonic measurements

Piezoelectric ceramic transducers (AmericanPiezo - APC shear mode piezo plates, 15.0 X 15.0 mm, 750 kHz - material 850 and APC longitudinal mode 20.00 mm diameter, 1 MHz - material 840) with resonant frequencies of 1 MHz and 0.75 MHz are used to both send and receive, respectively, ultrasonic P- and S- waveforms. Pulses are launched by stimulating the ceramics with a rapid step voltage (~200 V). The propagated mechanical pulses are then converted into voltages by the receiving ceramics and acquired at a 10 ns sampling period for 9999 samples using a digital oscilloscope. A minimum of 300 individual pulses were stacked to improve the signal to

noise ratio in order to create a final waveform for analysis. Since the P and S wave transducers are stacked on top of each other, they are recorded sequentially. The transducers are mounted onto aluminium endcaps. To account for the travel time of pulses through the endcaps, calibration measurements are taken for travel times through the endcaps at measurement pressures. These are later subtracted from the measurements of travel time through the entire sample.

An example of the first break picking to determine the transit time is shown in Fig 2.4. After accounting for the delay due to the endcaps, the time-of-flight Δt is used with the sample length (L) to calculate the wave velocity

$$velocity = \frac{L}{\Delta t} \tag{2.27}$$

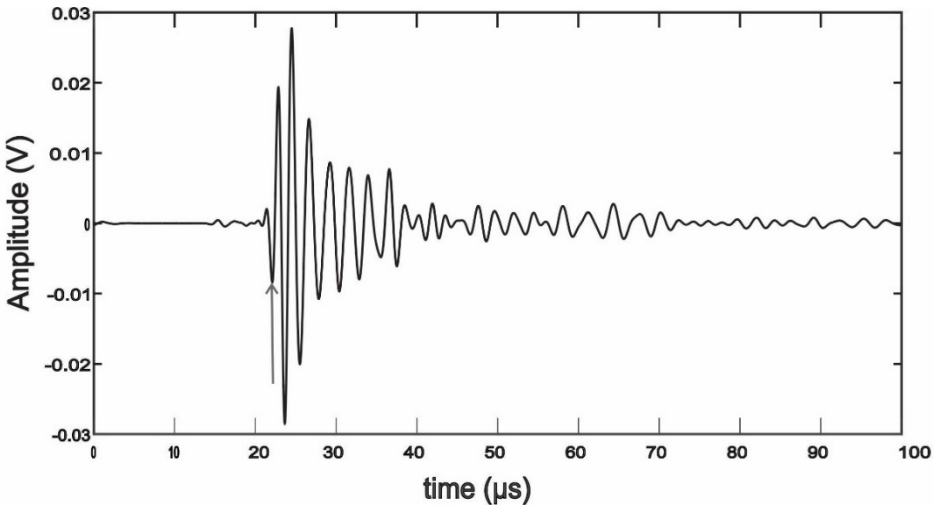

Figure 2.4. Filtered waveform from ultrasonic velocity measurement with an arrow indicating arrival time determination.

2.3.2) Electrical measurements

A simple IV circuit was used for the electrical measurements (Fig. 2.3b). A volt meter with floating leads (HP 34401a) measured voltage differences across both a 350 Ω ± 0.05% precision

reference resistor (Vishay Instruments) and the sample. The voltage V across the precision resistor is used to calculate current I using Ohm's law

$$V = IR \tag{2.28}$$

where R is its known resistance. The sample's resistance R_s is found from the voltage drop across it together with the measured input current, and is then converted to the material's resistivity ρ using the sample geometry

$$\rho = R_s \frac{A}{L} \tag{2.29}$$

with the known cross-sectional area A and length L. A 0.5 V peak-to-peak AC excitation voltage was generated by a programmable synthesized function generator (Wavetek™ model 278) and tested across 100 Ω and 350 Ω resistors to verify its accuracy. The measured resistance R did not vary noticeably when a range of excitation voltages were applied; and a final value of 0.5 V peak to peak was selected to take best advantage of the voltmeter's sensitivity. Some authors have previously reported non-linear contact impedance effects (e.g., Sumner 1976); these are not believed to be important here because the ends of the samples were machined flat to better than 25 μm (1/1000th inches). The contacting end-caps were also machined flat ensuring uniform contact allowing for uniform current injection through the sample.

The constraints of the experiment within a pressure vessel necessitated that a 2-electrode configuration be employed; and consequently, the endcaps were used both for the electrodes and for the ultrasonic buffers. This is problematic in that electrode polarization must be considered. Following procedures described by Wang et al. (2009), the system was tested over a range of frequencies from 1 Hz to 1 MHz, and similar to their findings the polarization was not problematic at a frequency of 10 kHz. To further validate use of this frequency, the resistivity was measured

at a range of frequencies using a 2-electrode configuration at room conditions on the alumina sample saturated with a NaCl electrolyte (2% by weight ~ 3.37 S/m). This was compared to a single measurement at 100Hz using a four-electrode method. The 2-electrode resistivities diverge significantly from the 4-electrode resistivity at frequencies below 1 kHz due to electrode polarization effects (Fig. 2.5), but the values are the same above this frequency. The 2-electrode resistivities remain slightly higher but according to Chelidze and Gueguen (1999) this small variation is probably due to contact impedance effects.

In the measurement set-up, one end-cap is electrically attached to the pressure vessel and this provides a virtual ground. The other end cap remained unconnected to the pressure vessel ensuring that no short circuiting occurred. The end caps are made of an aluminum alloy, which was a concern due to its susceptibility to corrosion. However, the electrolytes used were relatively dilute composed of NaCl dissolved in distilled water; and no obvious corrosion (pitting etc.) was detected on the end caps at any point in time during the experiments. Reproducibility of measurements over time was also monitored to see if there were changes to measured physical properties that could not correspond to changes in the sample.

It is important to mention how the reported formation factors $F = R_w/R$ were obtained. Normally, for the sake of redundancy this is done by making multiple measurements of R at differing salinities R_w. Here, only one salinity (2% by weight or ~20000 ppm) was used but this is considered sufficiently high that it should be near the high salinity asymptote of the formation factor vs. electrolyte conductivity graph (Weller et al. ,2013). Making a single measurement risks underestimating F; regardless the values obtained here are similar to those found in other studies on Berea sandstone.

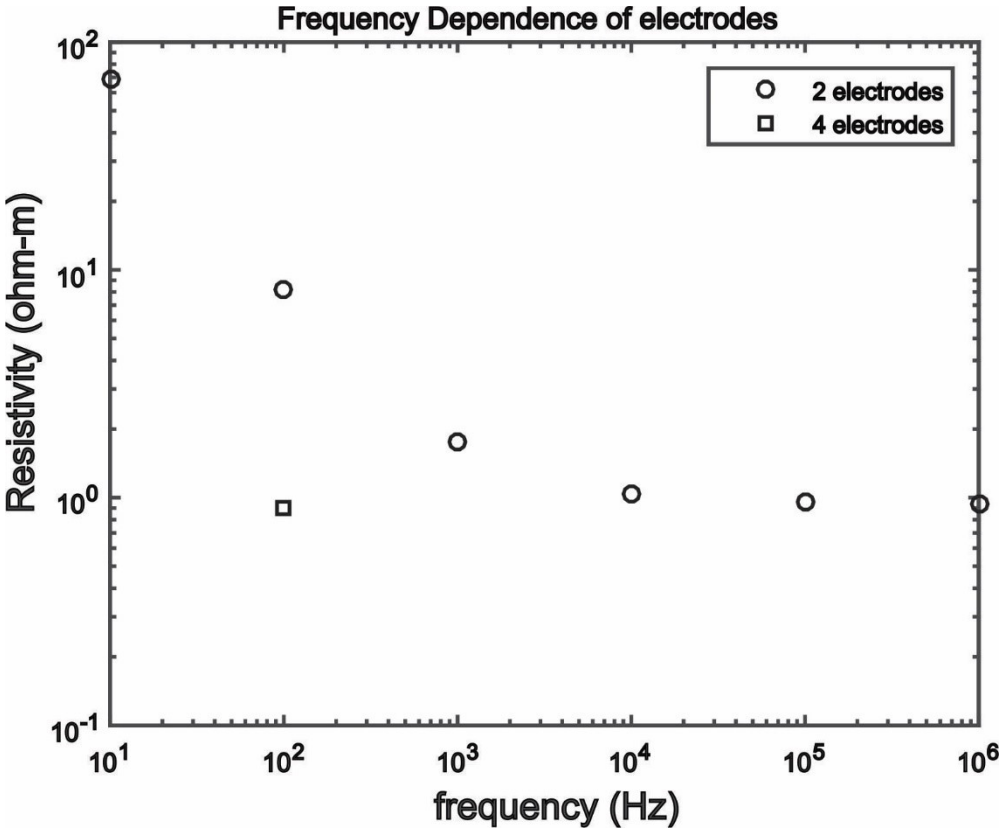

Figure 2.5. Impedance magnitude as a function of frequency for multiple 2 electrode measurements and a single 4 electrode measurement on a ceramic sample.

2.3.3) Sample Description

Measurements were made on two contrasting samples previously characterized by Yam (2011) including a highly-porous sintered alumina (Soil Moisture Equipment Corporation) and a natural Berea sandstone. The synthetic alumina is composed primarily of shards of alumina (Al_2O_3) with a binder material; this makes a porous solid that is almost devoid of crack-like porosity. The natural Berea sandstone sample is composed primarily of quartz grains with some trace amounts of clay material that binds the grains together. As described by Prasad and Manghnani (1997), the Berea sandstone consists of angular quartz grains with many uncemented and crack-like grain boundaries that behave as microcracks. The synthetic alumina sample, however, is dominated by

more equant porosity. Yam (2011) carried out a variety of petrophysical measurements to characterize these materials as summarized in Table 2.1.

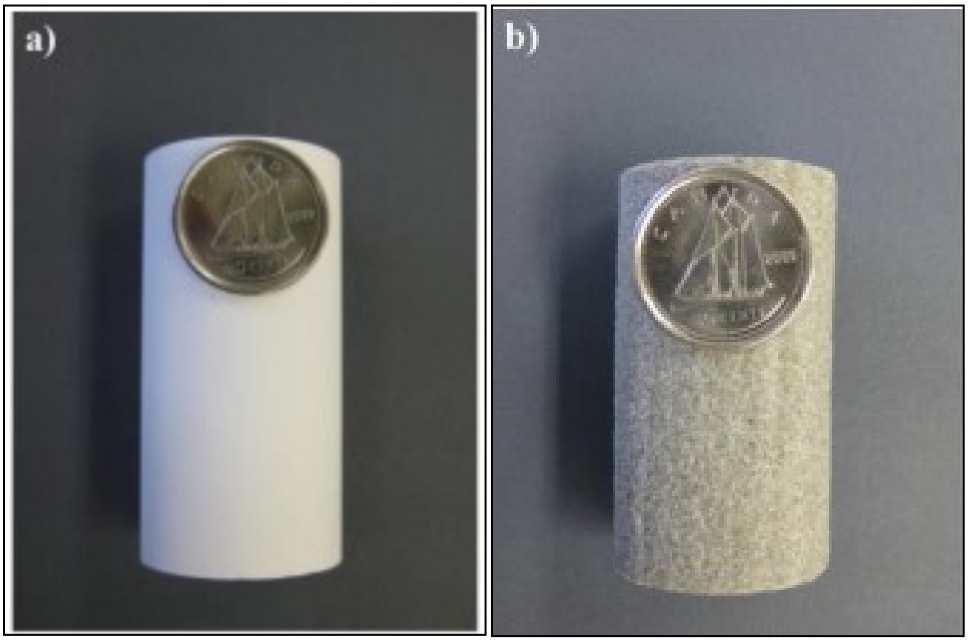

Figure 2.6. Samples used in the laboratory tests. a) sintered alumina. b) Berea sandstone. Canadian ten cent coin with 18.03 mm diameter for scale.

Table 2.1. Petrophysical properties of 2 samples used in this study

Property	Alumina rod	Berea Sandstone
Bulk Density (g/cc)	1.55	2.15
Grain Density (g/cc)	3.70	2.64
Porosity	0.584	0.186
Air permeability (mD)	96.94	237.65
Modal pore size (μm)	2.06	11.33

2.4) Experimental procedure

2.4.1) Dry measurements

Ultrasonic pulse transmission measurements were first conducted on the dry samples with the pore pressure inlet vented to the atmosphere while the confining pressure was cycled from 1 MPa to 40 MPa.

2.4.2) Saturated measurements

A weak NaCl brine (2% NaCl by weight) was prepared. While the sample remained in the pressure vessel, its pore volume was then subject to vacuum through the pore pressure inlet. The sample was then saturated by placing the inlet into the brine and opening it allowing the brine to be forced into the pore spaced driving by both the atmospheric pressure and capillary forces. In practice, additional brine was further pushed into the sample before pore pressure could be maintained.

Once the sample was saturated, the confining pressure and pore pressures were first set, respectively, to 10MPa and 1 MPa. Once the pore pressure could be maintained indefinitely the confining pressure was set to one of 10, 20 and 30 MPa. At each level of these confining pressures the pore pressure was steadily increased to within 1MPa of the confining pressure before cycling in reverse back to a minimum of P_p =1 MPa. At each increment of increasing and decreasing pressure, P and S waveforms were recorded from which the transit times and consequent wave speeds found. Additionally, electrical measurements were also sequentially obtained at each pressure increment to ensure the samples are under the exact same Pressure –Temperature conditions.

When the pressure is increased there is an unavoidable increase in temperature of the system due to adiabatic or other (Stesky, 1986) effects. The system must therefore be allowed some time to equilibrate, and in general, to accommodate this a minimum of 10 minutes elapsed between measurements. As an additional check we ensured that the arrival times of ultrasonic pulses were not changing and that the temperature was stable when the measurements were recorded. The measurements are time consuming, and each set was carried out over the course of 48 hours. The same end caps were used for both samples. After each run the end caps were inspected for any visible signs of corrosion. As a further test, the first and last electrical measurements were carried out at the same conditions. All checks suggested that corrosion was not a problem.

2.5) Results

The observed P- and S-wave speed pressure dependencies under dry conditions for the two samples, tabulated in Appendix I, behave quite differently (Fig. 2.7). The alumina ceramic sample displays only weakly pressure dependent wave speeds below 10 MPa and above this pressure remains essentially constant. The Berea sandstone, in contrast, shows considerable pressure dependence with P- and S-wave speeds both increasing by 29%, over the range of applied confining pressures. This behaviour is well known in Berea sandstone and is attributed to the progressive closure of the micro-crack porosity. Also seen in Fig 2.7 is hysteresis is the velocities between loading and unloading cycles. This is sometimes attributed to crack like pores not being fully recovered (opened or closed) from the previous cycle but may also be due to some plastic deformation that occurs during pressure cycling.

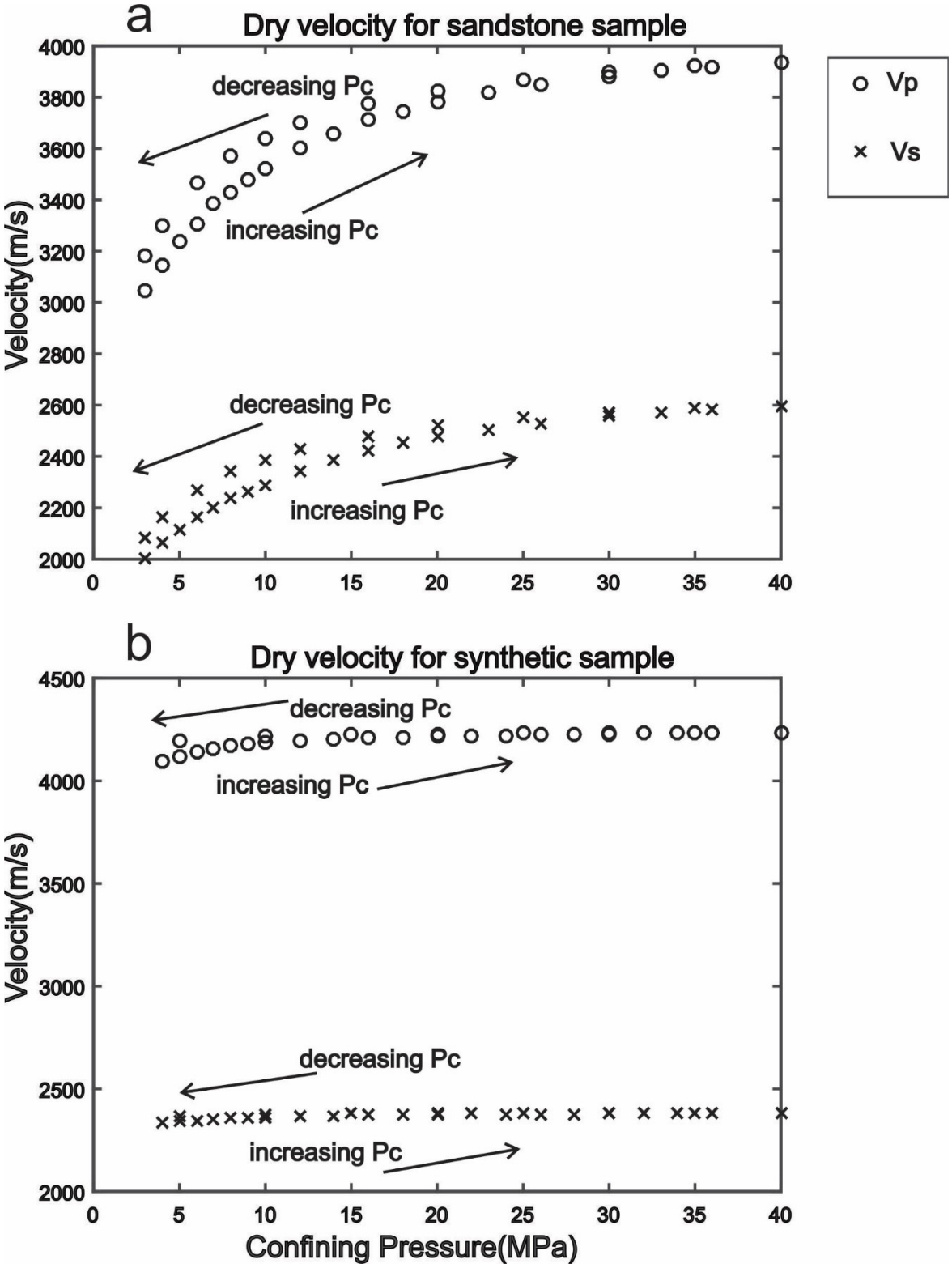

Figure 2.7. P and S-wave velocities as a function of confining pressure under dry conditions for a) Berea sandstone and b) alumina ceramic.

The pressure dependent behaviour of the P- (Fig. 2.8a) and S-wave (Fig. 2.8b) speeds under saturated conditions, when plotted as a function of P_d, is largely similar to that for the dry measurements. Interestingly, the addition of fluid to the synthetic alumina sample largely eliminated pressure dependence. For the velocity measurements shown in Fig. 2.8 (a and b), for the ceramic rod, the difference in velocity between the highest and lowest differential pressures is less than 25 m/s for P waves and less than 6m/s for the S waves. The Berea sample wave speeds, in contrast, change considerably with P_d increasing 22% and 17% for the P- and S-waves, respectively. From these measurements it appears that the Terzhaghi effective stress law of Eqn. 2.1 is valid. This seems to be satisfied as the resistivities and wave speeds measured remain nearly constant at the same P_d (Fig. 2.8).

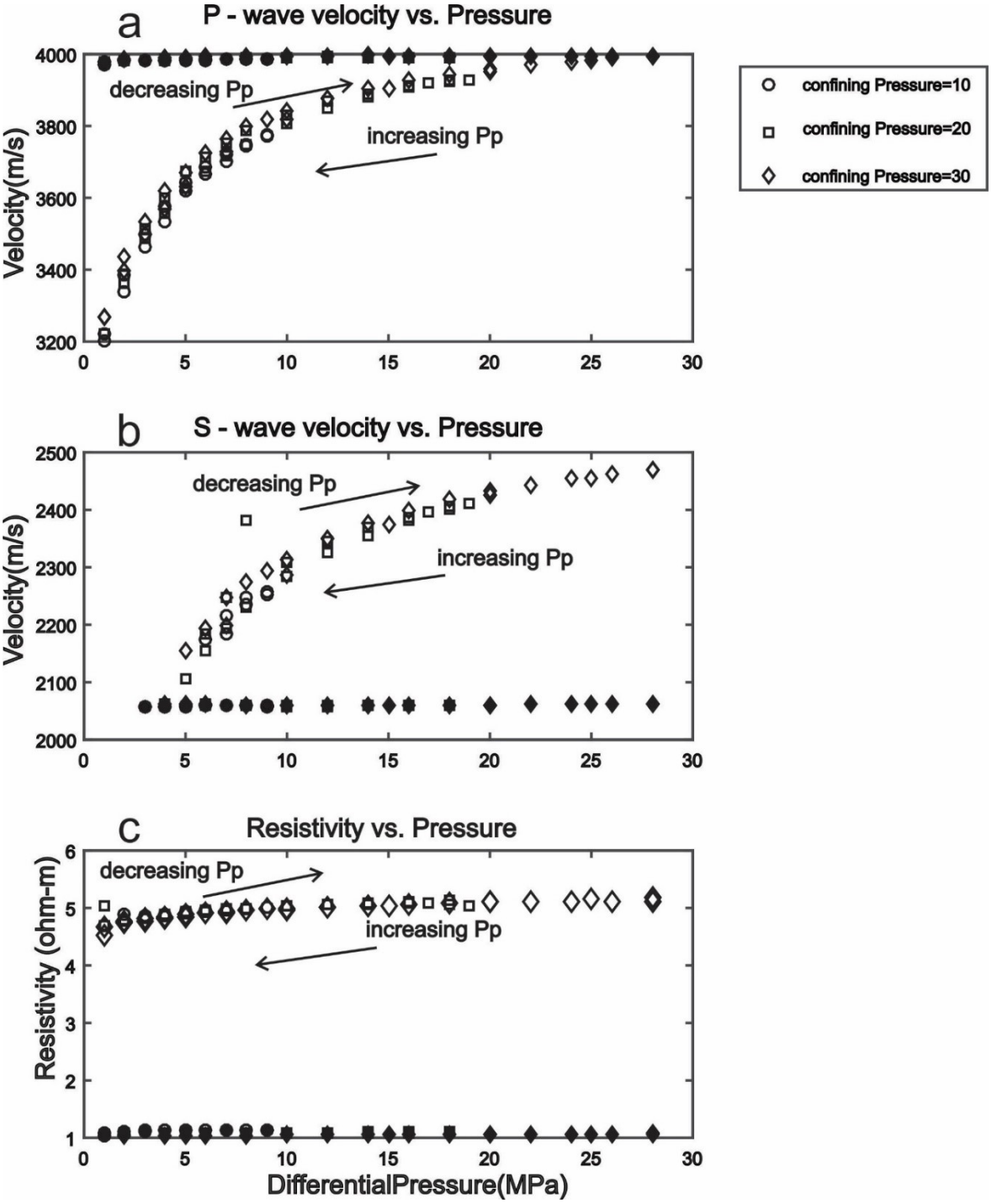

Figure 2.8. a) Saturated P- wave velocities, b) saturated S-wave velocities, and c) saturated electrical resistivity as a function of differential pressure for all confining pressure runs. Open markers indicate that the data is from the sandstone and filled markers are used for the ceramic data.

The observed resistivities (Fig. 2.8c) indicate different pressure dependencies for both samples. The Berea sandstone resistivity increases by ~16% while that for the alumina ceramic changes by ~8%. This latter change is somewhat unexpected given the lack of pressure dependence seen in the wave speeds for this sample. It should be noted that the changes in resistivities at 20 MPa and 30 MPa were both ~3%. We believe this discrepancy is due to the data collection process. This is because the 10 MPa run was done last for this sample and it is believed to have sustained some damage at the edges where the endcaps connect to the sample. This would have slightly increased the contact impedance between the electrode and sample. The relief of pressure going from 30 MPa down to 20 MPa and then 10 MPa also may have caused slightly bigger contact impedance at each pressure as it was decreased.

Nonetheless, the effective pressure dependent behaviours of both resistivity and ultrasonic velocities significantly differ between the two samples. This difference can primarily be attributed to the compliant nature of the porosity for the Berea sandstone.

2.5.1) Inversion Implementation

The electrical and wave speed pressure dependencies shown for the Berea sandstone and sintered alumina samples were inverted to obtain the model parameters Me , n , B_e, φ_c, K_0, μ_0, p and m. For the sandstone sample Eqns. 2.3, 2.4 and 2.26 were inverted for wave velocities and electrical conductivity while Eqns. 2.3, 2.4 and 2.23 were used for the ceramic. This is due to the different characteristics of the samples. The sandstone sample is heavily microcracked with a modest porosity. Based on Eqn. 2.25 this means that the inverse formation factor at zero pressure provides a rough estimate of the crack porosity. The ceramic on the other hand, has an extremely high porosity and stiff, equant wide open pores. The lack of microcracks indicated by the weak pressure dependence along with he relatively low resistivity of the sample suggest that conduction through

matrix porosity may be important to consider. Three sets of inversions were carried out for the sandstone sample and one for the ceramic. Table 2.2 summarizes the inversion showing what data was inverted, the parameters inverted for, and the number of inversions. Inversions involving only wave speeds or electrical data would not use all of the parameters. The Genetic Algorithm (function '*ga*' in Matlab™) is used to carry out the inversions. This was selected in order to avoid the objective function getting trapped in local minima which is an anticipated problem for an 8-parameter solution space. The Genetic Algorithm works on principals of natural selection. Random values are assigned to the parameters of interest subject to user defined constraints. The number of realizations of each parameter is denoted by the "population size". Modeled data is produced by the forward model that computes model velocities and resistivities based on the parameters (Eqns. 2.3, 2.4 and 2.23 or 2.26). These model results are compared to the data and the objective function supplied to the genetic algorithm is used to decide the best sets of parameters. The best parameters are then used to create a new generation of parameters. This is done until no further reduction in the objective function is achieved (to within some user defined tolerance). Processes such as random mutation can be incorporated to further avoid getting trapped in local minima.

Large population sizes result in long run times for the algorithm while small population sizes often result in poor fits to the data. We found that a population size of 1000 was sufficiently large to obtain a good fit to the data but sufficiently small as to avoid exhaustive runtimes. In general, a larger population size is desirable, but in order to carry out the hundreds of inversions for the sandstone we found that 1000 was optimal. The various inversions are later used to analyse the non-uniqueness of each parameter by examining parameter distributions. For the alumina ceramic. Only one inversion was carried out with a population size of 10,000.

Following Gao and Gibson (2012), Gassmann (1951) fluid substitution was used to provide a value for the elastic moduli for the material in the "uncracked" state. The effect of pressure on the velocity of the saturating electrolyte was calculated using Batzle and Wang's (1992) expressions (specifically their Eqn. 29). For inverting the resistivities Eqn. 2.26 is used as the forward model.

The objective function

$$misfit = \frac{A + B + \lambda C}{3} \tag{2.30}$$

where λ is a scaling factor and,

$$A = \left\| V_{p,measured} - V_{p,modeled} \right\|$$

$$B = \left\| V_{s,measured} - V_{s,modeled} \right\|$$

$$C = \left\| \sigma_{measured} - \sigma_{modeled} \right\|,$$

minimized the difference between model results and the observed results in a least square sense. In order to account for the large magnitude differences between the velocities and conductivities, a scaling factor of λ =70,000 was assigned to the conductivities. This is almost one order of magnitude higher than difference between the conductivity and velocity data (conductivity on the order of 10^{-1} and velocities on the order of 10^{4}). Other weighting factors were tested, and any values within an order of magnitude of this made little difference to the qualitative appearance of the fit. The reason that the weight is higher than the required amount to make up the difference in magnitude between the conductivity and velocity data is because the inversion relied on four velocity data sets (Dry P wave, Dry S wave, saturated P wave and saturated S wave) but included only the single suite of conductivity measurements.

In the inversions the both specimens are assumed to be isotropic. This is a common assumption for Berea sandstone although it has been shown to be weakly anisotropic (Prasad and Manghnani, 1997). There is not previous work to suggest weather the sintered alumina is completely isotropic in mineral orientation and pore space orientation and so we assume isotropy in the following. It should be noted that the use of Gassmann fluid substitution allows the user to investigate the effects of different fluids if desired.

Table 2.2- Summary of inversions carried out on different data

Sample	**Data Inverted**	**Number of inversions**	**Parameters inverted for**
Berea Sandstone	Velocity	400	Me , n , B_e, φ_c, K_0, μ_0
Berea Sandstone	conductivity	400	Me , n, φ_c, p
Berea Sandstone	Velocity and conductivity	400	Me , n , B_e, φ_c, K_0, μ_0, p
Alumina Ceramic	Velocity and conductivity	1	Me , n , B_e, φ_c, K_0, μ_0, p, m

2.5.2) Inversion results

Four hundred inversions for seven parameters (Me , n , B_e, φ_c, K_0, μ_0 and p) were carried out for the sandstone sample inverting Eqns. 2.3, 2.4 and 2.26 to obtain modeled ultrasonic wave velocities and electrical conductivity. Further, three separate inversions were executed using different elements of the datasets as shown in Table 2.2. This was done to assess what effect including the different data sets had on the parameter distributions for the sandstone. One inversion on the ceramic sample was carried out for eight parameters (Me , n , B_e, φ_c, K_0, μ_0, p, m). The

following constraints were applied to the inversion. The K and μ obtained from the velocities measured at the highest confining pressures on the dry samples was used to estimate a lower bound to the background K_o and μ_0 moduli, while an arbitrarily high value of 70 GPa was taken for the upper bound. φ_c was allowed to vary between zero and the total porosity (φ_T) for each sample (Table 2.1). The parameters Me and B_e were difficult to constrain, and based on the results of Gao and Gibson (2012), ranges of 10 GPa $\leq M_e \leq$ 100 GPa and $0 \leq B_e \leq 1$ GPa^{-1} were eventually adopted for the Berea Sandstone. The same bounds were used or the ceramic sample with the exception of the closure modulus which was assigned a range of 1 GPa $\leq M_e \leq$ 500 GPa since there are no analogous samples to compare it to from Gao and Gibson (2012). Parameters Me and B_e are therefore the least constrained. The exponent n was initially set with an upper bound of 100 but this was reduced to 10 upon inspection of preliminary results (lower bound set to 0). These constraints were not necessary to achieve a good solution but allowed us to use smaller population sizes in order to speed up the computation time. The results of the joint inversions are shown with the fitted curves in Fig. 2.9 and Fig. 2.10 for the sandstone and ceramic respectively. The parameters obtained in Figs. 2.9 and 2.10 are summarized in Table 2.3. Figs. 2.11 and 2.12 show inversion results when inverting the velocity and resistivity separately.

Table 2.3. Summary of parameters obtained for results shown in Figs. 2.9 and 2.12.

Sample	$\boldsymbol{Me(GPa)}$	$\boldsymbol{n}$	$\boldsymbol{B_e(GPa)^{-1}}$	$\boldsymbol{\varphi_c}$	$\boldsymbol{K_0(GPa)}$	$\boldsymbol{\mu_0(GPa)}$	$\boldsymbol{p}$	$\boldsymbol{m}$
Sandstone	57.2	.525	1.11 x 10^{-2}	0.0649	23.5	19.2	.544	N/A
Ceramic	1.47	0.111	1.89 x 10^{-2}	0.00642	20.4	9.14	0.470	2.33

Sandstone (velocities)	48.3	0.278	1.23 x10^{-2}	0.109	30.3	19.9	N/A	N/A
Sandstone (electrical conductivity)	98.3	4.07	N/A	0.0665	N/A	N/A	0.994	N/A

For the ceramic sample, it is difficult to get a satisfactory fit to the data and we were unable to do so here. Fig. 2.10 shows modeled and measured results with root mean square (rms) error values of 39.78 m/s, 3.496 m/s and 0.0075 ohm-m) for the dry velocities, saturated velocities and resistivity respectively. The rms error values are all reasonable however the graphs do not qualitatively agree and the pressure dependence of the resistivity is underestimated. This could be due to the unusual nature of the sample. It is highly porous with no sign of microcracks and contains a binding material, which we know little about. The changes in resistivity are also not correlated with velocity in this sample since the velocity does not change much for the saturated velocities. Uncorrelated changes may suggest the mechanism for change in the properties is unrelated and the model is invalid for the sample.

A good fit is seen for the sandstone data and this could be achieved with using any subset of the data set. Fig. 2.9 shows modeled and measured results with rms error values of 59.0 m/s, 20.8 m/s and 0.0471 ohm-m for the dry velocities, saturated velocities and resistivity respectively. Fig. 2.11 shows modeled and measured results for velocities with rms error values of 54.89 m/s and 23.99 m/s for dry and saturated velocities respectively. Fig. 2.12 shows the modeled and measured results for sandstone resistivities with and rms error value of 0.0329 ohm-m.

Although good fits can be obtained, it is useful to examine how well determined each of the parameters were in the various inversions as non-uniqueness is a common problem in rock physics modeling. This is discussed in the next section along with how the result can influence rock physics modeling.

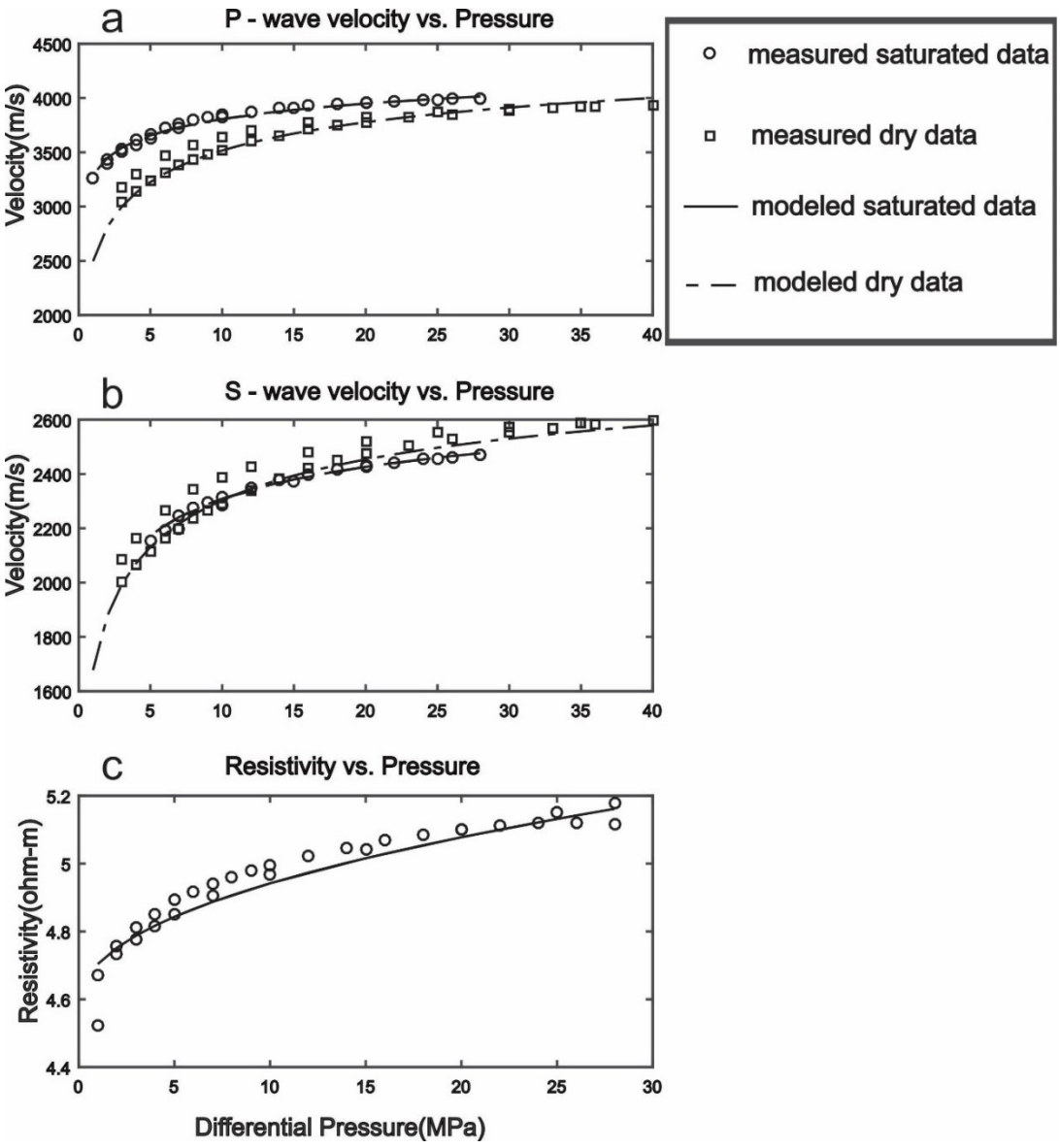

Figure 2.9. Berea sandstone comparison of measured results to modeled results for (a) P wave velocities under dry and saturated conditions, (b) S wave velocities under dry and saturated conditions and (c) electrical resistivity for measurements under saturated conditions.

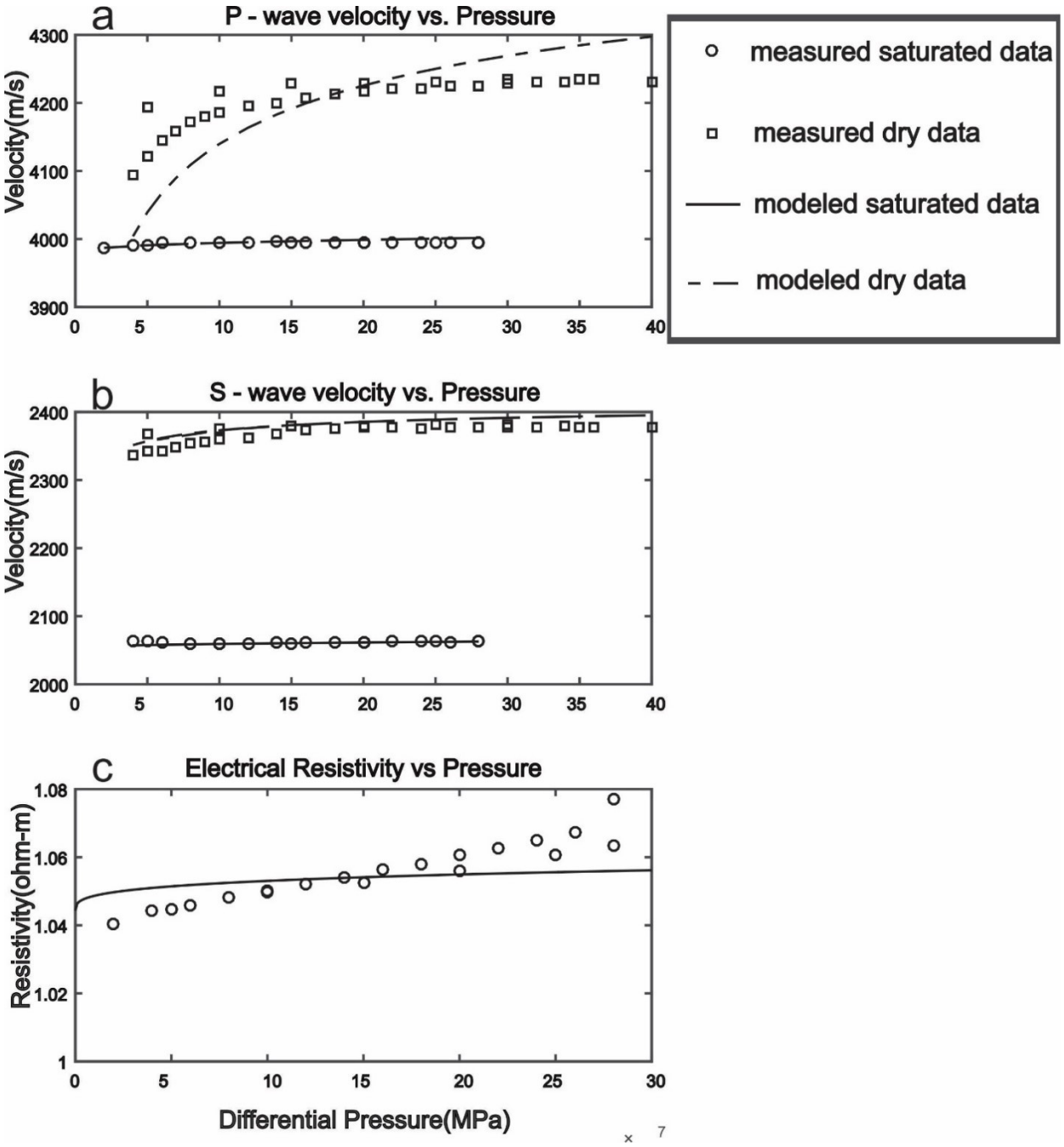

Figure 2.10 Alumina ceramic comparison of measured results to modeled results for (a) P wave velocities under dry and saturated conditions, (b) S wave velocities under dry and saturated conditions and (c) electrical resistivity for measurements under saturated conditions.

c

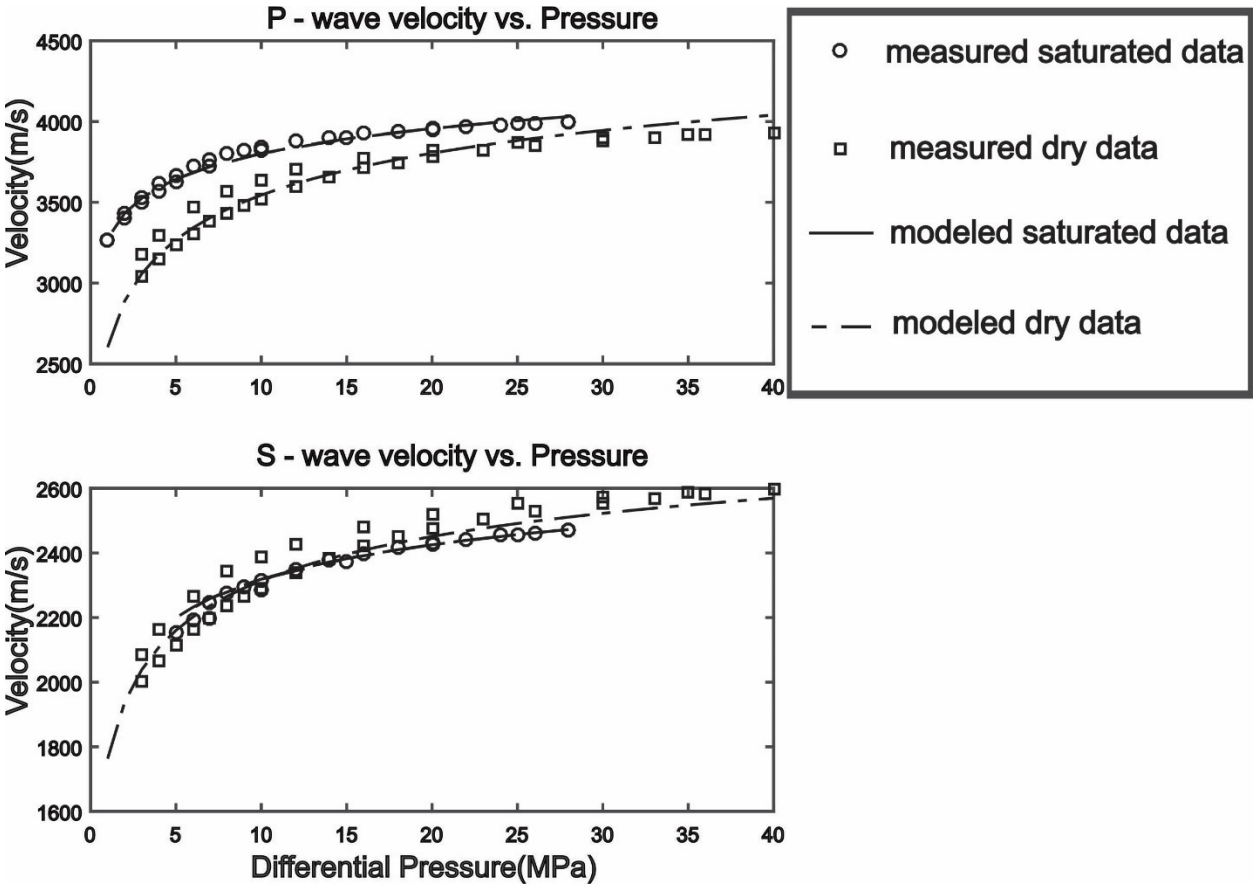

Figure 2.11. Berea sandstone comparison of measured results to modeled results for (a) P wave velocities under dry and saturated conditions and (b) S wave velocities under dry and saturated conditions.

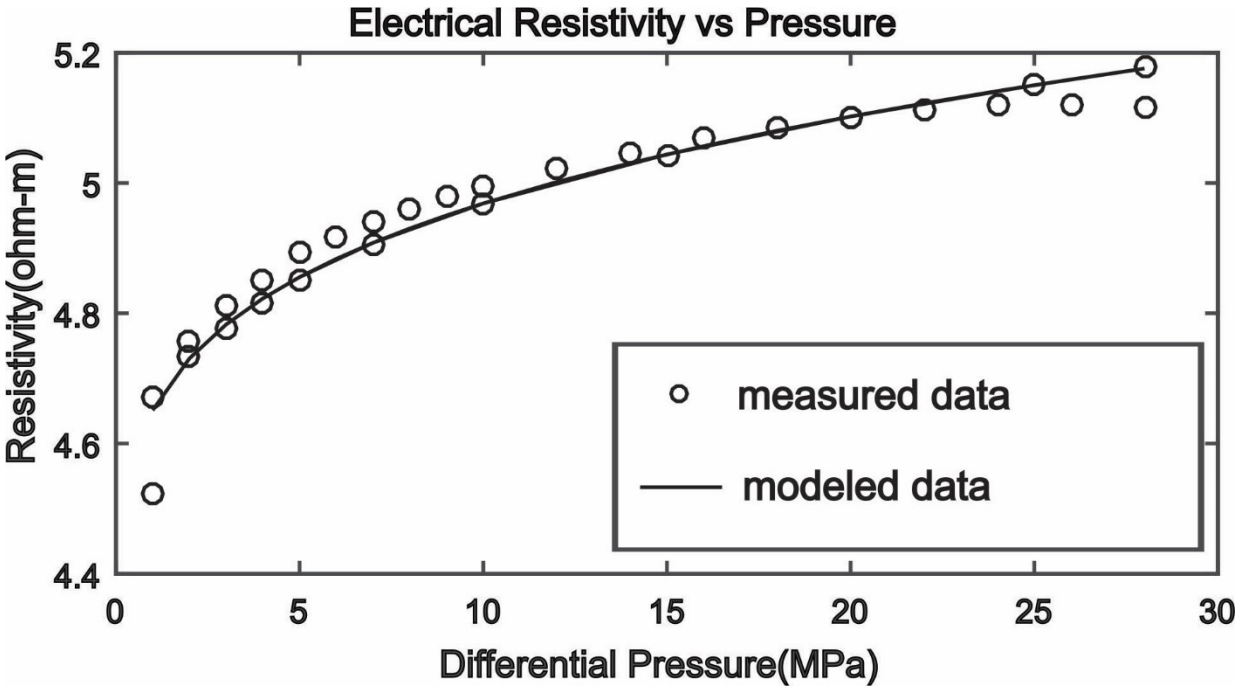

Figure 2.12. Berea sandstone comparison of Modeled to measured P electrical resistivity under saturated conditions.

2.6) Discussion

In this section we discuss the limitations of the proposed model. We focus on the issues of non-uniqueness and the Poisson's ratio for the material making up the elastic hemispheres.

One admitted problem arising from the Gao and Gibson (GG) model of pressure dependent crack compliance is the number of parameters required to be fit causing the parameters to be non-unique. Gao and Gibson (2012) only inverted ultrasonic velocities, and on the basis of their observations suggested that the closure modulus (M_e) and the crack porosity were least well constrained.

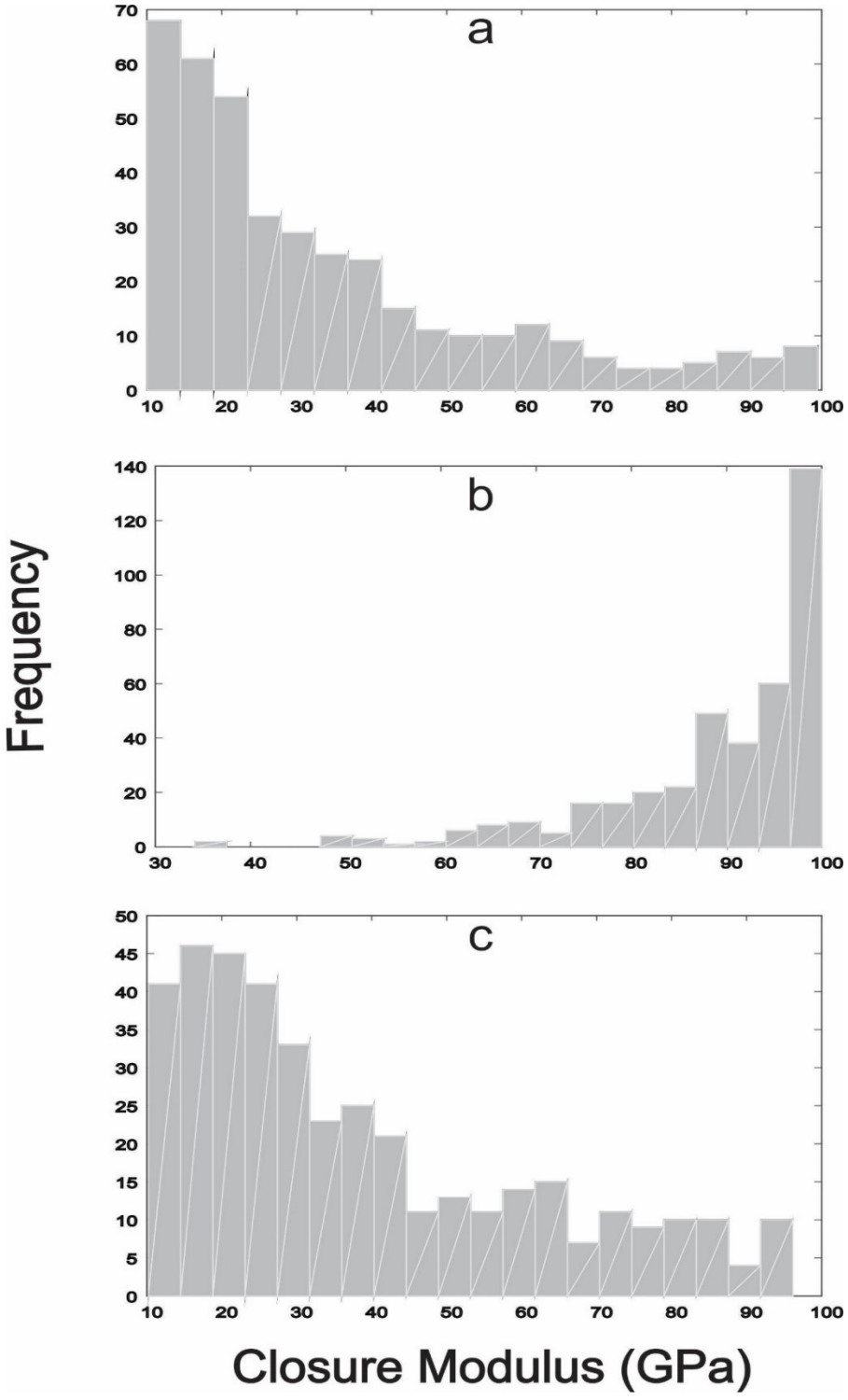

Figure 2.13. M_e distributions when inverting (a) velocity data, (b) conductivity data and (c) both velocity and conductivity data. Histograms were calculated from the 400 inversions done for each dataset.

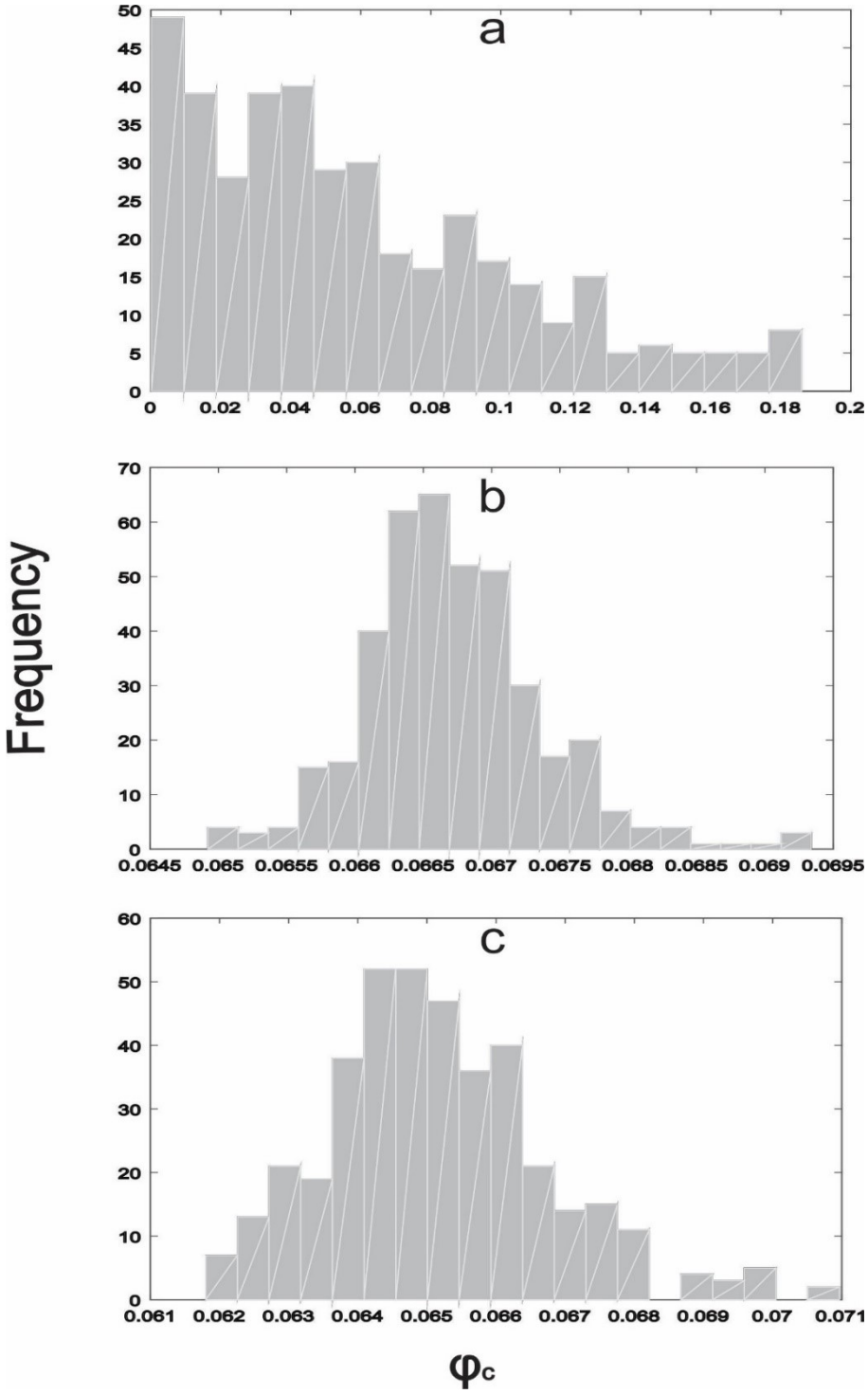

Figure 2.14. φ_c distributions when inverting (a) velocity data (b) conductivity data and (c) both velocity and conductivity data. Histograms were calculated from the 400 inversions done for each dataset.

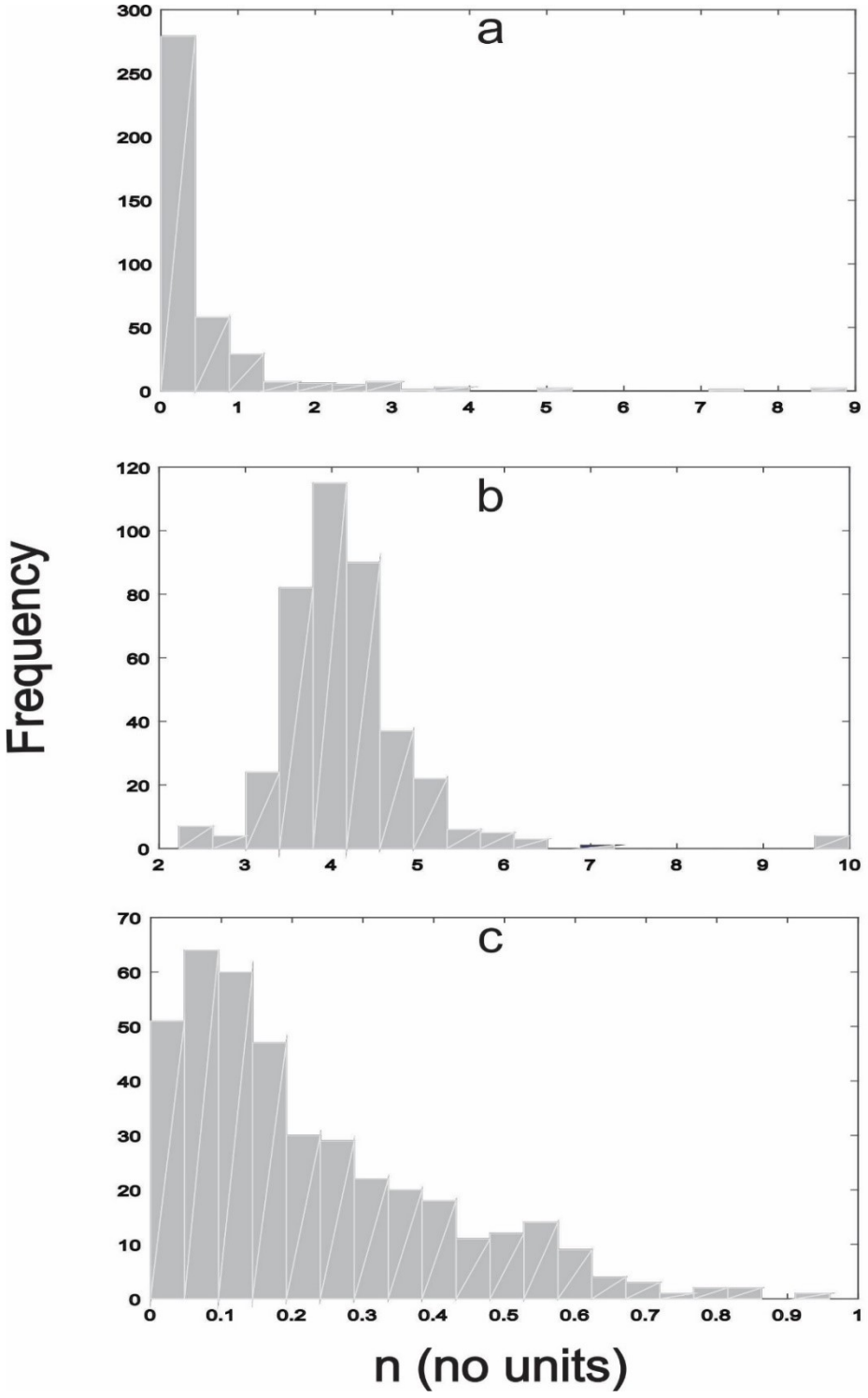

Figure 2.15. n distributions when inverting (a) velocity data, (b) conductivity data and (c) both velocity and conductivity data. Histograms were calculated from the 400 inversions done for each dataset.

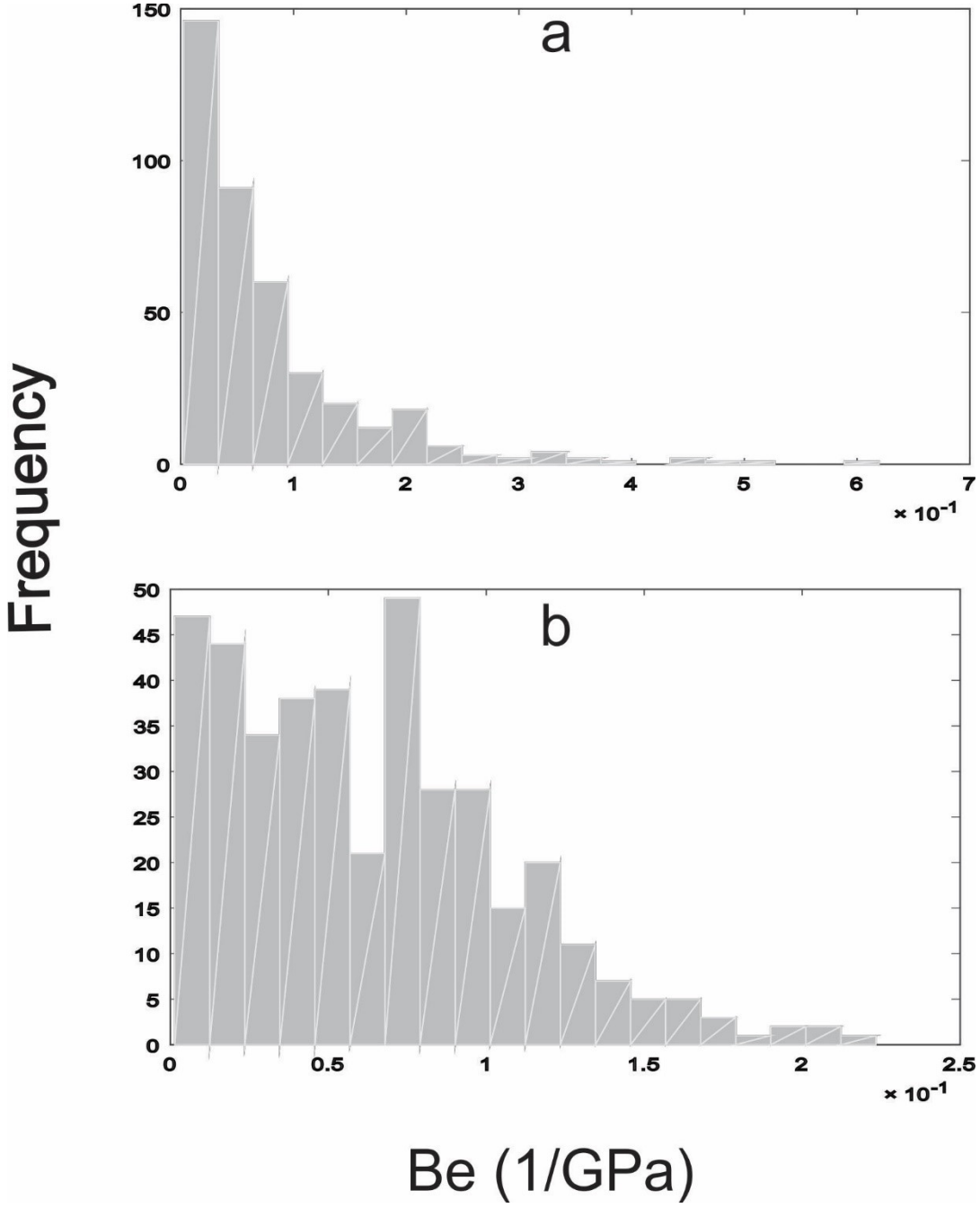

Figure 2.16. B_e distributions when inverting (a) velocity data and (b) velocity and conductivity data. Histograms were calculated from the 400 inversions done for each dataset.

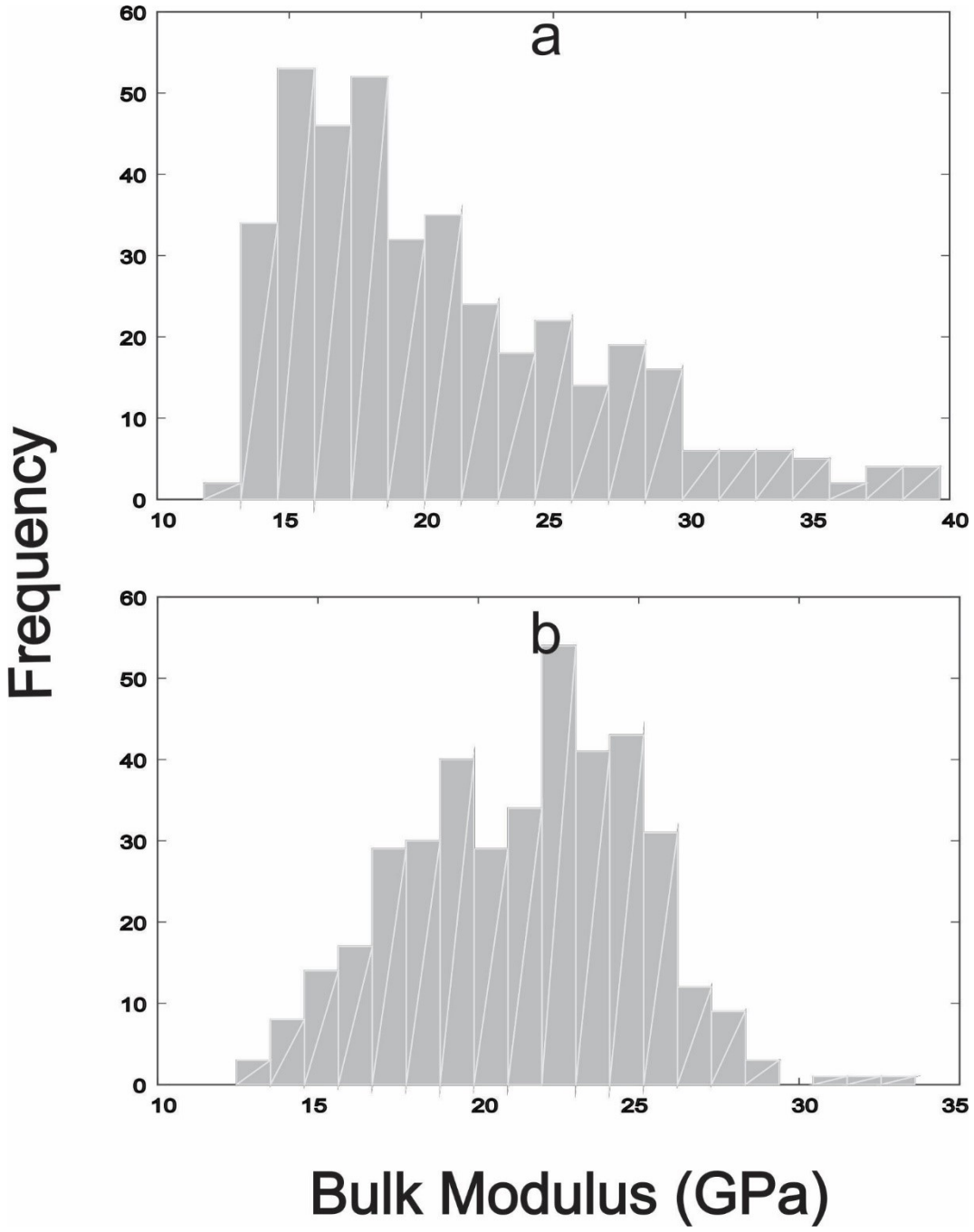

Figure 2.17. K_0 distributions when inverting (a) velocity data and (b) both velocity and conductivity data. Histograms were calculated from the 400 inversions done for each dataset.

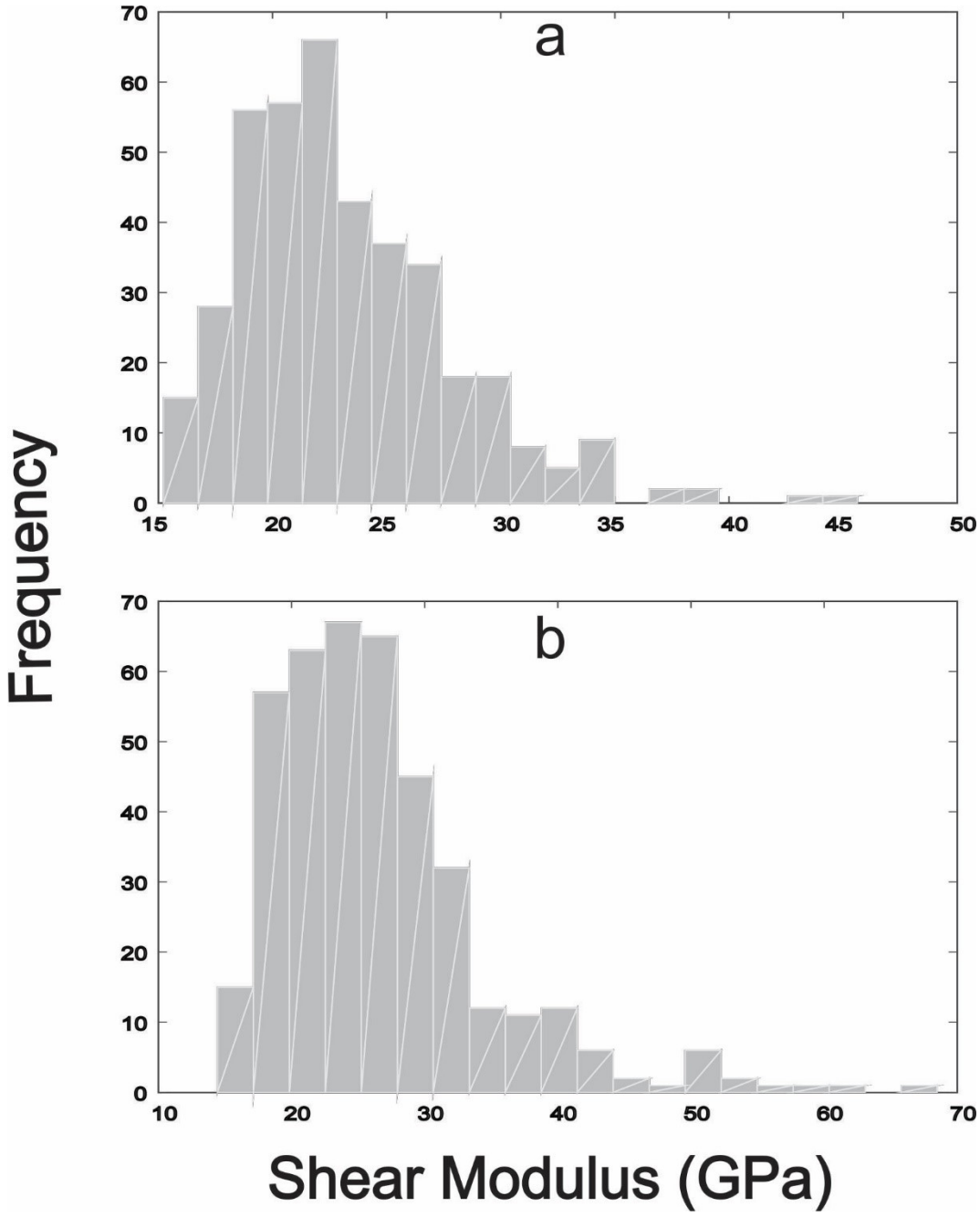

Figure 2.18. μ_0 distributions when inverting (a) velocity data and (b) both velocity and conductivity data. Histograms were calculated from the 400 inversions done for each dataset.

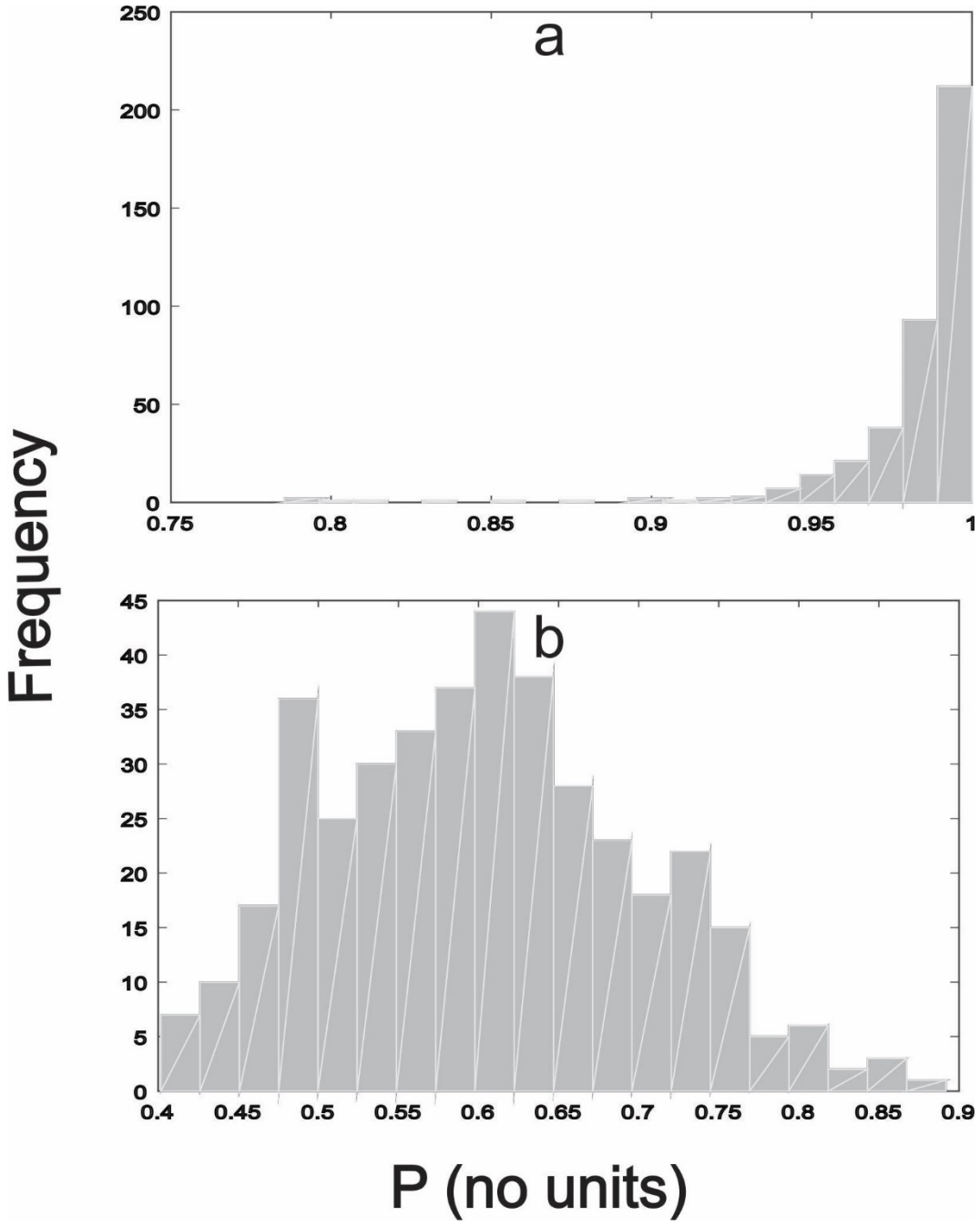

Figure 2.19. p distributions when inverting (a) conductivity data and b) both velocity and conductivity data. Histograms were calculated from the 400 inversions done for each dataset.

Figs. 2.13 to 2.19 show the distributions for the inverted parameters for each of the 400 inversions on Berea sandstone. Fig. 2.13 shows that the distribution of parameter M_e is quite similar for both

inversions which include velocity data. Although the distribution is broad, the mean of the distribution closer to the lower end of the parameters. The distribution obtained with only the electrical data is notably different and heavily favours values toward the higher end of the parameter distribution. Fig. 2.14 shows that resistivity has the greatest impact on the crack porosity. The parameter distributions for the conductivity inversion and joint inversions shown are notably different from the parameter distribution for the velocity data. Goa and Gibson's result showed that the crack porosity was poorly constrained when only using velocity data. The distribution of parameter n is similar for the inversions involving velocity data and both data sets but is different for the electrical data. Parameter B_e (Fig. 2.16) only applies to the velocity data and so is equally well determined by both data sets. Figs. 2.17 and 2.18 show that the "uncracked" moduli remain well determined as seen in Goa and Gibson (2012). Parameter p (Fig. 2.19) only fits the electrical data but its distribution changes dramatically when fitting the joint inversion data compared to the conductivity data.

The differences in the distributions obtained from the inversion of different datasets suggests that either dataset on its own is will likely give different parameters for the same rock. This non-uniqueness is a common problem in geophysics and highlights the need for joint inversions like the one shown here. The electrical data constrains the crack porosity more than any other parameter. This in turn causes other parameters to adopt different values in order to fit the data. Assuming the physical description is sufficiently accurate, this would suggest that both data sets offer complementary constraints to the inversion. The closure modulus is most well constrained by the velocity data while the crack porosity is best constrained by the electrical data. It is also apparent that there are parameter trade-offs. A proper sensitivity analysis would be necessary to quantify them all but it is clear that for the electrical data, a high value for parameter p favours a

higher value for the closure modulus. Investigation of the significance of these trade-offs will be left to future work.

Another relevant point made by Gao and Gibson (2012) was the fact that their background Poisson ratios $v_{0,}$ which are related to the normal to tangential crack compliances as shown in Eqn. 2.31, were not always realistic.

$$\frac{B_N}{B_T} = \frac{1 - v_0}{1 - \frac{v_0}{2}} \tag{2.31}$$

We found that our inversions agreed with his findings that the ratio $\frac{B_N}{B_T}$ is less than 1 and decreases with differential pressure however it was greater than 1 for a small number of them. Although the Poisson ratio values are not always realistic (changing from one inversion to another), the ratios agree with Gao and Gibson (2012). However, many inversions give Poisson's ratios within reasonable bounds. This shows that the unrealistic Poisson's ratio is caused by the non-uniqueness of the inversion. This can be included as a constraint for the genetic algorithm but in practice it greatly increased computation time. Without this constraint, most inversions result in a Poisson's ratio between 0.4 and 1; it must be noted that unless the material is anisotropic Poisson's ratio cannot exceed 0.5. This means that most of the results were unrealistic, but the results shown for Fig. 2.9 have a Poisson's ratio of 0.36. The Poisson's ratio for Figs .2.10, 2.11 and 2.12 are is 0.83, 0.09 and 2.10 respectively. It is interesting to note that although all the sandstone data could be fit with a model with a realistic Poisson's ratio, none of the inversions using only electrical data produced realistic Poisson's ratios. Workers are therefore advised to use this as a constraint if conducting similar inversions using a genetic algorithm.

2.7) Conclusions

We conducted a series of electrical resistivity and ultrasonic velocity measurements on two very different porous samples. The first was natural sandstone with a large amount of compliant porosity and the second was a synthetic porous media with very stiff equant porosity. The difference in the responses of the two samples in part demonstrates the difference in pressure dependent behaviour introduced by crack-like porosity. Gao and Gibson's (2012) model for pressure dependent crack compliances was integrated with crack geometries suggested by Stesky (1986) to account for the similar pressure dependencies of electrical conductivity. This integration allows electrical and seismic data sets to be jointly inverted to characterize the cracks in the material. Although this problem remains inherently nonunique, the electrical data added a strong constraint on the crack porosity parameter which is the most useful parameter in the model used to fit the data.

The relations shown here require more testing against a variety of data sets. However, they offer the potential to reduce ambiguity in data interpretation by describing how two measurable properties can be expected to vary together as pressure changes in a reservoir. This may be useful when trying to discern the effects of pressure changes in a reservoir from changes due to other factors such as chemical reactions, damage or changing fluid properties.

Future work includes extending the model to the anisotropic conductivity. Kachanov (1992) suggested that crack density tensors like that used in Gao and Gibson's model be incorporated into electrical and fluid flow models to model the effect of fractures but the problem has seen little development since.

Acknowledgements – This work was funded within Dr. Schmitt's CMC grant. Special thanks to Randolf Kofman for his assistance with the lab work.

2.8) Appendix

Table 2.A1- Measured velocity and resistivities for saturated samples at various confining pressure and pore pressure. Note Cycle indicates whether the Pore pressure was being increased (up) or decreased (down) during the run.

Sample	Cycle	Confining Pressure (MPa)	Pore Pressure (MPa)	V_p (m/s)	δV_p (m/s)	V_s (m/s)	δV_s (m/s)	ρ (Ohm-m)	$\delta\rho$(Ohm-m)
Berea Sandstone	Up	10	1	3771	16	2252	6	5.01	0.03
Berea Sandstone	Up	10	2	3744	16	2236	6	4.99	0.03
Berea Sandstone	Up	10	3	3703	16	2184	6	4.96	0.03
Berea Sandstone	Up	10	4	3665	16			4.94	0.03
Berea Sandstone	Up	10	5	3620	16			4.91	0.03
Berea Sandstone	Up	10	6	3535	15			4.88	0.03
Berea Sandstone	Up	10	7	3462	15			4.83	0.03
Berea Sandstone	Up	10	8	3338	14			4.78	0.03
Berea Sandstone	Up	10	9	3223	14			4.69	0.03
Berea Sandstone	Down	10	9	3201	14			4.70	0.03
Berea Sandstone	Down	10	8	3386	15			4.90	0.03
Berea Sandstone	Down	10	7	3500	15			4.86	0.03
Berea Sandstone	Down	10	6	3578	15			4.90	0.03
Berea Sandstone	Down	10	5	3642	16			4.93	0.03

Berea Sandstone	Down	10	4	3685	16	2174	6	4.96	0.03
Berea Sandstone	Down	10	3	3720	17	2215	6	4.98	0.03
Berea Sandstone	Down	10	2	3750	17	2247	6	4.99	0.03
Berea Sandstone	Down	10	1	3774	17	2258	6	5.01	0.03
Berea Sandstone	Up	20	1	3930	18	2410	6	5.04	0.03
Berea Sandstone	Up	20	2	3926	18	2406	6	5.07	0.03
Berea Sandstone	Up	20	3	3920	18	2396	6	5.08	0.03
Berea Sandstone	Up	20	4	3913	18	2388	6	5.08	0.03
Berea Sandstone	Up	20	6	3890	18	2368	6	5.07	0.03
Berea Sandstone	Up	20	8	3867	17	2346	6	5.05	0.03
Berea Sandstone	Up	20	10	3829	17	2308	6	5.03	0.03
Berea Sandstone	Up	20	12	3786	16	2383	6	5.00	0.03
Berea Sandstone	Up	20	13	3753	16	2247	6	4.98	0.03
Berea Sandstone	Up	20	14	3714	16	2184	6	4.96	0.03
Berea Sandstone	Up	20	15	3674	16	2105	6	4.94	0.03
Berea Sandstone	Up	20	16	3600	15			4.90	0.03
Berea Sandstone	Up	20	17	3514	15			4.85	0.03
Berea Sandstone	Up	20	18	3386	14			4.79	0.03
Berea Sandstone	Up	20	19	3223	14			4.70	0.03
Berea Sandstone	Down	20	19	3223	14			5.03	0.03
Berea Sandstone	Down	20	18	3362	14			4.77	0.03
Berea Sandstone	Down	20	17	3487	15			4.83	0.03
Berea Sandstone	Down	20	16	3556	15			4.88	0.03

Berea Sandstone	Down	20	15	3628	16			4.91	0.03
Berea Sandstone	Down	20	14	3674	16	2154	6	4.94	0.03
Berea Sandstone	Down	20	13	3717	16	2194	6	4.96	0.03
Berea Sandstone	Down	20	12	3750	17	2231	6	4.99	0.03
Berea Sandstone	Down	20	10	3805	18	2285	6	5.03	0.03
Berea Sandstone	Down	20	8	3849	18	2326	6	5.06	0.03
Berea Sandstone	Down	20	6	3880	18	2355	6	5.09	0.03
Berea Sandstone	Down	20	4	3907	18	2382	6	5.12	0.03
Berea Sandstone	Down	20	2	3923	18	2400	6	5.14	0.03
Berea Sandstone	Up	30	2	3993	18	2468	6	5.12	0.03
Berea Sandstone	Up	30	4	3990	18	2463	6	5.12	0.03
Berea Sandstone	Up	30	6	3980	18	2454	6	5.12	0.03
Berea Sandstone	Up	30	8	3970	18	2444	6	5.11	0.03
Berea Sandstone	Up	30	10	3959	18	2434	6	5.10	0.03
Berea Sandstone	Up	30	12	3943	17	2419	6	5.09	0.03
Berea Sandstone	Up	30	14	3930	17	2399	6	5.07	0.03
Berea Sandstone	Up	30	16	3903	17	2378	6	5.05	0.03
Berea Sandstone	Up	30	18	3877	17	2351	6	5.02	0.03
Berea Sandstone	Up	30	20	3842	17	2313	6	5.00	0.03
Berea Sandstone	Up	30	21	3820	17	2293	6	4.98	0.03
Berea Sandstone	Up	30	22	3799	17	2274	6	4.96	0.03
Berea Sandstone	Up	30	23	3762	16	2247	6	4.94	0.03
Berea Sandstone	Up	30	24	3726	16	2194	6	4.92	0.03

Berea Sandstone	Up	30	25	3671	16	2154	6	4.89	0.03
Berea Sandstone	Up	30	26	3620	16			4.85	0.03
Berea Sandstone	Up	30	27	3532	15			4.81	0.03
Berea Sandstone	Up	30	28	3436	15			4.76	0.03
Berea Sandstone	Up	30	29	3268	14			4.52	0.03
Berea Sandstone	Down	30	29	3268	14			4.67	0.03
Berea Sandstone	Down	30	28	3399	14			4.73	0.03
Berea Sandstone	Down	30	27	3500	15			4.78	0.03
Berea Sandstone	Down	30	26	3570	15			4.82	0.03
Berea Sandstone	Down	30	25	3631	16			4.85	0.03
Berea Sandstone	Down	30	23	3729	16	2199	6	4.90	0.03
Berea Sandstone	Down	30	20	3820	17	2286	6	4.97	0.03
Berea Sandstone	Down	30	15	3903	17	2373	6	5.04	0.03
Berea Sandstone	Down	30	10	3953	17	2425	6	5.10	0.03
Berea Sandstone	Down	30	5	3983	18	2455	6	5.15	0.03
Berea Sandstone	Down	30	2	3993	18	2468	6	5.18	0.03
Alumina Ceramic	Down	10	9	3972	17			1.05	.01
Alumina Ceramic	Down	10	8	3981	17			1.07	.01
Alumina Ceramic	Down	10	7	3984	17	2058	5	1.11	.01
Alumina Ceramic	Down	10	6	3984	17	2058	5	1.13	.01
Alumina Ceramic	Down	10	5	3984	17	2058	5	1.14	.01
Alumina Ceramic	Down	10	4	3987	17	2059	5	1.14	.01
Alumina Ceramic	Down	10	3					1.14	.01

Alumina Ceramic	Down	10	2	3987	17	2060	5	1.14	.01
Alumina Ceramic	Down	10	1	3987	17	2058	5	1.14	.01
Alumina Ceramic	Up	10	1	3987	17	2059	5	1.14	.01
Alumina Ceramic	Up	10	2	3987	17	2060	5	1.14	.01
Alumina Ceramic	Up	10	3	3987	17	2060	5	1.14	.01
Alumina Ceramic	Up	10	4	3984	17	2061	5	1.14	.01
Alumina Ceramic	Up	10	5	3987	17	2060	5	1.13	.01
Alumina Ceramic	Up	10	6	3984	17	2058	5	1.13	.01
Alumina Ceramic	Up	10	7	3984	17	2058	5	1.13	.01
Alumina Ceramic	Up	10	8	3984	17			1.10	.01
Alumina Ceramic	Up	10	9	3978	17			1.10	.01
Alumina Ceramic	Down	20	19	3978	17			1.10	.01
Alumina Ceramic	Down	20	18	3981	17			1.10	.01
Alumina Ceramic	Down	20	16	3984	17			1.10	.01
Alumina Ceramic	Down	20	14	3987	17	2060	5	1.10	.01
Alumina Ceramic	Down	20	12	3991	17	2059	5	1.10	.01
Alumina Ceramic	Down	20	10	3991	17	2058	5	1.10	.01
Alumina Ceramic	Down	20	8	3991	17	2058	5	1.10	.01
Alumina Ceramic	Down	20	6	3991	17	2060	5	1.10	.01
Alumina Ceramic	Down	20	4	3991	17	2059	5	1.10	.01
Alumina Ceramic	Down	20	2	3991	17	2061	5	1.10	.01
Alumina Ceramic	Up	20	2	3991	17	2061	5	1.10	.01
Alumina Ceramic	Up	20	4	3991	17	2061	5	1.10	.01

Alumina Ceramic	Up	20	6	3991	17	2061	5	1.10	.01
Alumina Ceramic	Up	20	8	3994	17	2061	5	1.09	.01
Alumina Ceramic	Up	20	10	3991	17	2060	5	1.09	.01
Alumina Ceramic	Up	20	12	3991	17	2059	5	1.09	.01
Alumina Ceramic	Up	20	14	3987	17	2062	5	1.09	.01
Alumina Ceramic	Up	20	16	3987	17	2062	5	1.08	.01
Alumina Ceramic	Up	20	18	3984	17			1.07	.01
Alumina Ceramic	Up	30	2	3994	17	2063	5	1.08	.01
Alumina Ceramic	Up	30	4	3994	17	2062	5	1.07	.01
Alumina Ceramic	Up	30	6	3994	17	2063	5	1.07	.01
Alumina Ceramic	Up	30	8	3994	17	2063	5	1.06	.01
Alumina Ceramic	Up	30	10	3994	17	2061	5	1.06	.01
Alumina Ceramic	Up	30	12	3994	17	2061	5	1.06	.01
Alumina Ceramic	Up	30	14	3994	17	2061	5	1.06	.01
Alumina Ceramic	Up	30	16	3997	17	2061	5	1.05	.01
Alumina Ceramic	Up	30	18	3994	17	2059	5	1.05	.01
Alumina Ceramic	Up	30	20	3994	17	2060	5	1.05	.01
Alumina Ceramic	Up	30	22	3994	17	2060	5	1.05	.01
Alumina Ceramic	Up	30	24	3994	17	2062	5	1.05	.01
Alumina Ceramic	Up	30	26	3991	17	2063	5	1.04	.01
Alumina Ceramic	Up	30	28	3987	17			1.04	.01
Alumina Ceramic	Down	30	25	3991	17	2063	5	1.05	.01
Alumina Ceramic	Down	30	20	3994	17	2060	5	1.05	.01

Alumina Ceramic	Down	30	15	3994	17	2059	5	1.05	.01
Alumina Ceramic	Down	30	10	3994	17	2061	5	1.06	.01
Alumina Ceramic	Down	30	5	3994	17	2063	5	1.06	.01
Alumina Ceramic	Down	30	2	3994	17	2063	5	1.06	.01

Table 2.A2- Dry rock velocities measured for Berea Sandstone and the alumina ceramic

Sample	Confining pressure (MPa)	Vp (m/s)	δV_p (m/s)	Vs (m/s)	δV_s (m/s)
Berea Sandstone	3	3050	14	2000	6
Berea Sandstone	4	3150	14	2060	6
Berea Sandstone	5	3240	14	2120	6
Berea Sandstone	6	3310	15	2160	6
Berea Sandstone	7	3390	15	2200	6
Berea Sandstone	8	3430	15	2240	6
Berea Sandstone	9	3480	16	2260	6
Berea Sandstone	10	3520	16	2290	6
Berea Sandstone	12	3600	16	2340	6
Berea Sandstone	14	3660	17	2390	6
Berea Sandstone	16	3710	17	2420	6
Berea Sandstone	18	3740	17	2450	6
Berea Sandstone	20	3780	17	2480	6
Berea Sandstone	23	3820	17	2510	6
Berea Sandstone	26	3850	18	2530	6

Berea Sandstone	30	3880	18	2560	6
Berea Sandstone	33	3900	18	2570	6
Berea Sandstone	36	3920	18	2580	6
Berea Sandstone	40	3930	18	2600	6
Berea Sandstone	35	3920	18	2590	6
Berea Sandstone	30	3900	18	2570	6
Berea Sandstone	25	3870	18	2550	6
Berea Sandstone	20	3820	18	2520	6
Berea Sandstone	16	3770	17	2480	6
Berea Sandstone	12	3700	17	2430	6
Berea Sandstone	10	3640	17	2390	6
Berea Sandstone	8	3570	16	2340	6
Berea Sandstone	6	3470	15	2270	6
Berea Sandstone	4	3300	15	2160	6
Berea Sandstone	3	3180	14	2080	6
Alumina Ceramic	4	4090	17	2340	5
Alumina Ceramic	5	4120	17	2340	5
Alumina Ceramic	6	4150	17	2340	5
Alumina Ceramic	7	4160	17	2350	5
Alumina Ceramic	8	4170	17	2360	5
Alumina Ceramic	9	4180	17	2360	5
Alumina Ceramic	10	4190	17	2360	5
Alumina Ceramic	12	4200	17	2360	5

Alumina Ceramic	14	4200	17	2370	5
Alumina Ceramic	16	4210	17	2370	5
Alumina Ceramic	18	4210	17	2380	5
Alumina Ceramic	20	4220	17	2380	5
Alumina Ceramic	22	4220	17	2380	5
Alumina Ceramic	24	4220	17	2380	5
Alumina Ceramic	26	4230	17	2380	5
Alumina Ceramic	28	4230	17	2380	5
Alumina Ceramic	30	4230	17	2380	5
Alumina Ceramic	32	4230	17	2380	5
Alumina Ceramic	34	4230	17	2380	5
Alumina Ceramic	36	4240	17	2380	5
Alumina Ceramic	40	4230	17	2380	5
Alumina Ceramic	35	4240	17	2380	5
Alumina Ceramic	30	4240	17	2380	5
Alumina Ceramic	25	4230	17	2380	5
Alumina Ceramic	20	4230	17	2380	5
Alumina Ceramic	15	4230	17	2380	5
Alumina Ceramic	10	4220	17	2380	5
Alumina Ceramic	5	4190	17	2370	5

2.9) References

Adams, L. H., and E. D. Williamson. (1923). Compressibility of minerals and rocks at high pressures. *Journal of the Franklin Institute* 195: 475-529.

Aquino-Lopez, A., A. Mousatov, and M. Markov. (2011). Model of sand formations for joint simulation of elastic moduli and electrical conductivity. *Journal of Geophysics and Engineering* 8 (4): 568-578.

Archie, G. E. (1942). The electrical resistivity log as an aid in determining some reservoir characteristics. *Transactions of the American Institute of Mining and Metallurgical Engineers* 146: 54-62.

Asami, K. (2002). Asami, K. (2002). "Characterization of heterogeneous systems by dielectric spectroscopy. *Progress in Polymer Science* 27 (8): 1617-1659.

Avellaneda, M., and S. Torquato. (1991). Rigorous link between fluid permeability, electrical conductivity, and relaxation times for transport in porous media. *Physics of Fluids A* 3: 2529-2540.

Bachrach, Ran. (2011). Elastic and resistivity anisotropy of shale during compaction and diagenesis : Joint effective medium modeling and field observations. *Geophysics* 76 (6): E175-E186.

Batzle, M., and Z. Wang. (1992). Seismic properties of pore fluids. *Geophysics* 57 (11): 1396-1408.

Bernabe, Y. (1991). Pore Geometry and pressure-dependence of the transport-properties in sandstones. *Geophysics* 56 (4): 436-446.

Brace, W F, and A S Orange. (1968). Further Studies of the Effects of Pressure on Electrical Resistivity of Rocks. *Journal of Geophysical Research* 73 (16): 5407-5420.

Brace, W. F., A. S. Orange, and T. R. Madden. (1965). Effect of pressure on electrical resistivity of water-saturated crystalline rocks. *Journal of Geophysical Research* 70 (22): 5669-5678.

Brown, V., K. Key, and S. Singh. (2012). Seismically regularized controlled-source electromagnetic inversion. *Geophysics* 77 (1): 1JF-Z19.

Burns, D. R., C. H. Cheng, and R. H. Wilkins. (1990). Sandstone Pore Aspect Ratio Spectra from Direct Observations and Velocity Inversion. *International Journal of Rock Mechanics and Mining Sciences & Geomechanics Abstracts* 27 (4): 315-323.

Bussian, A. (1983). Electrical conductance in a porous medium. *Geophysics* 48 (9): 1258-1268.

Carcione, Jose, Bjorn Ursin, and Janniche Nordskeg (2007). Cross-property relations between electrical conductivity and the seismic velocity of rocks. *Geophysics* 72 (5): E193-E204.

Carlson, R. L., and A. F. Gangi (1985). Effect of cracks on the pressure-dependence of P-wave velocities in crystalline rocks. *Journal of Geophysical Research-Solid Earth and Planets* 90 (NB10): 8675-8684.

Chapman, M. (2003). Frequency-dependent anisotropy due to meso-scale fractures in the presence of equant porosity. *Geophysical Prospecting* 51 (5): 369-379.

Chelidze, T L, and Y. Gueguen (1999). Electrical spectroscopy of porous rocks: a review -I Theoretical models. *Geophysical Journal International* 137: 1-15.

Cheng, C. H., and M. N. Toksoz (1979). Inversion of seismic velocities for the pore aspect ratio spectrum OF a rock. *Journal of Geophysical Research* 84 (NB13): 7533-7543.

David, E. C., and R. W. Zimmerman (2012). Pore structure model for elastic wave velocities in fluid-saturated sandstones. *Journal of Geophysical Research-Solid Earth* 117: B07210.

Doyen, P. M. (1987). Crack geometry in igneous rocks - a maximum-entropy inversion of elastic and transport-properties. *Journal of Geophysical Research-Solid Earth and Planets* 92 (B8): 8169-8181.

Durr, O., W. Dieterich, P. Maass, and A. Nitzan (2002). Effective Medium Theory of Conduction in Stretched Polymer Electrolytes. *Journal of Physical Chemistry B* 106: 6149-6155.

Fatt, I., and D. H. Davis (1952). Reduction in permeability with overburden pressure. *Transactions of the American Institute of Mining and Metallurgical Engineers* 195: 329-329.

Gangi, A. F (1978). Variation of whole and fractured porous rock permeability with confining pressure. *International Journal of Rock Mechanics and Mining Sciences & Geomechanics Abstracts* 15 (5): 249-257.

Gangi, Anthony, and Richard Carlson (1996). An asperity deformation model for effective pressure. *Tectonophysics* 256: 241-251.

Gao, K., and R. L. Gibson Jr. (2012). Pressure-dependent seismic velocities based on effective compliance theory and an asperity deformation model. *Geophysics* 77 (6): D229-D243.

Gassmann, F. (1951). Elastic Waves through packing of spheres. *Geophysics* 16 (4).

Glover, P. W.J., and F. J. Vine (1995). Beyond KTB - electrical conductivity of the deep continental crust. *Surveys in Geophysics* 16 (1): 5-36.

Glubokovskikh, S., B. Gurevich, M. Lebedev, V. Mikhaltsevitch, and S. Tan (2016). Effect of asperities on stress dependency of elastic properties of cracked rocks. *International Journal of Engineering Science* 98: 116-125.

Gomez, C. T., J. Dvorkin, and T. Vanorio (2010). Laboratory measurements of porosity , permeability , resistivity , and velocity on Fontainebleau sandstones. *Geophysics* 75 (6): E191-E204.

Greenwood, J. A., and J. B. Williamson (1966). Contact of nominally flat surfaces. *Proceedings of the Royal Society of London Series a-Mathematical and Physical Sciences* (295): 300-310.

Han, T. C. (2018). An effective medium approach to modelling the pressure-dependent electrical properties of porous rocks. *Geophysical Journal International* 214 (1): 70-78.

Han, T. C. (2016). Are self-consistent models capable of jointly modeling elastic velocity and electrical conductivity of reservoir sandstones? *Geophysics* 81 (4): D377-D382.

Han, T. C. (2018). Joint Elastic-Electrical Properties of Artificial Porous Sandstone With Aligned Fractures. *Geophysical Research Letters* 45 (7): 3051-3058.

Han, T.C., A. Best, J. Sothcott, and L. Macgregor. 2011. Joint elastic-electrical properties of reservoir sandstones and their relationships with petrophysical parameters. *Geophysical Prospecting* 59: 518-535.

Hashin, Z. (1988). The differential scheme and its application to cracked materials. *Journal of Mechanics and Physics of Solids* 36: 719-734.

Izumotani, S., and S. Onozuka (2013). Elastic moduli and the aspect ratio spectrum of rock using simulated annealing. *Geophysical Prospecting* 61: 489-504.

Jensen, E. H., L. J. Gelius, T. A. Johansen, and Z. Wang (2013). Consistent joint elastic-electrical differential effective-medium modelling of compacting reservoir sandstones. *Geophysical Prospecting* 61 (4): 788-802.

Kachanov, Mark (1992). Effective elastic properties of cracked solids: critical review of some basic concepts. *Applied Mechanics Reviews* 45 (8): 304:335.

Kazatchenko, E., M. Markov, A. Mousatov, and J. O. Parra (2006). Carbonate microstructure determination by inversion of acoustic and electrical data: Application to a south Florida aquifer. *Journal of Applied Geophysics* 59 (1): 1-15.

Kozlov, E. (2004). Pressure-dependent seismic response of fractured rock. *Geophysics* 69 (4): 885-897.

MacBeth, C., J. Stammeijer, and M. Omerod (2006). Seismic monitoring of pressure depletion evaluated for a United Kingdom continental-shelf gas reservoir. *Geophysical Prospecting* 54 (1): 29-47.

Marquis, G., and R. D. Hyndman (1992). Geophysical support for aqueous fluids in the deep crust: seismic and electrical relationships. *Geophysical Journal International* 110 (1): 91-105.

Mavko, G. M., and A. Nur (1978). Effect of non-elliptical cracks on compressibility of rocks. *Journal of Geophysical Research* 83 (NB9): 4459-4468.

Moorkamp, M., A. G. Jones, and S. Fishwick (2010). Joint inversion of receiver functions, surface wave dispersion, and. *Journal of Geophysical Research* 115: B04318.

Prasad, M., and M. Manghnani (1997). Effects of pore and differential pressure on compressional wave velocity and quality factor in Berea and Michigan sandstones. *Geophysics* 62 (4): 1163-1176.

Pride, S. R., J. G. Berryman, M. Commer, S. Nakagawa, G. A. Newman, and D. W. Vasco (2017). Changes in geophysical properties caused by fluid injection into porous rocks: analytical models. *Geophysical Prospecting* 65 (3): 766-790.

Revil, A., and L. Cathles (1999). Permeability of shaly sands. *Water Resources Research* 35 (3): 651-662.

Saeger, E H, and S A Shapiro (2002). Effective velocities in fractured media: a numerical study using rotated staggered finite-difference grid. *Geophysical Prospecting* 50: 183-194.

Sayers, Colin M, and Mark Kachanov (1995). Microcrack-induced elastic wave anisotropy of brittle rocks. *Journal of Geophysical Research* 100 (B3): 4149-4156.

Schmitt, D. R. 2015. Geophysical Properties of the Near Surface Earth: Seismic Properties. Edited by G. Schubert. *Treatise in Geophysics (2nd edition)* (Elsiver) 11 (2): 43-87.

Sen, P., C. Scala, and M. Cohen (1981). A self-similar model for sedimentary rocks with application to the dielectric constant of fused glass beads. *Geophysics* 46 (5): 781-795.

Stesky, R M. (1985). Compressional and shear velocities of dry and saturated jointed rock: a laboratory study. *Geophysical Journal of the Royal astronomical Society* 83: 239-262.

Stesky, R M. (1986). Electrical conductivity of brine-saturated fractured rock. *Geophysics* 51 (8): 1585-1593.

Stesky, R. M., and S. S. Hannan (1989). A new theory for the static contact between rough, unmated surfaces in non-elastically deforming rock and its implications for rock friction. *Journal of Structural Geology* 11 (7): 787-798.

Sumner, J S. (1976). *Principles of induced polarization for geophysical exploration.* Elsiver.

Walsh, J B. (1981). Effect of pore pressure and confining pressure on fracture permeability. *International Journal of Rock Mechanics and Mining Sciences and Geomechanics Abstracts* 18: 429-435.

Walsh, J. B., and M. A. Grosenbaugh (1979). New model for analysing the effect of fractures on compressibility. *Journal of Geophysical Research* 84 (NB7): 3532-3536.

Wang, Z., and L. J. Gelius (2010). Electric and elastic properties of rock samples: a unified measurement approach. *Petroleum Geoscience* 16 (2): 171-183.

Wang, Zhong, Leiv Gelius, and Fan-Nian Kong (2009). Simultaneous core sample measurements of elastic properties and resistivity at reservoir conditions employing a modified triaxial cell- a feasibility study. *Geophysical Prospecting* 57: 1009-1026.

Weller, A., L. Slater, and S. Nordsiek (2013). On the relationship between induced polarization and surface conductivity: Implications for petrophysical interpretation of electrical measurements. *Geophysics* 78 (5): D315-D325.

Wong, T. F., J. T. Fredrich, and G. D. Gwanmesia (1989). Crack aperture statistics and pore space fractal geometry of westerly granite and rutland quartzite: Implications for an elastic contact model of rock compressibility. *Journal of Geophysical Research Solid Earth* 94 (B8): 10267-10278.

Wyllie, M. R.J., A. R. Gregory, and L. W. Gardner (1956). Elastic wave velocities in heterogenious and porous media. *Geophysics* 21 (1): 41-70.

Yam, H. (2011). *CO2 rock physics: A laboratory Study.* MSc Thesis, Edmonton: Department of Physics, University of Alberta.

Yan, P., T. Kalscheuer, P. Heidin, and M. A.G. Juanatey (2017). Two-dimensional magnetotelluric inversion using reflection seismic data as constraints and application in the COSC project. *Geophysical Research letters* 44 (8): 3554-3563.

Zaitsev, V. Y., A. V. Radostin, E. Pasternak, and A. Dyskin (2017). "Extracting shear and normal compliances of crack-like defects from pressure dependences of elastic-wave velocities." *International Journal of Rock Mechanics and Mining Sciences* 97: 122-133.

Zhang, L., J. Ba, L. Fu, J. M. Carcione, and C. Cao (2019). Estimation of pore microstructure by using the static and dynamic moduli. *International Journal of Rock Mechanics and Mining Sciences* 113: 24-30.

Chapter 3

Preliminary experiments towards understanding the influence of fractures on the anisotropy of electrical conductivity

3.1) Introduction

Anisotropy can be defined as the property of being directionally dependent so that the same physical property may have different values for the same material if the measurement direction is varied. It has long been recognized that the flow of current through the subsurface varies with direction of the applied voltage and that this anisotropy is controlled by geologic structure. Indeed, Schlumberger et al. (1934) note from field observations that the resistivities perpendicular to geoelectric strike regularly exceed those parallel by 2 to 40 times. They suggested that current flowed more easily through water-filled fractures that, too, more naturally ran parallel to the geoelectric strike. Curiously, despite this early recognition of the severity of electrical anisotropy, workers still commonly assume that the subsurface materials are electrically isotropic.

Understanding the electrical conductivity anisotropy of a rock mass is complicated by the multiple mechanisms of electrical conduction that can act in porous media. Charges can move through many parallel paths along the mineral surfaces, within the bulk of the electrolyte in the pore space, through the mineral solids, and across geologic structures at differing dimensional scales. Any of these paths may have preferential directions that would make the bulk conductivity anisotropic. This anisotropy can significantly influence the processing and interpretation of geophysical electrical surveys (e.g., Ellis et al, 2010; Leibecker et al, 2002; Marti, 2014; Brown et al, 2012; Newman et al, 2010) and is a concern for the interpretation of various electrical logging techniques

(see Anderson et al. (1994) for a review) but although anisotropy has been found in the field, the source of this electrical anisotropy is rarely investigated in any detail.

That said, there are some works dedicated to measuring electrical anisotropy in rock samples. Hill (1972) measured the anisotropy of electrical conductivity and dielectric constants from 10 Hz to 100 kHz on dry and highly resistive crystalline Precambrian Shield rocks. Louis et al., (2003) determined acoustic, magnetic, and electrical anisotropy using three orthogonally cut core samples from each of two different sandstones. Zisser and Nover (2009) carried out an extensive study comparing the pressure dependences of permeability and complex electrical conductivity anisotropies on tight sandstones to confining pressures of 100 MPa. North et al. (2013) introduced a laboratory procedure for determining the resistivity tensor for a material that North and Best (2014) then used to measure the resistivity tensor of clean reservoir sandstones finding anisotropy ratios between 1.15 and 1.25. Woodruff et al., (2014) and Woodruff et al., (2015) determine the conductivity tensor on a variety of shales. David et al. (2017) describe a system that allows a simplified electrical resistivity tensor to be derived from multiple radial measurements on orthogonally-oriented sample cylinders cored from the same rock block.

This, taken with the fact that electrical anisotropy plays a large role in processing CSEM and magnetotelluric data, highlights the need to better understand different causes of anisotropy and their relative influence on electrical measurements. For instance, it is plausible to suggest that the electrical anisotropy of a given formation may change after that formation has been hydraulically fractured with the induced fractures expected to align in the direction of the maximum horizontal stress, and this is often used to predict the direction that most fluid will flow. The flow of both fluids and current (at low frequencies) make use of the same connected pathways; and inferences about permeability can sometimes be interchangeably applied to resistivity. Understanding how

the anisotropy introduced by fractures interacts with the background anisotropy of the pore space is therefore relevant to accurate electrical imaging of the reservoir. This is in addition to modeling the behaviour of fluids injected into the ground. This is relevant to both the oil and gas, and geothermal industries.

An additional complication to the problem is the role that surface conduction plays in the anisotropic response. Anisotropic surface conduction gives information about the mineral orientation (Robion et al., 2012) which reflects the loading and tectonic history and is not necessarily obvious from the present tectonic setting. However, pore space directional orientation is partly reflected by compaction which controls mineral orientation and so these two are closely related. It is desirable to separate anisotropy due to surface conduction and that due to pore space anisotropy if they are different. Woodruff et al. (2014) partly did this by using a combination of high and low salinity measurements on samples that were likely to have high surface conductivity with an obvious preferred orientation. The ratio between the resistivities measured perpendicular and parallel to bedding decreased with more saline electrolytes. This suggests that anisotropy due to mineral alignment will be stronger than that due to preferred pore space orientation (depending on the mineralogy).

Workers (e.g., Revil et al., 2013) often assume that the principal directions of the conductivity tensor align with the bedding planes in sediments. Introduction of a variously oriented fracture to this matrix, however, may disrupt the primary current flow directions. Further, although measurement techniques like that shown by North et al. (2013) are capable of separating surface conductivity tensor from the pore space conductivity tensor if used at multiple salinities, it is difficult to know exactly how much fractures affect the background rock without knowledge of its "uncracked" conductivity tensor. Although it has been shown that fractures significantly channel

current in an isotropic background medium (Tranter et al., 2018), it is not understood how much this can affect conductivity in relatively porous, permeable rocks where other conductive pathways exist.

In this chapter, a series of electrical conductivity measurements on an artificial porous material containing oriented cracks are presented. The background matrix is constructed from glass beads and epoxy. Using synthetic samples allows us to 1) verify that the background material is isotropic and 2) control the orientation of cracks. The samples showed relatively small anisotropic ratios (1.01-1.11) but showed a clear trend with the ratio of crack porosity to total porosity. It is important to note that Han et al, (2018, 2019) have also recently carried out electrical conductivity and dielectric constant anisotropy measurements on synthetic sandstones containing known oriented flaws. The synthetic sandstone samples here differ significantly in that they contain only a single large fracture within the otherwise porous medium. This information can help in modeling the effects of fractures on a previously unfractured reservoir. Preferentially aligned fractures are often expected in the earth. Joint sets, for example, are often strongly oriented. Stress fields, too, tend to preferentially open or close different fractures sets in the earth as is often manifest as seismic anisotropy.

The primary contribution here is the development of a novel experimental configuration to make measurements on artificial rock samples containing oriented fractures. The paper includes a detailed description of the experimental method starting with the manufacture of artificial anisotropic samples with controlled crack porosity and followed by an account of the experimental procedures used to measure the electrical anisotropy. The paper concludes with discussion of the results and their impact rock physics modeling. Before continuing a small note on terminology is necessary. In Chapter 2 a distinction was drawn between the appropriate use of the terms crack

and fracture. Here, the defects are fractures but the term crack porosity is still used to describe nominally flat porosity.

3.2) Theory

In the following we consider conduction in porous media where conduction takes place only through the pore space. We therefore ignore surface conductivity effects.

Ohm's law relates the electric field, E (in V/m) to the current density J (in A/m^2) as

$$J_i = \sigma_{ij} E_j \tag{3.1}$$

where σ_{ij} is the conductivity, more commonly referred to by its inverse resistivity ($\rho = \frac{1}{\sigma}$) in geophysical literature and i and j are directional indices. In the lab σ is determined by obtaining the apparent material resistance R (in Ω) from voltage V (in V) and current, I (in A) measurements

$$R = \frac{V}{I} \tag{3.2}$$

This can be converted to resistivity or conductivity through a geometric parameter G such that

$$\rho = RG \tag{3.3}$$

When measurements are made in the axial direction on samples of length L with a constant cross-sectional area A, the geometric factor G is simply the familiar A/L. Here the measurements are made radially across a cylindrical sample and determination of G is more complicated as the geometries of the opposing curved electrodes must be considered. For the right-cylindrical geometry used here, Wang et al. (2009) numerically solved for G arriving at an expression:

$$G = \eta dL \tag{3.4}$$

where *d* and *L* are the diameter and length (in m) and $\eta = 25.73$ is a correction factor that applies to a geometry in which the electrodes are 30 mm wide extending the length of a cylindrical sample with 38 mm diameter.

The conductivity of the rock is given in the form of 2nd-order tensor components:

$$\sigma_{ij} = \sigma_w(\frac{1}{F})_{ij} \quad (3.5),$$

where σ_w is the conductivity of the electrolyte fully saturating the pore space and $(\frac{1}{F})_{ij}$is the inverse formation factor given in Archie's (1942) law as

$$\frac{1}{F} = \varphi^m \quad (3.6)$$

where φ is the connected porosity and m is the cementation exponent. Revil and Cathles (1999) show that the inverse formation factor is related to that portion of the porosity connected by lines of flux with higher weight given to cracks and narrow pore throats where electric field lines are denser. In this way, the cementation exponent *m* acts in decoupling the porosity not involved in conduction from that which is.

Wyllie and Rose (1950) derived an expression for the formation factor of capillary tubes in terms of porosity as

$$\frac{\sigma_r}{\sigma_w} = \frac{1}{F} = \frac{\varphi}{\tau} \quad (3.7)$$

where σ_r is the whole rock conductivity and τ is the average tortuosity of flow paths in the rock given as:

$$\tau = \frac{L_e}{L} \quad (3.8)$$

where L_e is the effective path length illustrated in Fig. 3.1 and L is the straight-line distance from the beginning to the end of the path. Porosity in Eqn. 3.7 is a scalar but tortuosity is often expressed as the connectivity tensor T (e.g., Revil et al, 2013), the components of which are the inverse of the tortuosity factor in that direction so that:

$$(\frac{1}{F})_{ij} = \varphi T_{ij} \tag{3.9}$$

The capillary tube model does not account for the branching nature of porosity or for dead end pores but is useful as a link between electrical measurements and fluid flow modeling. (Johnson et al, 1986). Nominally flat cracks do not cause a change in tortuosity in flow paths oriented perpendicular to them. So tortuosity values in the perpendicular direction can be seen as equivalent to the "uncracked" isotropic tortuosity.

Conductivity models for anisotropic porous media have been developed by Mendelson and Cohen (1982) who extended the work of Sen et al. (1981) solving for the effective properties of composite dielectrics. They show that Archie's law can be derived from this approach and that the cementation exponent is a shape parameter for inclusions. DEM has the benefit of being able to model conductivity for the entirety of the frequency spectrum but does not offer the same analogy to transport problems due to the different mechanisms for conduction at high frequencies.

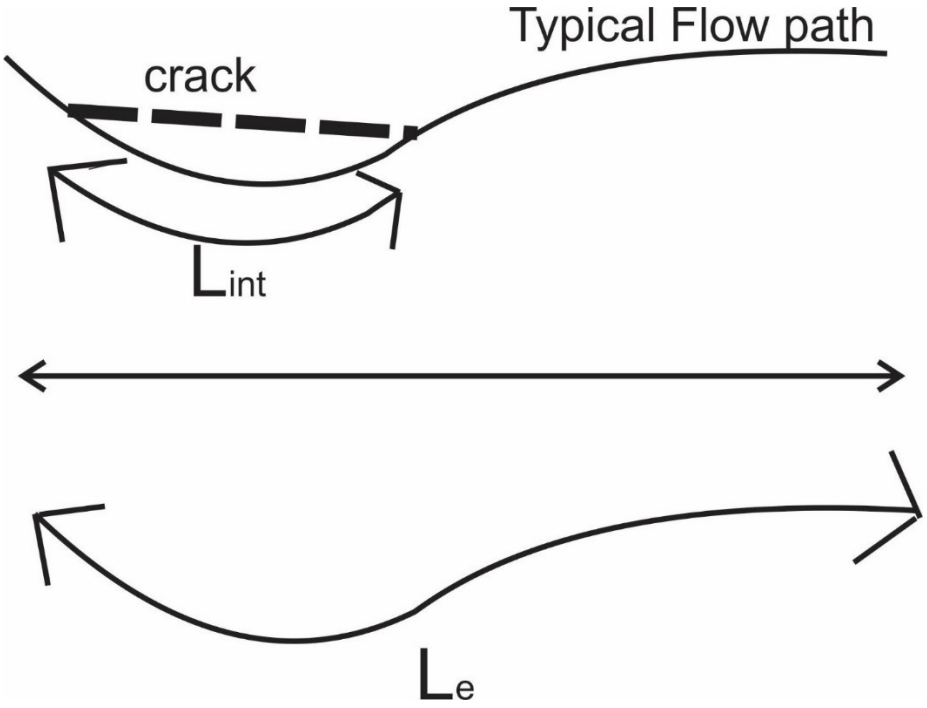

Figure 3.1. Illustration of the effect of cracks on flow paths Le shows the usual path current would have to travel and L_{int} shows the length of that path that is short circuited by the crack.

3.3) Experimental method

Artificial porous samples with macroscopic embedded "cracks" were constructed to study their effect on electrical anisotropy. The manufacture of these samples and a radial-strap electrode array developed to measure their conductivity are reviewed.

3.3.1) Synthetic samples

Sample geometry is often problematic in electrical measurements, and this sometimes requires that complicated geometric correction factors be determined to obtain true material resistivities from the apparent values found that might be found by simply taking the ratio of measured voltage *V* to input current *I*. This is particularly important when attempting to measure electrical anisotropy, and numerous geometries have been proposed to accomplish this (e.g., see Walmsley and Fisher,

2017). In order to reduce these complications and to simplify the problem to a more tractable 2D situation, a cylindrical shape containing "cracks" fully extending along the axis was adopted. Han et al. (2018) adapted a similar geometry but with octagonal cross-sectional shape to carry out their measurements.

To simplify the analysis, measurements are made only parallel and perpendicular to the plane of the fractures with the implicit assumption that the current flux lines also run completely in parallel and perpendicular directions. Two-dimensional finite element simulations, similar to those of Wang et al., (2009) and Abousrafa et al., (2013) were carried out in order to verify the current paths. The calculations were conducted on a circular cross-section of the cylinder using Matlab's™ PDE tool box. The relationship between current density and electric field is specified by Ohm's law (Eqn. 3.1) and the pde tool solves Poisson's equation:

$$-\nabla \cdot (\sigma \nabla V) = Q \tag{3.10}$$

where σ gives the conductivity of the material inside the circle, ∇V gives the gradient of voltage and Q specifies a current source in the figure, but Q = 0 for this simulation. The material is set to be homogeneous and isotropic.

Fig. 3.2 shows the result of a circle with electrodes that are in contact with 30 mm along the circumference of the sample at two opposite sides. Dirichlet boundary conditions are applied at the electrodes with the potentials set to 2V and -2V. Elsewhere a Neumann boundary condition is used meaning that current cannot flow normal to boundaries other than at the electrodes (i.e. $\boldsymbol{J} \cdot \boldsymbol{n}$ = 0, where J is the current density and n is the normal vector to the surface). A crack is annotated in black perpendicular to the electric field. The conductivity is set to 2 S/m and a voltage difference of 4V is applied. The applied voltage is DC unlike the actual measurement current. The colour

shows electric field values and contours denote lines of equipotential. Arrows indicate current density direction. The direction of the current density vectors relative to the annotated crack shows that for the size of the electrodes used here, the current lines at the location of the crack will be perpendicular or parallel to the fracture for the two measurement directions.

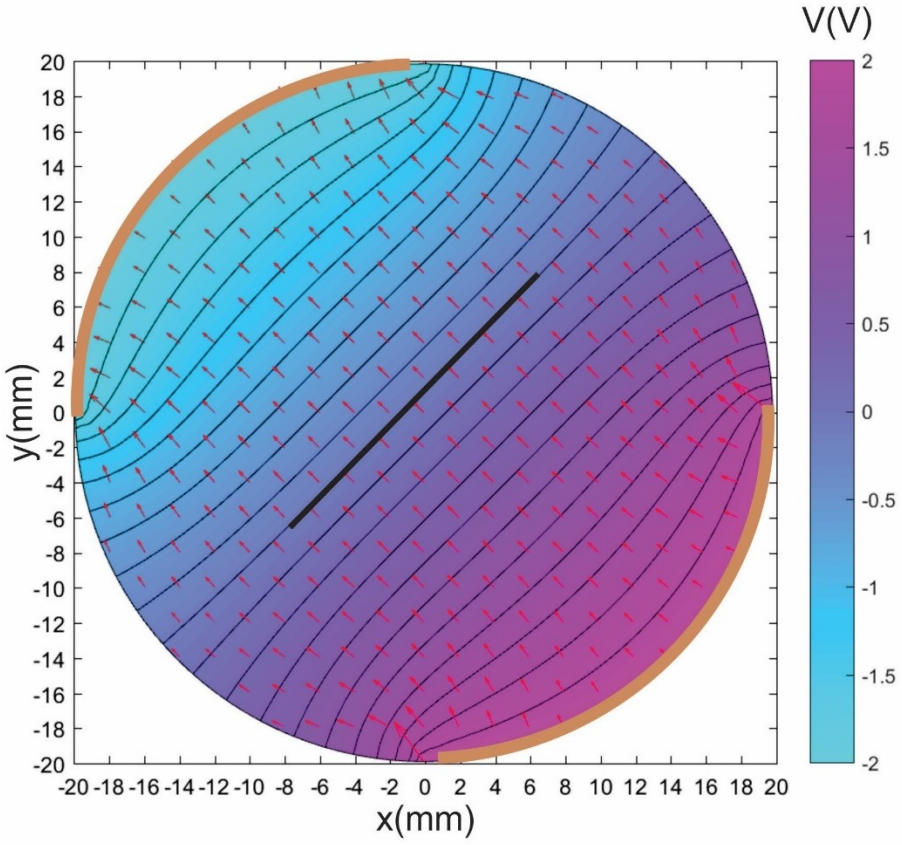

Figure 3.2. Result of simulation on a circular cross-section with colour bar indicating Electric potential. Electrodes are shown in brown with red arrows indicating the direction of current density vectors.

The samples were constructed from a mixture of glass beads (Manus Abrasives, 44-88 μm diameters) cemented with a slow curing epoxy (West Systems) following procedures similar to Rathore et al. (1995) and Wang et al. (2017). An advantage of using epoxy is that it is weakly hydrophobic meaning that the role of surface conductivity along the glass beads is reduced.

Specific bead/epoxy mixing ratios were used to obtain differing porosities with ratios of about 8:1 to 7:1 found to give the best balance of porosity relative to material strength. The mix was loaded into a cylindrical mould of machined aluminum that could later be split along the axis of the cylinder, and then compacted by shaking and pressing with a plunger. The interior diameter of the cylindrical mould was 3.81 cm (1.5") but the sample lengths varied from about 3.0 to 3.8 cm (Table 3.1). Once the mix was appropriately compacted, an incision was made into the mixture using a flat steel ruler to make space for a water-soluble polysaccharide polymer (pullulan) strip (Listerine Pocketpacket™) that formed the inverse mold for the future fracture. Use of the water-soluble strips avoided the precipitation of salts in the pore space produced in our first attempts at making internal fractures using aluminum strips leached with caustic NaOH (e.g., Wang et al., 2017). For comparison, Han et al., (2018) used plastic pieces to create their penny shaped inclusions that were removed from the matrix by heating to 900°C. The water-soluble strips were cut sufficiently long to allow them to extend the full sample length. Each strip was 0.060 mm thick and 22.0 mm wide; in order to make thicker fractures the strips were stacked on top of one another before being embedded in the sample. However, it is important to note that two of the samples had multiple cracks inserted separately. The number of strips used was consistent from sample to sample ensuring that they all had similar crack porosities but allowing for the flexibility of distributing the flaws differently in some samples (Fig. 3.3). Once the strips were inserted the mix was again compacted and left to harden overnight. The samples were then removed from the mould and further cured in an oven at 65 ◦C overnight. De-ionized water was then percolated through the samples to dissolve the strips for 24 hours. Finally, the samples were again oven dried. Cleaving open some of the samples after the measurements verified that the strips were completely dissolved leaving behind the inverse mould crack (Fig. 3.5).

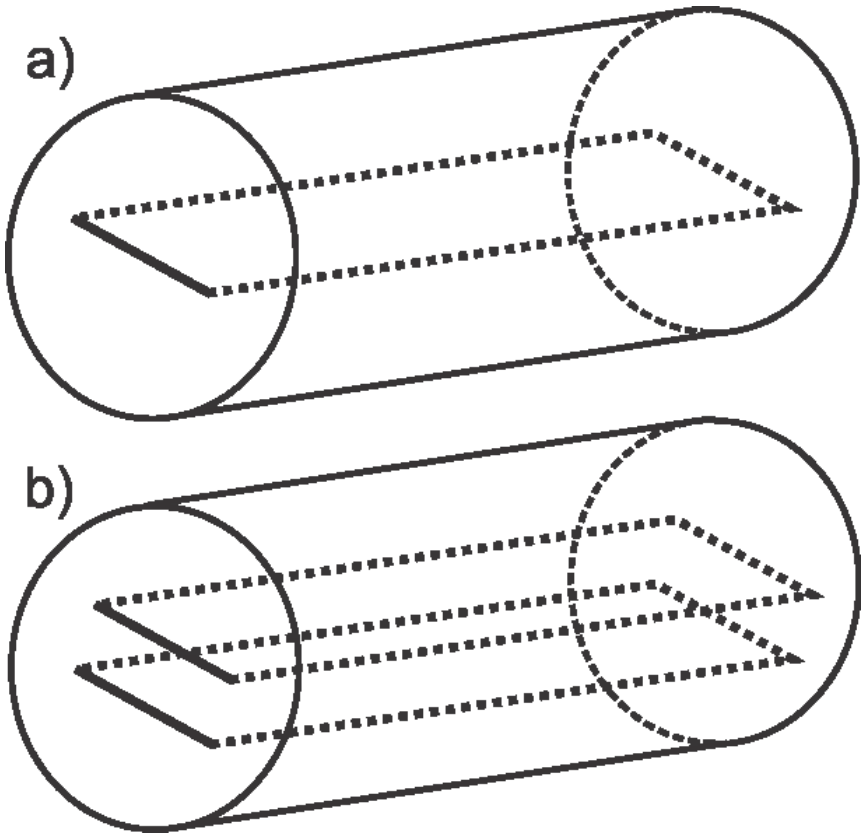

Figure 3.3. Simplified sample geometry containing a) single crack, and b) two separated cracks.

One concern for the analysis of the results is the degree to which surface conduction along the internal surfaces of the sample might contribute to the overall bulk conductivity of the sample. It should be noted that the use of epoxy is particularly useful here since it is non-wetting with deionized water (Wang et al 2015), and this suggests too that it is difficult to develop electrical diffuse layers near the bead surfaces. In order to satisfy the requirement that surface conductivity not be important, the resistivity of a subset of the samples was measured using electrolytes with differing salinities (i.e., giving differing σ_w). The formation factor did not change with σ_w

indicating that surface conductivity was not important and that that the conductivity could be attributed to electrolytic current.

For all the tests, the samples were saturated with a 1% NaCl by weight electrolyte made by dissolving reagent grade NaCl in distilled water; this is expected to give a nominal σ_w = 1.76 S/m at room temperature as was confirmed by measuring the fluid conductivity independently using a 4-electrode configuration. Samples were saturated under vacuum overnight.

The sample geometries and petrophysical characteristics are summarized in Table 3.1 and Fig.3.4 shows a picture of an intact sample next to a cleaved one.

The total porosity φ was determined by measuring the actual grain and bulk density of the samples prior to the electrical measurements. The grain density was measured using a Boyle's law Helium pycnometer (Quantachrome Instruments™). The bulk density was determined by Archimedes' method. This involved weighing the sample in air and then recording its weight when immersed in water. To account for any invasion of water when it was fully immersed, we weigh the sample after and subtract the weight of any water that had invaded the pore space. The bulk density can be determined by Eqn. 3.6 as:

$$\rho_b = \frac{mass\ in\ air}{mass\ in\ air - mass\ in\ water} \times \rho_f \tag{3.6}$$

where ρ_b is the bulk density and ρ_f is the density of the fluid. The porosity can then be determined by Eqn. 3.7:

$$\varphi = \frac{\rho_g - \rho_b}{\rho_g - \rho_a} \tag{3.7}$$

where ρ_g is the grain density and ρ_a is the density of air.

The crack porosity φ_c is simply the ratio of the known volume of the pullulan strips inserted to the sample to the sample's total volume.

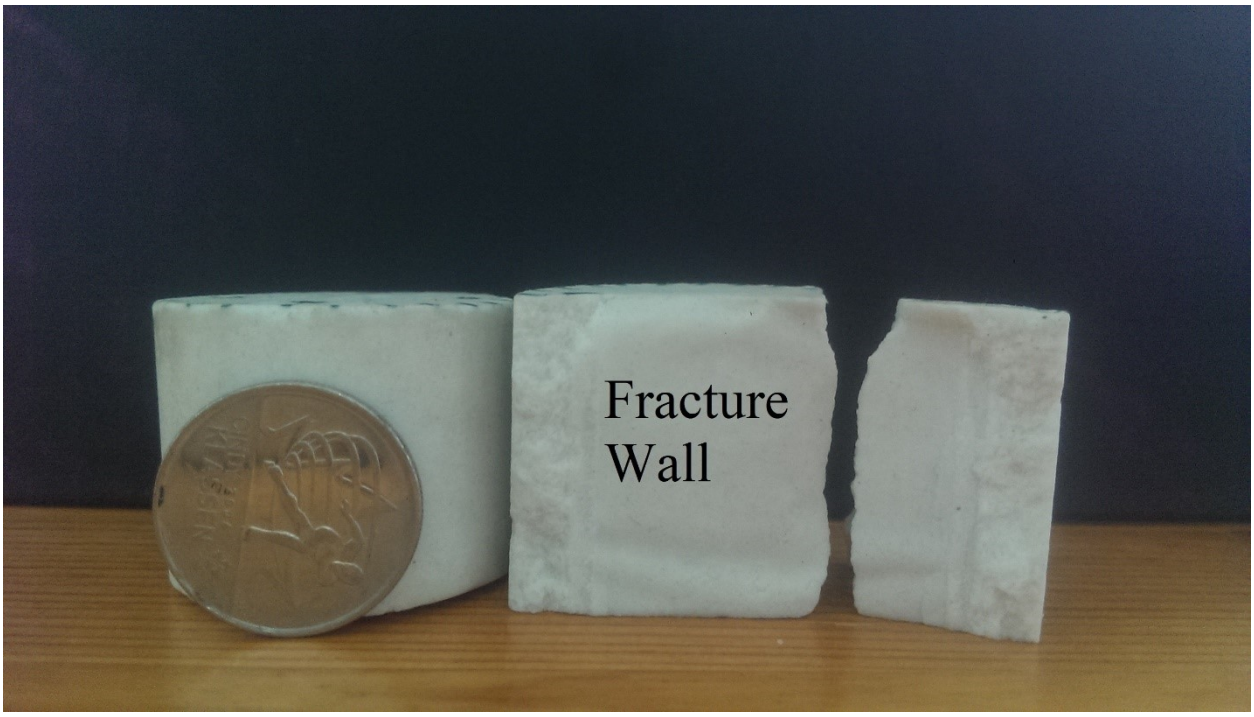

Figure 3.4. Photograph of a broken and cleaved sample showing clear fracture surface alongside an intact sample. Canadian quarter with 23.81 mm diameter for scale.

Table 3.1. Geometries of the constructed samples

Sample ID	Ratio of glass beads to epoxy	number of stacked strips	Total Porosity (ϕ)	Crack Distribution	Crack Aperture mm	Crack Porosity (φ_c)	Sample length (cm)
A1	8:1	1	0.2475	single	0.06	0.0012	3.022
A2	8:1	2	0.2491	single	0.12	0.0022	3.47
A3	8:1	3	0.258	single	0.18	0.0035	3.187
A4	8:1	4	0.2633	single	0.24	0.0044	3.523
A5	8:1	5	0.2562	single	0.30	0.0052	3.723
A6	8:1	2	0.2631	separated	0.06 x 2	0.0022	3.437
A7	8:1	3	0.2591	separated	0.06 x 3	0.0035	3.111
B1	8:1	0	0.2721	N/A	N/A	0	6.335
B2	8:1	0	0.2619	N/A	N/A	0	5.851
B3	8:1	0	0.2669	N/A	N/A	0	6.365
B4	8:1	0	0.2553	N/A	N/A	0	5.907
A8	7:1	1	0.2061	single	0.06	0.0012	3.296
A9	7:1	2	0.206	single	0.12	0.0023	3.126
A10	7:1	3	0.2086	single	0.18	0.0035	3.251
A11	7:1	4	0.2039	single	0.24	0.0046	3.204
A12	7:1	5	0.2106	single	0.30	0.0058	3.255
B5	7:1	0	0.2289	N/A	N/A	0	3.455
B6	9:1	0	0.2665	N/A	N/A	0	6.793
B7	9:1	0	0.2769	N/A	N/A	0	5.901
B8	10:1	0	0.2908	N/A	N/A	0	6.055

It is useful to further examine the mixing ratio as a function of porosity (Fig. 3.5). Although the mixing ratio exercises some control over the porosity, it does allow for some variation for a given mixing ratio. The comparison suggests that construction of a relatively uniform porous matrix is relatively repeatable, but with some variation in porosity. This may be due to the precision of the scale used to measure out the ratios. Variations on the order of 0.1 g could cause differences observed between supposedly identical samples. Alternatively, it may be due to inconsistency in grain size distribution (manufacturer error) of the samples or differences between how the spheres

packed together for different samples although care was taken so that the sample construction process was identical from one sample to another. Some combination of all three of these may also be responsible.

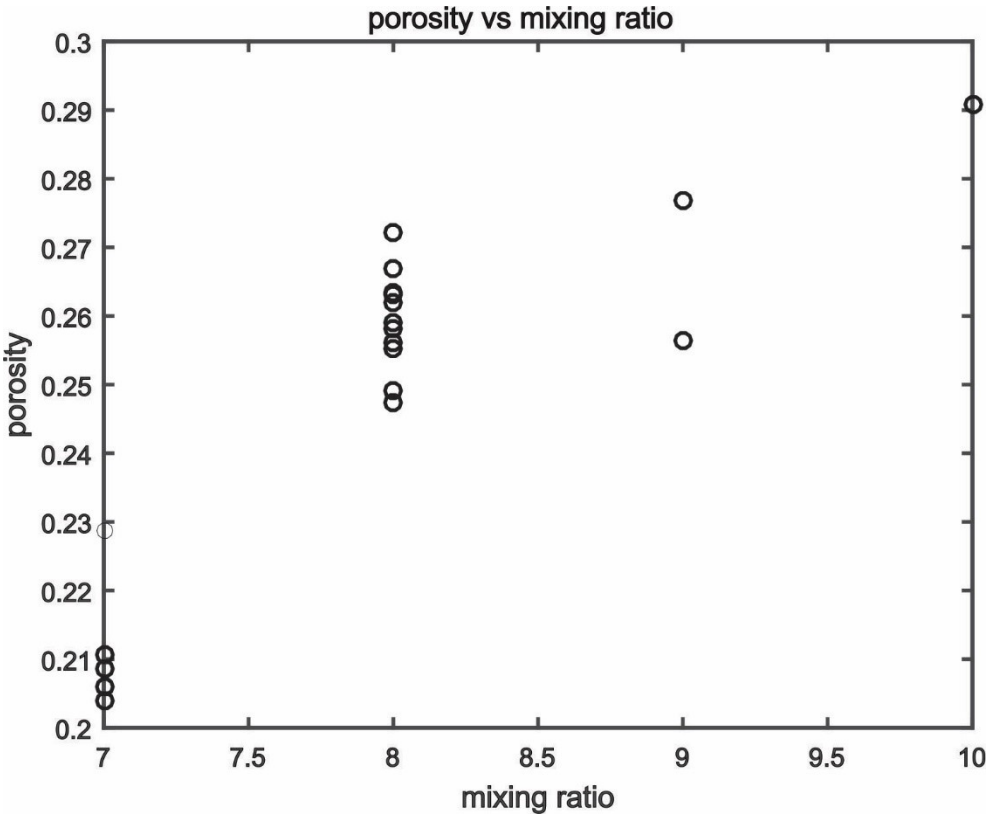

Figure 3.5. Sample total porosity versus the glass bead: epoxy mass mixing ratio.

3.3.2) Conductivity Measurements

The tests employed the configuration shown in Fig. 3.6 with a 10 kHz AC, 1 μA current input supplied from a constant current source (Keithly™ 6221) with the subsequent voltage responses obtained with a lock-in-amplifier (Stanford Research™ SR830). A strap-electrode design modified from Wang et al, (2009) was adopted. We used 30mm wide strap electrodes extending the length of the sample since this gave the most accurate results according to Wang et al., (2009). This meant that we were averaging our measurements over a large portion of the sample which we

believe to be desirable since we want to see how the crack affects the entire sample and not just the area nearest to the crack itself. The copper strap electrodes are attached to the acrylic mounting blocks (Fig. 3.7) that push the electrodes into contact with the sample.

A 2-electrode method was employed primarily because of the additional difficulties that use of a 4-electrode method would impose on the interpretation of the results within the essentially 2D configuration. A strong reason for using a 4-electrode method is to avoid electrode polarization effects, and consequently to minimize these here the measurements were taken at 10 kHz. In Chapter 2 we demonstrated that 2 and 4 electrode methods can give identical results.

Voltage measurements were recorded and converted to resistivity using Eqns. 3.2 and 3.3. As mentioned earlier the reported conductivity is just the inverse of resistivity. The value of η in Eqn. 3.4 is 25.73 as provided by Wang et al. (2009).

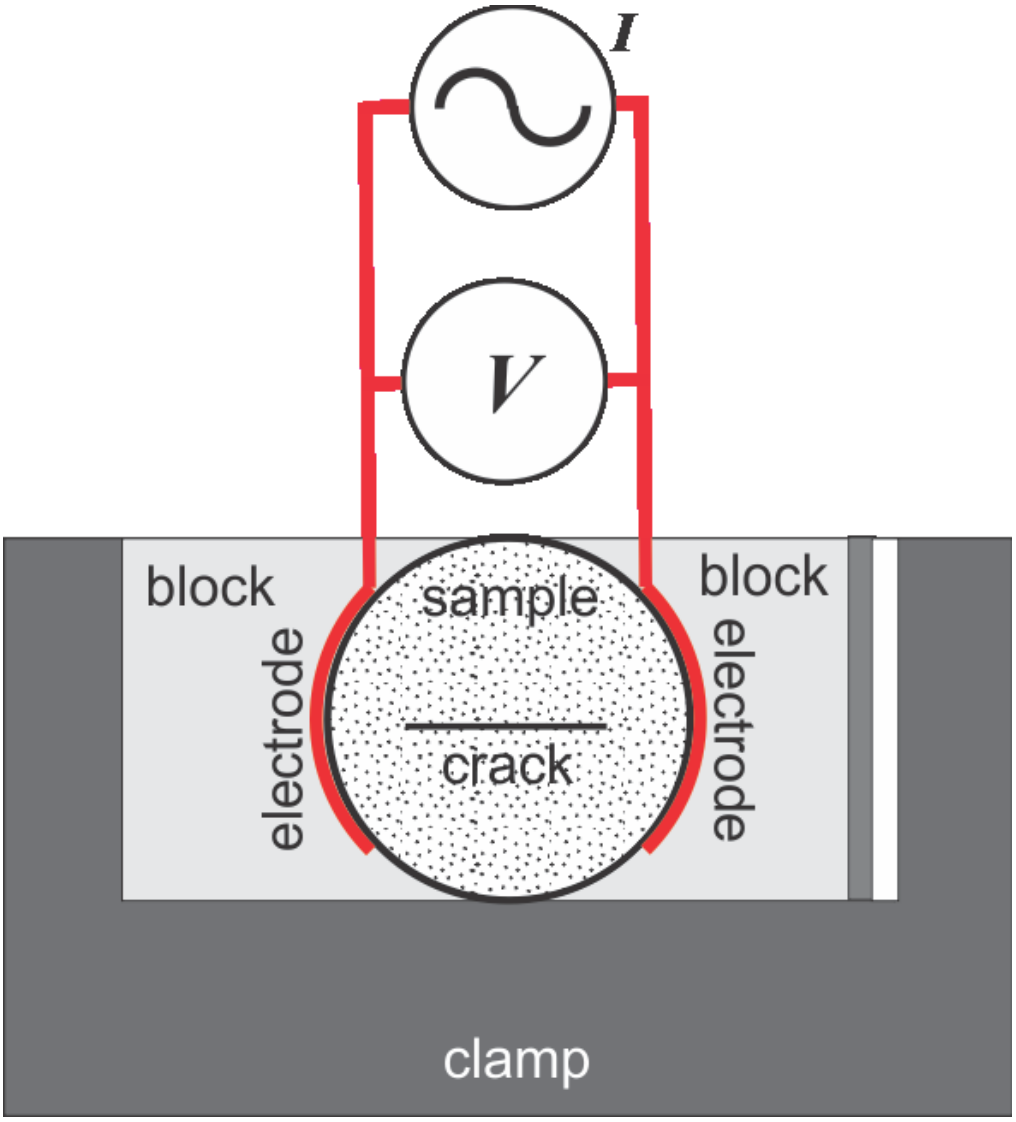

Figure 3.6. Experimental configuration consisting of sample shown oriented parallel to current flow between two strap-electrodes mounted in acrylic blocks. The clamp pushes the electrodes against the sample.

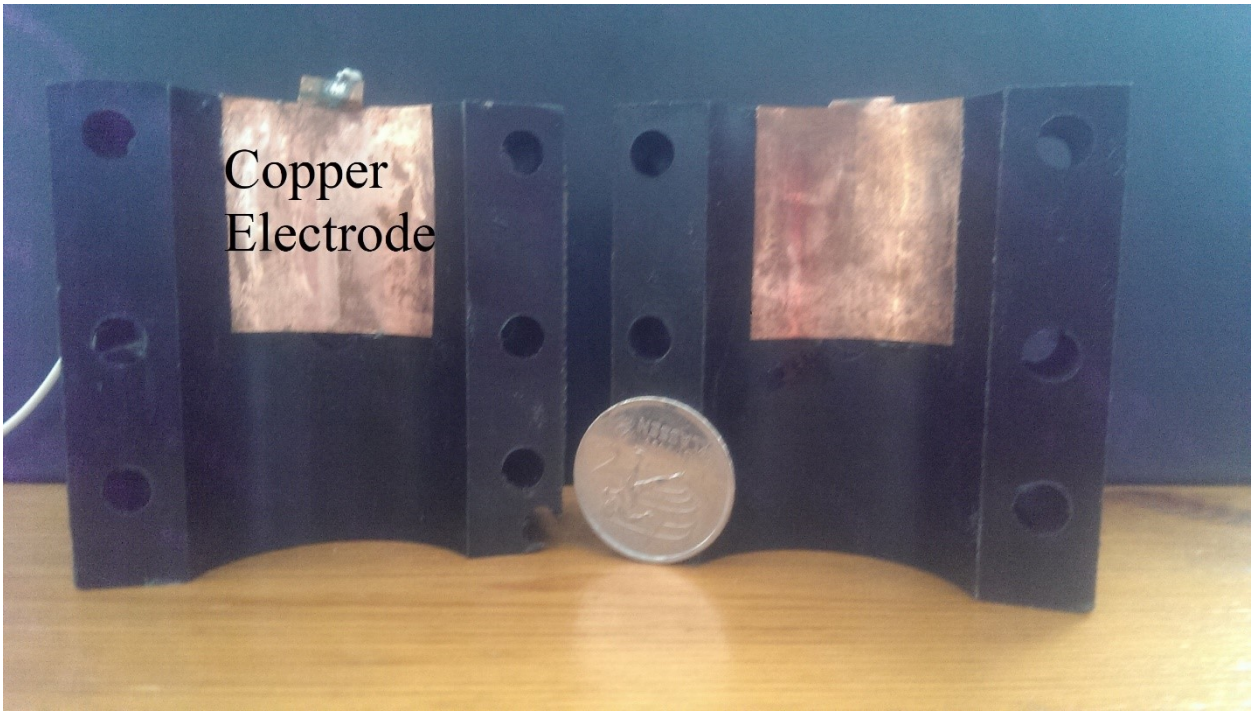

Figure 3.7. Photograph of acrylic blocks and copper electrodes. Canadian quarter with 23.81 mm diameter for scale.

The electrolyte-saturated sample was placed in between the acrylic sample holders and the clamp was used to ensure a good contact between the electrodes and sample. Three separate measurements were made in two directions; parallel and perpendicular to the strike of the fracture in each of the samples. The measurement order was altered for each pair of measurements. Evaporation during the tests was a concern as they were carried out in the open atmosphere at room conditions on the bench top. This effect was reduced by immersing the sample in the saturating electrolyte after each pair of parallel and perpendicular measurements. This led to a slow increase in the overall conductivity of the sample with each measurement. This is due to evaporation causing some salt to be left behind in the unsaturated part of the sample where fluids evaporated from followed by resaturation with the same electrolyte. This led to a slow increase in salinity of the electrolyte. This can be seen in Table 3.2. It means that the formation factors reported

are apparent formation factors and not true ones. Estimation of the true formation factor would require consistent fluid conductivities for all measurements. Uncertainty in individual measurements were based on the uncertainty in the recorded voltage (1% uncertainty) and the lengths measured for the geometric factor (+/- .02mm). They were ~10^{-3} S/m for samples with an 8:1 mixing ratio and ~5 x 10^{-4} S/m for samples with a 7:1 mixing ratio. Total uncertainties in the average anisotropy ratios also used the standard deviation in anisotropy ratios for individual measurements.

3.4) Results

The observed conductivities for all measurements along with anisotropy ratios are provided in Table 3.2 while the tortuosities, inverse formation factors and cementation exponents are reported in Table 3.3.

Table 3.2. Observed conductivities for measurements taken parallel and perpendicular to the fracture strike. The average anisotropy ratio is the average of the individual ratios that can be calculated from the individual measurements.

Sample ID	**Parallel conductivity (S/m)**	**Perpendicular conductivity (S/m)**	**Average parallel conductivity (S/m)**	**Average perpendicular conductivity (S/m)**	**Average Anisotropic ratio**
A1	0.113	0.107	0.117	0.114	1.024
	0.116	0.115			
	0.123	0.122			
A2	0.102	0.100	0.109	0.105	1.038
	0.110	0.105			
	0.114	0.109			
A3	0.145	0.136	0.148	0.140	1.055
	0.151	0.145			
	0.148	0.140			
A4	0.169	0.162	0.176	0.168	1.048

	0.178	0.171			
	0.180	0.170			
A5	0.152	0.143	0.159	0.148	1.070
	0.159	0.147			
	0.166	0.156			
A6	0.156	0.153	0.163	0.158	1.027
	0.162	0.156			
	0.172	0.168			
A7	0.177	0.177	0.185	0.180	1.026
	0.189	0.181			
	0.190	0.184			
A8	0.0676	0.0623	0.0686	0.0633	1.084
	0.0680	0.0635			
	0.0703	0.0642			
A9	0.0884	0.0839	0.0890	0.0848	1.050
	0.0891	0.0854			
	0.0897	0.0851			
A10	0.0810	0.0763	0.0862	0.0816	1.056
	0.0894	0.0844			
	0.0887	0.0848			
A11	0.0870	0.0800	0.0886	0.0829	1.069
	0.0881	0.0820			
	0.0908	0.0870			
A12	0.0900	0.0816	0.0928	0.0845	1.098
	0.0952	0.0864			
	0.0933	0.0856			
B2	0.183	0.181	0.188	0.188	1.004
	0.190	0.190			
	0.192	0.192			
B4	0.163	0.163			
	0.172	0.171	0.169	0.169	1.002
	0.172	0.172			

Table 3.3. Summary of formation factors (F), cementation exponents (m) and tortuosities (τ) in parallel and perpendicular directions

Sample ID	$\left(\frac{1}{F}\right)_{\perp\perp}$	$\left(\frac{1}{F}\right)_{\parallel}$	$\tau_{\perp\perp}$	$\tau_{\parallel}$	$m_{\perp\perp}$	$m_{\parallel}$
A1	0.064	0.067	3.81	3.72	1.96	1.94
A2	0.059	0.063	4.19	4.04	2.03	2.00

A3	0.080	0.084	3.24	3.08	1.87	1.83
A4	0.095	0.10	2.77	2.64	1.76	1.73
A5	0.084	0.090	3.04	2.83	1.82	1.76
A6	0.090	0.093	2.93	2.84	1.80	1.78
A7	0.10	0.11	2.53	2.46	1.69	1.67
A8	0.036	0.039	5.73	5.29	2.11	2.05
A9	0.048	0.051	4.28	4.07	1.92	1.89
A10	0.046	0.049	4.50	4.26	1.96	1.92
A11	0.047	0.050	4.33	4.05	1.92	1.88
A12	0.048	0.053	4.39	3.99	1.95	1.89

3.4.1) Absolute conductivity variation

As anticipated, the conductivity both parallel and perpendicular to the fracture plane generally increased with the total porosity φ (Fig. 3.8) which includes crack and regular matrix porosity. This was most apparent for the samples with mixing ratios of 8:1, but not noticeable with the samples using a 7:1 mixing ratio. In Fig. 3.8 the samples with 7:1 mixing ratio are clustered together in the low porosity section of the graph where they do not seem to fall along a trend on their own. It is also important to note that the samples are, again as anticipated, more conductive in the direction parallel to the fracture. Fig. 3.8 shows the average perpendicular and parallel conductivities as a function of porosity with Archie's law plotted for cementations exponents of 1.5 and 2 which are typical bounds for clean sandstones. They do not follow any obvious trend since the epoxy affects the cementation exponent in unpredictable ways. However, they generally fall inside the bounds expected for clean sandstone.

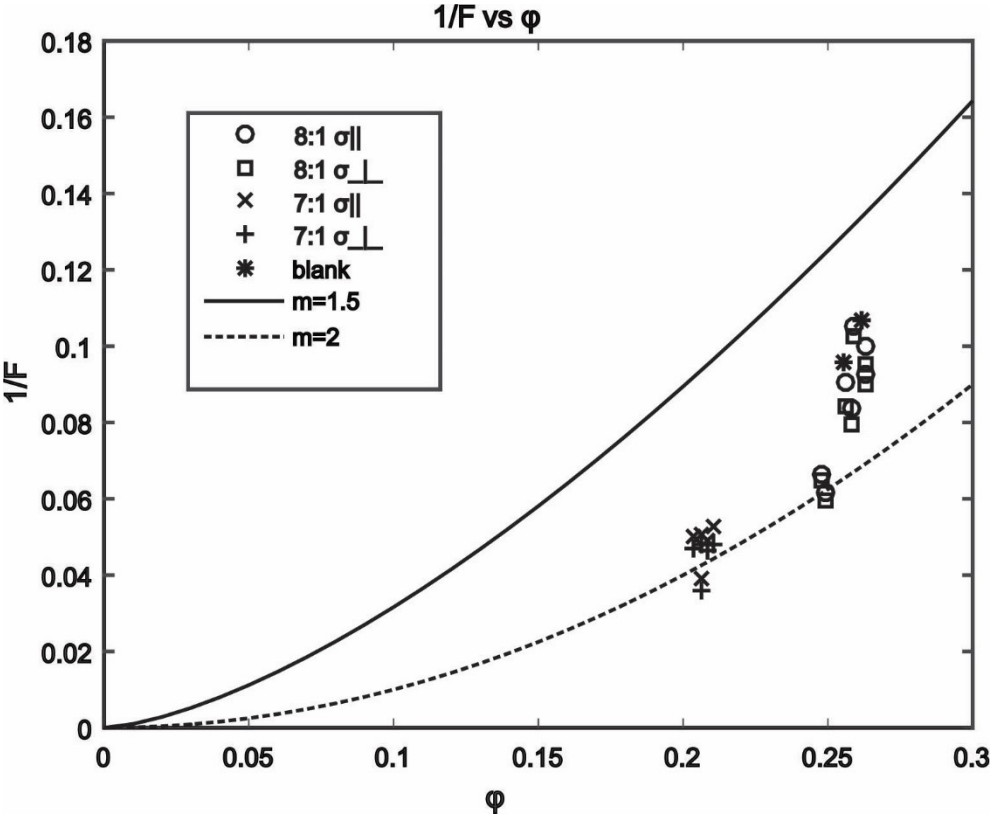

Figure 3.8. 1/F variation with porosity. Archie's law plotted for m=1.5 and m=2.

3.4.2) Anisotropy ratios

To measure the anisotropy, we look at the ratio of measured conductivities in the two principal directions parallel and perpendicular to the fracture and plot this as functions of the ratio of crack porosity to total porosity (Fig. 3.9). Although it displays some scatter and aside from one outlier, the anisotropy clearly increases with porosity ratio. In order to understand why sample A8 was such an outlier in the data we performed another microCT scan on this sample that revealed a heavily deviated fracture that extended from top to bottom. A comparative sample showed no such deviation. The crack porosity for this sample was higher than plotted and the geometry of the fracture is irregular. Fracture irregularities may also be responsible for some of the scatter in Fig. 3.9 as small errors in the manufacturing process could have resulted in some fractures being

slightly more curved than others. This could cause the samples to deviate from the true trend (that if the fractures were perfectly straight). The line of best fit is shown in Fig. 3.9 and the equation is given in Eqn. 3.8. The fit excludes the outlier datapoint and was a weighted least square fit. Weights were assigned to the data based on the magnitude of the uncertainties for each anisotropy ratio. An arbitrarily high weight of one million was used to force the fit through the point (0,1) which represents isotropy.

$$Anisotropy\ ratio = 3.47\left(\frac{\varphi_c}{\varphi}\right) + 1.00 \tag{3.8}$$

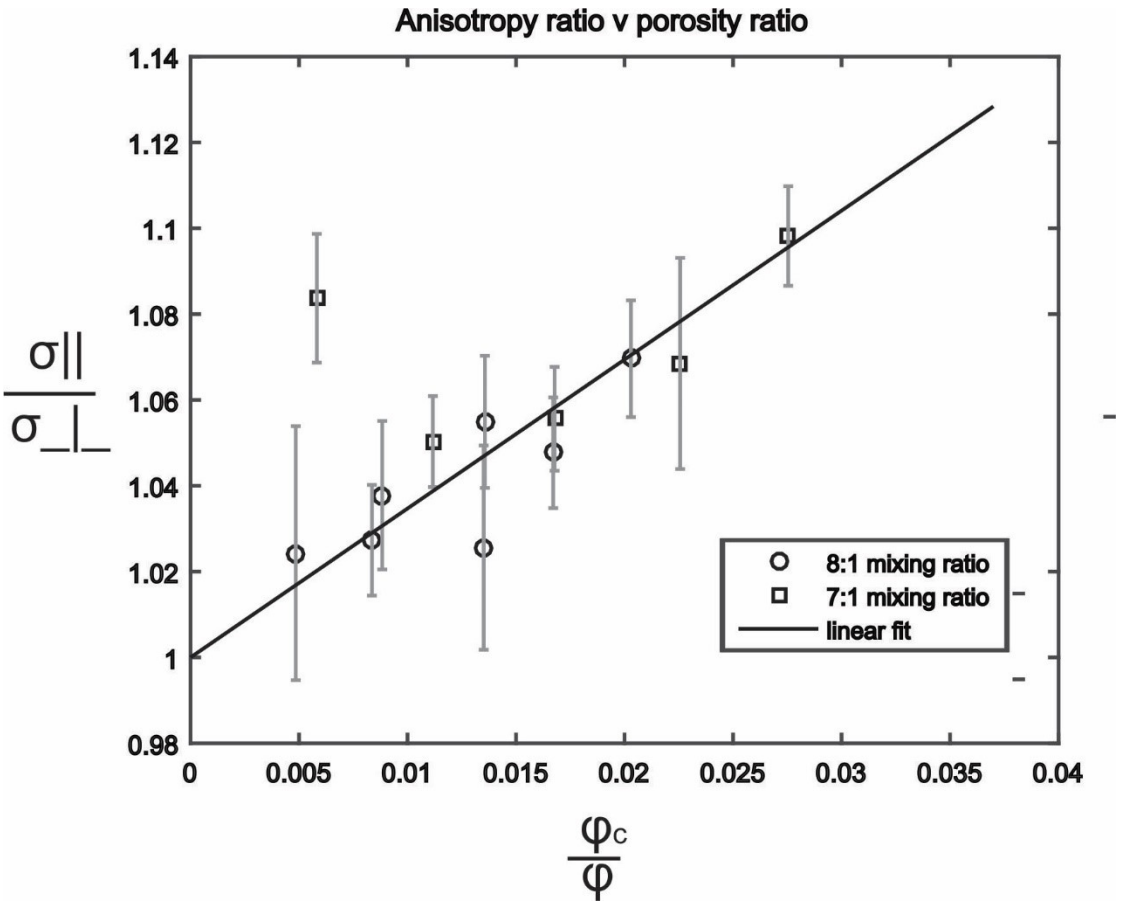

Figure 3.9. Anisotropy ratio as a function of crack porosity/total porosity ratio. Line of best fits excludes the outlier datapoint. Error bars are shown in grey.

The root mean square error for the fit to the data in Fig. 3.9 is 0.009 and the correlation coefficient for the data is 0.94.

As discussed in the theory section and in Chapter 2 the formation factor can be interpreted as the porosity connected by lines of current, and, fractures and narrow pore throats are weighted more heavily due to the higher density of electric field lines. Fractures oriented perpendicular to the electric field are not expected to be involved in conduction and so perpendicular measurements can be used as a proxy for conductivity of the unfractured matrix. We offer some experimental evidence of these claims by examining the change in inverse formation factor between the parallel and perpendicular measurement direction as a function of the crack porosity and plot a 1:1 trendline (Fig. 3.10).

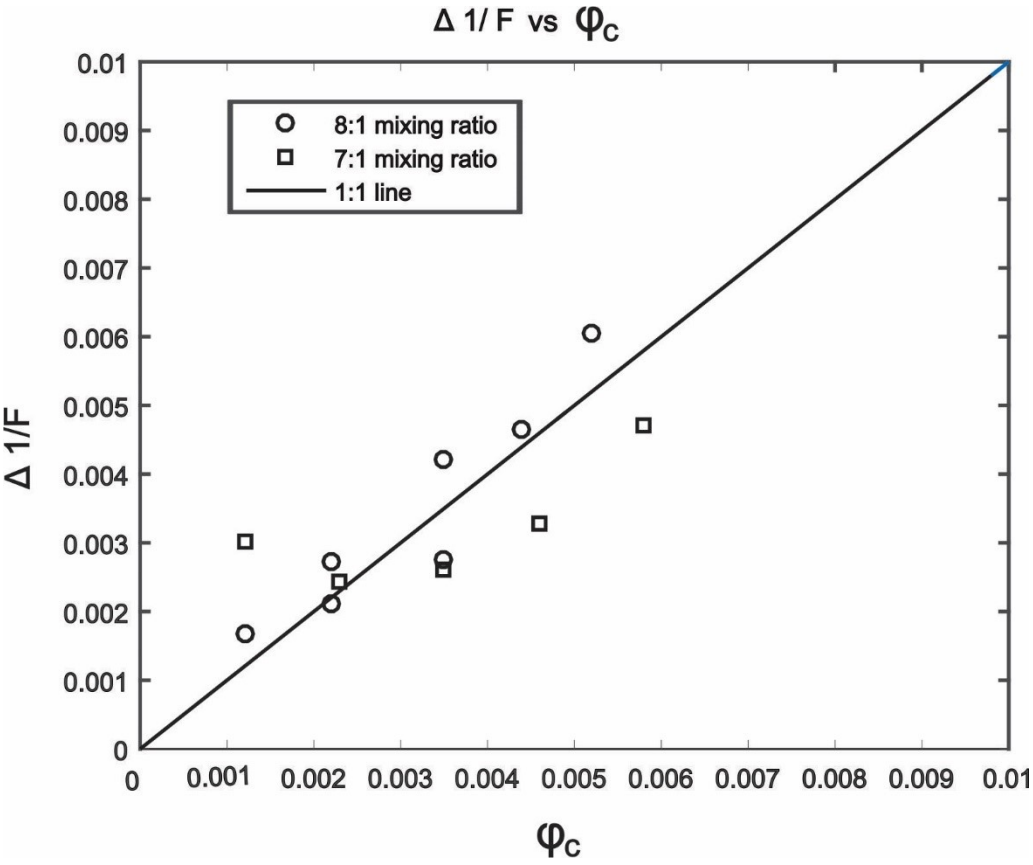

Figure 3.10. Change in the inverse formation factor (difference between 1/F in the two measurement directions) vs crack porosity.

3.5) Discussion

The results presented here show an obvious trend between conductivity anisotropy and $\frac{\varphi_c}{\varphi}$ for a material with aligned fractures and an isotropic matrix. This is an important step in quantifying how fractures affect electrical conductivity. We note that the preceding was limited to rocks with a relative high background porosity whereas fractures are expected to dominate pore space conduction at low matrix porosities. However, the observed trend agrees with that expectation and further work like this can be used to help constrain the empirical relationship derived here (Eqn. 3.8) at lower matrix porosities.

An important point to discuss is how the anisotropy of the measured samples compares to previously published anisotropy ratios. We will restrict the following discussion to lab data as ratios found in the field are associated with features that exist at reservoir and regional scales (eg. Brown et al. 2012; Leibecker et al., 2002).

Woodruff et al (2014) showed shales with anisotropy ratios on the order of 10 that decreased with electrolyte conductivity. Woodruff et al. (2015) perform similar measurements and showed anisotropy ratios of 30. However, the reported fluid conductivity was .01 S/m which us sufficiently low that surface conductivity is expected to dominate. Both these results show that surface conductivity dominated in a low salinity environment; and consequently, the surface conductivity in their shales was more anisotropic than pore space conductivity. However, even at high salinities, samples used in those studies were far more anisotropic than those presented here and this can be explained by the fact that shales are composed of grains that are aligned perpendicular to the direction of compaction during diagenesis (Bachrach, 2011). This results in a pore space that is directionally anisotropic.

David et al. (2017) and North and Best (2013) both showed that anisotropy may be much more prevalent than is usually assumed. Using a novel geometry on three samples from two different blocks of porous sandstones (fractional porosities of 0.26 to 0.28), David et al. (2017) measured the full conductivity tensor finding ratios between the maximum and minimum principal conductivities (~1.09 and 1.15) that were similar to those found here. North and Best (2013), from unique measurements on four different quarried quartz sandstones with porosities between 0.13 and 0.23, showed that even these clean sand formations, which are often assumed to be isotropic, were anisotropic with conductivity ratios ranging from 1.15-1.25. Their observed ratios exceed the values here although it seems plausible that lowering the background porosity below

20 percent or increasing the crack porosity further could produce ratios in this range for the types of samples used in this study. This highlights the usefulness making measurements on controlled samples because a truly isotropic background matrix porosity is very difficult to find in nature. The only way to then understand how fractures interact with the background porosity is therefore through experiments like this where the isotropy of the background matrix can be guaranteed, and the orientation of the fractures is known. These are difficult things to verify in studies on natural specimens.

The results presented here can be used for both modeling changes in conductivity and fluid flow. In instances when a reservoir is expected to have new fractures forming (for instance after hydraulic fracturing), it is desirable to know how the newly formed fractures will interact with the initial porosity. Eqn. 3.8 can be used to calculate the change in conductivity in the direction fractures are expected to align in the ambient stress field. The change in conductivity corresponds to a change in the inverse formation factor which can then be used to update the tortuosity. These values can then be used to model the new electrical imaging response or compute new tortuosity factors for use with permeability prediction (Johnson et al, 1986).

3.6) Conclusions

We have presented measurements on materials with oriented fracturess in an isotropic background matrix. These samples show an increase in anisotropy with increasing ratio of crack porosity to total porosity up to a maximum of ~1.1. These results can be used to help predict changes in conductivity expected when a reservoir is fractured which can in turn be used to inform transport models for the reservoir. Further work is required to constrain Eqn. 3.8 at higher $\frac{\varphi_c}{\varphi}$ ratios and extend this analysis to examine the effects of fractures on the full conductivity tensor. This work

represents a starting point in constraining the effects of fractures in porous media. Future work will extend data to higher values of $\frac{\varphi_c}{\varphi}$ and compare trends seen experimentally to those seen numerical models of conducting saturated grain packs.

Acknowledgements – This work was funded within Dr. Schmitt's NSERC Discovery Grant. Special thanks to Randolf Kofman for his assistance with the lab work.

3.7) References

Abousrafa, E. M., J. M. Somerviller, S. A. Hamilton, and P. W.H. Olden (2013). A laboratory measurement technique for axial and radial resistivity at ambient or reservoir stress state conditions. *Journal of Petroleum Science and Engineering* 102: 57-65.

Anderson, B., B. Bryant, M. Lu ling, B. Spies, and K. Helbig (1994). Oilfield anisotropy: Its origins and electrical characteristics. *Oilfield Review:* 48–56.

Archie, G. E. (1942). The electrical resistivity log as an aid in determining some reservoir characteristics. *Transactions of the American Institute of Mining and Metallurgical Engineers* 146: 54-62.

Bachrach, R. (2011). Elastic and resistivity anisotropy of shale during compaction and diagenesis : Joint effective medium modeling and field observations. *Geophysics* 76 (6): E175-E186.

Brown, V., M. Hoversten, K. Key, and J. Chen (2012). Resolution of reservoir scale electrical anisotropy from marine CSEM data. *Geophysics* 77 (2): E147-E158.

David, C., P. Robion, and L. Laurent (2017). "A single laboratory setup for investigating the anisotropy of both seismic and electrical properties in core samples." *Geophysical Journal International* 210: 1595-1608.

Ellis, M., M. Sinha, and R. Parr (2010). Role of fine-scale layering and grain alignment in the electrical anisotropy of marine sediments. *First Break* 28 (9): 49-57.

Han, T.C. (2018). Joint Elastic-Electrical Properties of Artificial Porous Sandstone With Aligned Fractures. *Geophysical Research Letters* 45 (7): 3051-3058.

Han, T.C., M. Josh, and H. Liu (2019). Effects of aligned fractures on the dielectric properties of synthetic porous sandstones. *Journal of Petroleum Science and Engineering* 172: 436-442.

Hill, D. G. 1972. Laboratory investigation of electrical anisotropy in precambrian rocks. *Geophysics* 37 (6): 1022-1038.

Johnson, D. L., T. J. Plona, and H. Kojima (1986). Probing porous media with 1st sound, 2nd sound, 4th sound and 3rd sound. Edited by R. Jayanth, J. Banavar and K. W. Winkler. *Physics and Chemistry of Porous Media.* New York. 243-277.

Leibecker, J., A. Gatzemeier, M. Honig, O. Kuras, and S. Wolfgang (2002). Evidence of electrical anisotropic structures in the lower crust and the upper mantle beneath the Rhenish Shield. *Earth and Planetary Science Leters* 202: 289-302.

Louis, L., C. David, and P. Robion (2003). Comparison of the anisotropic behaviour of undeformed sandstones under dry and saturated conditions. *Tectonophysics* 370 (1-4): 193-212.

Marti, A (2014). The Role of Electrical Anisotropy in Magnetotelluric Responses : From Modelling and Dimensionality Analysis to Inversion and Interpretation. *Surveys in Geophysics* 35: 179-218.

Mendelson, K., and M. Cohen (1982). The effect of grain anisotropy on the electrical properties of sedimentary rocks. *Geophysics* 47 (2): 257-263.

Newman, G., M. Commer, and J. Carazzone (2010). Imaging CSEM data in the presence of electrical anisotropy. *Geophysics* 75 (2): F51-F61.

North, L., A. Best, J. Sothcott, and L. Macgregor (2013). Laboratory determination of the full electrical resistivity tensor of heterogeneous carbonate rocks at elevated pressures. *Geophysical Prospecting* 61: 458-470.

North, L., and A. Best (2014). Anomalous electrical resistivity anisotropy in clean reservoir sandstones. *Geophysical Prospecting* 62: 1315-1326.

Rathore, J S, E Fjaer, R M Holt, and L Renlie (1994). P- and S- wave anisotropy of synthetic sandstone with controlled crack geometry. *Geophysical Prospecting* 43: 711-728.

Revil, A., and L. Cathles (1999). Permeability of shaly sands. *Water Resources Research* 35 (3): 651-662.

Revil, A., W. Woodruff, and M. Prasad (2013). Complex conductivity tensor of anisotropic hydrocarbon-bearing shales and mudrocks. *Geophysics* 78 (6): D403-D418.

Robion, P., F. Humbert, J. C. Colombier, S. Leghay, and D. Frizon de Lamotte (2012). Relationships between pore space anisotropy and anisotropy of physical properties of silicoclastic rocks from the Corbi??res-Minervois fold-and-thrust-belt (north-east Pyrenees, France). *Tectonophysics* 576-577: 63-77.

Schlumberger, C., M. Schlumberger, and E. G. Leonardon (1934). Some Observations Concerning Electrical Measurements in Anisotropic Media and Their Interpretations. *Trans, AIME* 110: 159-182.

Sen, P., C. Scala, and M. Cohen (1981). A self-similar model for sedimentary rocks with application to the dielectric constant of fused glass beads. *Geophysics* 46 (5): 781-795.

Tranter, T. G., M. Tam, and J. T. Gostick (2018). The Effect of Cracks on the In-plane Electrical Conductivity of PEFC Catalyst Layers. *Electroanalysis* 30: 1-6.

Wamsley, P., and R. Fisher (2017). Determination of the resistivity anisotropy of orthorhombic materials via transverse resistivity measurements. *Review of Scientific Instruments* 88 (4): 9.

Wang, Z., L. Gellus, and F. Kong (2009). Simultaneous core sample measurements of elastic properties and resistivity at reservoir conditions employing a modified triaxial cell - A feasibility study. *Geophysical Prospecting* 57 (6): 1009-1026.

Wang, Z., R. Wang, T. Li, and M. Zhao (2017). The combined effects of pore structure and pore fluid on the acoustic properties of cracked and vuggy synthetic rocks. *Journal of Petroleum Science and Engineering* 156: 202-211.

Wang, Z., D. Schmitt, and R. Wang (2015). Does wettability influence seismic wave propagation in liquid saturated porous rocks. *Geophysical Journal International* 203: 2182-2188.

Woodruff, W. F., A. Revil, and C. Torres-Verdin (2014). Laboratory determination of the complex conductivity tensor of unconventional anisotropic shales. *Geophysics* 79 (5): E183-E200.

Woodruff, W. F., A. Revil, and M. Prasad (2015). Measurements of elastic and electrical properties of an unconventional organic shale under differential loading. *Geophysics* 80 (4): D363-D383.

Wyllie, M R., and W. D. Rose (1950). Some theoretical considerations related to the quantitative evaluation of the physical charactaristics of reservoir rock from electrical log data. *Journal of Petroleum Technology* 2 (4): 105-118.

Zisser, N., and G. Nover (2009). Anisotropy of permeability and complex resistivity of tight sandstones subjected to hydrostatic pressure. *Journal of Applied Geophysics* 68 (3): 356-370.

Chapter 4

Induced polarization in artificial sediments

4.1) Introduction

The frequency-dependent complex resistivity $\rho^*(\omega)$, which is often called the spectral induced polarization (SIP) in the geophysical literature, quantifies the capacity of a porous rock or soil to both transmit electrical current and to store charge. SIP responses offer insights into pore-scale structures and interfacial processes within a fluid-saturated porous medium. At low frequencies (0.0001-100 Hz) pore-space topology (Titov et al., 2002; Marshall and Maden,1959) and electro-chemical interactions at the grain - pore fluid interface (Revil and Glover, 1998; Revil, 2012) control the extent of charge stored (i.e. the capacitance) during passage of current. Consequently, the SIP depends in part on the porous material's permeability and fluid-saturation.

This linkage between SIP responses and petrophysical properties makes it valuable in mapping subsurface contaminants (Vanhala 1997) and in predicting permeability (Revil et al.. 2015, Slater and Lesmes, 2002) using various relationships (e.g., VanGenuchten, 1980). The non-invasive nature of field electrical tomography measurements may allow for the economic mapping of clean and permeable aquifers. Its utility can be extended to the monitoring of geological CO_2 sequestration as well as oil and gas exploration since the response is heavily dependent on partial water saturation (Jougnot et al., 2010). More recently SIP measurements have also been used to monitor biological processes in porous media including the biodegradation of hydrocarbons (Ustra, et al. 2016), the growth of microbial films (Atekwana and Slater, 2009), and the precipitation of sulphide minerals (Williams, et al. 2009).

Here, we focus on the interpretation of complex resistivity spectra at low frequencies in sandy sediments, i.e., those composed of primarily of nonconducting sand-sized mineral grains but also containing modest amounts of clay (<12% by weight). A consensus on how to physically interpret observed spectra from these materials remains elusive, and two classes of models have been proposed in which either Stern layer (Revil, 2013) or membrane (Titov et al., 2002; Marshall and Madden, 1959) polarization dominate. The problem is further complicated because both mechanisms, which are discussed in more detail below, may also simultaneously contribute to observed responses.

The objective of this work is to address the issue of which mechanism controls electrical relaxation in weakly polarisable sediments. This is accomplished with controlled complex electrical resistivity measurements on analog sediments constituted of mixtures of glass beads and various clays. In the remainder of the paper we provide a brief review of the relevant theoretical relationships and the existing conceptual models for conductance in porous media, describe the measurement procedure and experimental details and interpret the observed results in the context of existing mechanistic models and other published results. A practical goal of this work is to test differing decomposition strategies for extracting representative relaxation times. Extracting representative relaxation times is important for permeability prediction. The contribution concludes with a discussion on how the findings affect interpretation of SIP data.

4.2) Background

In this section we first briefly provide the essential theoretical relationships, provide an overview of the models proposed to describe the complex resistivity and low frequency polarization of sandy sediments, and review the pertinent literature.

Basic Theoretical Relationships and Definitions

The response of a material to an input electrical signal is generally described by either the complex resistivity:

$$\rho^* = \rho' + i\rho'' \qquad (4.1a)$$

or the complex conductivity:

$$\sigma^* = \sigma' + i\sigma'' \qquad (4.1b)$$

where the superscripts $*$, ', and " respectively indicate complex, real (in-phase), and imaginary (out-of-phase or quadrature) values. It is worth noting that equations 4.1a and 4.1b are the inverse of each other (i.e., $\sigma^* = \frac{1}{\rho^*}$). These parameters are generally frequency dependent and this dispersive behaviour can provide insight on the various electrical relaxation processes existing in an uncharacterized material.

In the laboratory, the complex resistivity of a sample under study is obtained first by finding its sample-dependent complex impedance Z^*. This is accomplished at a given frequency ω by injecting a known harmonic current $I^*(t) = I_o e^{j\omega t}$ while measuring the resulting harmonic potential

$V^*(t) = V_o e^{(i\omega t \pm \theta)}$ with phase lag θ relative to $I(t)$ across the sample. According to Ohm's law, this impedance Z is then simply

$$Z^* = \frac{V^*}{I^*} = \frac{V_o}{I_o} e^{-i\theta} = Z_o e^{-i\theta} \tag{4.2}$$

Euler's formula

$$e^{i\theta} = cos(\theta) + isin(\theta) \tag{4.3}$$

is substituted to recast Z^* into its real and imaginary parts

$$Z^* = Z_0 \cos(\theta) + iZ_0 \sin(\theta) = Z' + Z'' \tag{4.4}$$

with real (in-phase) Z' and imaginary (out-of-phase) quadrature Z'' components. From Eqn. 4.4, the phase θ may be written

$$\theta = arctan\left[\frac{Z''}{Z'}\right] \approx \frac{Z''}{Z'} \tag{4.5}$$

valid if Z'' is small relative to Z'.

To convert the sample impedance into a material property, the sample's geometric factor G, that in simple axially symmetric samples will depend on the sample length L and cross-sectional area A, must be found. For the simple case of a circular cylinder with the electrode in contact with the entire cross-section's face, this is simply $G = L/A$. The corresponding electrical properties are then:

$$\rho^* = \frac{1}{\sigma^*} = GR^* \tag{4.6}$$

The frequency dependence of the electrical properties contains valuable information about the material's SIP; the measurements obtain real-valued $\rho'(\omega)$ and quadrature $\rho''(\omega)$ spectra.

Examination of Eqn. 4.5 suggests that $\rho''(\omega)$ is more directly related to the phase; and hence a goal may be to find the peak, or characteristic, frequency f_p from the $\rho''(\omega)$ whereby the material's characteristic relaxation time $\tau_c = 1/2\pi f_p$ may be found. As will be further discussed, this τ_c would ideally be related to a single relaxation, but in reality, the real material behaviour is more complicated. Real materials exhibit multiple relaxation processes occurring over different time/length scales. The contribution of each process is weighted by the chargeability (*M*) associated with that process. *M* can be defined as the normalized conductivity change across a frequency band for SIP or as the ratio of the secondary to primary voltage for time domain measurements (Sumner ,1976; Weller et al., 2013).

In earth materials the in-phase component ρ' only weakly depends on frequency. In contrast, the frequency dependence of the quadrature term ρ'' (most representative of the phase lag by Eqn. 4.5) is more variable and arises from a combination of dielectric and electrochemical polarisations that exhibit more complicated nonlinear behaviour. At low frequencies (meaning here, typically less than 1 kHz) dielectric polarisations generally contribute negligibly to the quadrature resistivity $\rho''(\omega)$. At these frequencies, however, the phase lags observed in sandy sediments are large. The large polarisations are instead due to processes occurring at the grain-fluid interface arising from charge imbalances that develop at the pore/grain scale. The frequency at which a phase lag is observed corresponds to the relative length scale over which charge imbalances develop. Therefore, at high frequency, phase lags represent polarization occurring over relatively smaller distances compared to those at lower frequencies. Electrochemical polarisations are consequently believed to reveal information about processes occurring over lengths that correspond to the grain or pore throat diameter/length.

Rocks and sediments often exhibit complicated quadrature spectra; and this is largely attributed to effects dependent on the distribution of polarization length scales (Leroy et al., 2008). For sandy sediments discussed here, the distribution could be influenced by either or both of the Stern layer or membrane polarizations; but it is still not clear which mechanism dominates any given spectrum. Examination of the characteristic relaxation time τ_c determined from the quadrature conductivity spectrum $\rho''(\omega)$ may provide insight into which mechanism is the most important.

There is now a large amount of evidence that the relaxation time in these materials correlates closely to the pore diameter (e.g., Revil et al., 2012; Revil et. al., 2015; Scott and Barker, 2003) although no polarisation mechanism has been suggested that would only operate in the pore throats. Unfortunately, the grain perimeters, pore-throat diameters, and pore-throat lengths are all geometrically related. Therefore, any mechanism associated with one of those length scales would correlate to all of them.

4.2.1) Electric Double Layer (EDL)

The electrical double layer (EDL) around a negatively charged grain immersed in an electrolyte is conceptually illustrated in Fig. 4.1a. The surfaces of clay minerals tend to be negatively charged. This is partly due to isomorphic substitutions that arise from defects in the mineral lattice and from pH dependent reactions with the pore water (Brady et. al.,1996). Silica glass and quartz grains also develop a surface charge primarily due to proton equilibria (Leroy et al., 2008). Once immersed in the electrolyte, ions with charge sign opposite to that of the mineral (hereafter referred to as counter ions of positive charge such as Na^+ and Ca^{++}) weakly adsorb to the mineral surface. This creates a first layer, commonly called the *Stern layer*, of confined counter ions that do not interact with the bulk pore electrolyte. Outside of this is a second *diffuse layer* in which the concentration

of counter ions is greater than that of the bulk electrolyte and from which the exchange of ions with the bulk electrolyte is allowed. Together, these first and second layers are referred to as the *double layer*; their existence is consistent with molecular dynamic simulations (Wang et. al., 2008). They are most pronounced in low concentration electrolytes where the counterion charge density is much greater at the mineral surface than it is in the bulk electrolyte. Much of the theory was originally developed to describe double-layer phenomena for colloidal suspensions where the mineral particles together with their associated double layers are isolated (Fig. 4.1a). In rocks and soils the situation is complicated because the mineral grains are in contact and this forces the diffuse layers to overlap (Fig. 4.1b). This is agreed upon by proponents of both classes of IP models (Revil, 2012;Titov, et al. 2002).

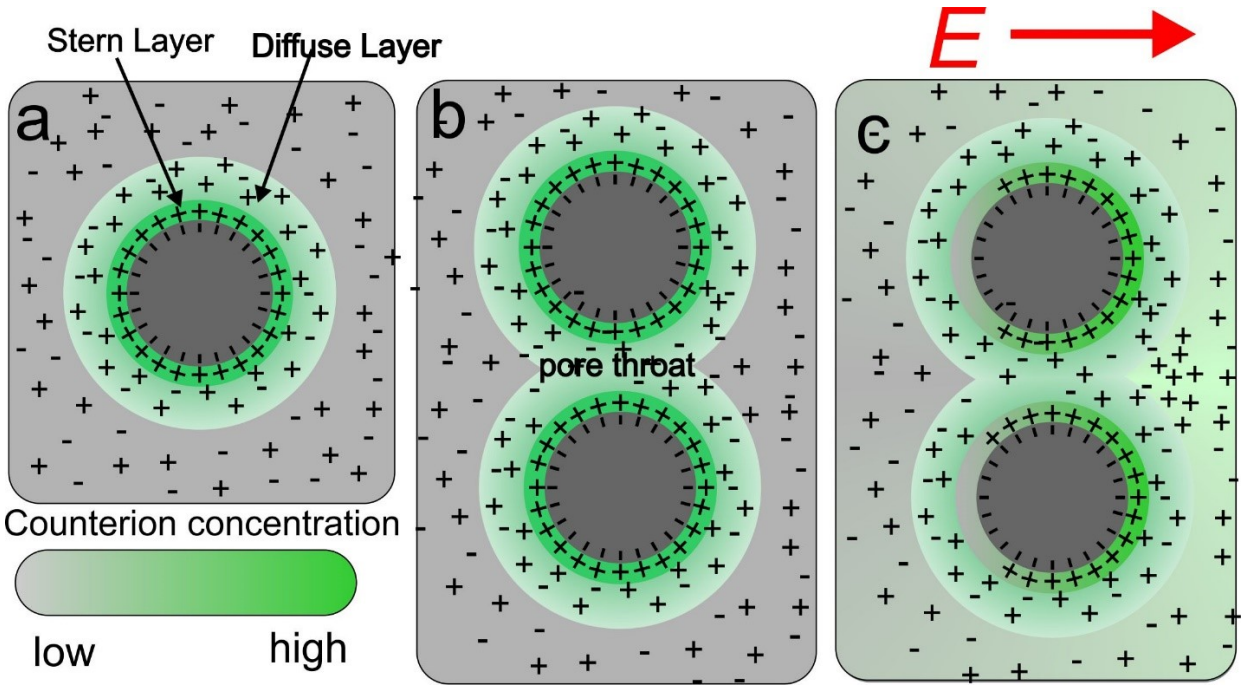

Figure 4.1. (a) Formation of electrical double layer at and near the mineral surface. Stern layer immediately adjacent to mineral surface in dark green. Diffuse layer shown as lighter shaded green area. Bulk electrolyte as grey region. (b) In the region between the mineral grains (i.e. the pore throat), the Stern layers are disconnected but the diffuse layers overlap and would be continuous throughout the porous medium. (c) Two polarisation mechanisms at work under an applied electric field. The Stern layer polarisation occurring simultaneously with membrane polarisation as clay counterions are displaced as current flows through the narrow pore throat.

4.2.2) Models

The complex resistivity of rocks is often simply described by a parallel resistor model shown in Fig. 4.2 (Waxman and Smits,1968). In terms of conductivity:

$$\sigma^*(\omega) = \sigma_f' + \sigma_s'(\omega) + i\sigma_s''(\omega) \tag{4.7}$$

where σ_f' is the in-phase conductivity due to charge migration through the electrolytic pore fluid, σ_s' is the in-phase conductivity due to charge migration along grain surfaces in the electrical double

layer of the minerals, and σ_s'' is the quadrature component of the surface conductivity caused by polarisation. When necessary, more complicated models can be developed to account for multiple polarisation processes over the frequency range, but at lower frequencies this is probably an appropriate representation given the current understanding polarisation effects.

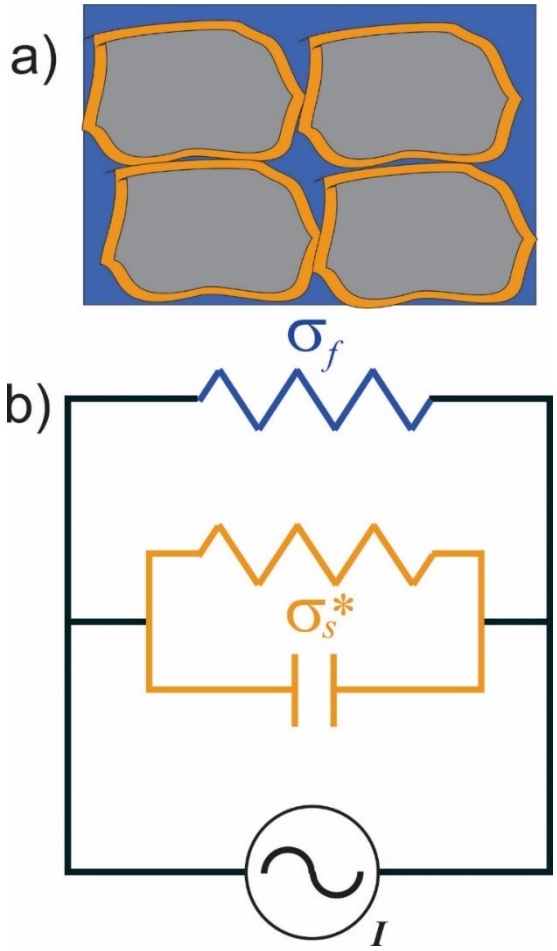

Figure 4.2. a) Simplified microscopic cross-section through a porous rock with solid portions in grey, surface charge layers in orange and electrolyte liquid (blue) saturated pore space. b) Equivalent circuit for the rock in which the overall complex conductivity $\sigma^*(\omega)$ consists of parallel conductive pathways through the electrolyte liquid and along grain boundaries. The solid minerals in grey are considered to be electrical insulators.

At frequencies above 100 Hz Maxwell-Wagner polarisation dominates. This is attributed to interfacial effects between the bulk electrolyte and the electrical double layer or the grain surface and the electrical double layer. Maxwell-Wagner responses (non-zero quadrature conductivity at frequencies below those where dielectric polarization would be important) have been well predicted using Differential Effective Medium (DEM) theory (see Chelidze and Gueguen, 1999) for an overview of this approach) which calculates the complex permittivity of a two-material composite. The most important result of this approach is following Revil (2012):

$$\sigma^* = \frac{\sigma_f}{F}\left(\frac{1-\frac{\sigma_s^*}{\sigma_f}}{1-\frac{\sigma_s^*}{\sigma^*}}\right)^m \tag{4.8a}$$

$$F = \varphi^{-m} \tag{4.8b}$$

which is the same as the long-standing Bruggeman-Hanai equation (Bruggeman, 1935; Hanai, 1968) where a star in the superscript indicates a complex quantity and subscripts are the same as previously described. F is the formation factor which has been shown to be the porosity dynamically connected by lines of current through the total pore space (Revil and Cathles, 1999; (Avellaneda and Torquato,1991). The F in Eqn. 4.8b is the formation factor as it is expressed in Archie's (1942) law where φ is the connected porosity and m is the so-called cementation exponent.

Differential Effective Medium (DEM) theory can be used to derive expressions similar to Archie's (1942) law and the Waxman Smits equation (Bussian, 1983, Sen et. al., 1981). Regardless, at lower frequencies <100Hz, DEM fails to predict the large polarisations observed in rocks and soils.

In this lower frequency range, the polarisations primarily arise due to the existence of the electrical double layer (EDL) but take place on length scales larger than Maxwell-Wagner polarisation. For a broad pH range of 4-10 for the saturating liquid (Revil and Glover, 1998), the solid portions of

the porous materials, composed for example as quartz grains or glass beads, do develop surface charges, but it can be experimentally shown that polarisation through a pack of such clean grains is typically weak (Klein and Sill 1982; Leroy et al., 2008). The addition of small amounts of clay minerals to such a bead pack increases the polarization dramatically as evidenced by larger quadrature conductivity. However, it must be stressed that this holds only for small amounts of clay. Paradoxically, the addition of even more clay increases the surface conductivity further, thus easing charge mobility and potentially reducing the mixture's capacity to store charge (Vacquier, 1957). We say "potentially" here because processes such as lithification and fluid flow play a role in the evolution of pore space topology and polarizability of the sediments. This makes it difficult to make any definite statements based on clay content alone.

Under an applied electric field, two mechanisms are thought to be responsible for the observed electrochemical polarisations and electrical relaxation times at low frequency (Fig. 4.1c):

1. Stern layer polarisation: the inner layer of the electrical double layer polarises as counter ions migrate tangentially along the grain boundaries (Revil, 2012, Revil 2013, Jougnotet al., 2010). In this case the grain size or specific surface area of the particle being polarized will exercise control over the peak frequency in the quadrature spectrum.

2. Membrane polarisation: clay counter ions are displaced from the diffuse layer that overlaps at grain contacts (Madden and Marshall, 1959; Titov et al., 2002). The excess accumulation of ions in turn causes electrolyte blockage at the pore throat boundary. This leads to a higher relative concentration of counterions at one end of each pore-throat. In this case, the length scale over which these charge imbalances develop would be associated with the average pore throat length at the "active" grain contacts (an active grain is defined as one where the electrical double layer is pronounced enough to control the observed polarisation). This means that the peak frequency is

not necessarily tied to the available surface area of those mineral grains (i.e. clays) with a pronounced electrical double layer, but instead is more closely related to the dimensions of the pore space topology that is primarily influenced by the rock's supporting structural framework of the "passive" grains (defined as grains with either no EDL coating them or a small EDL which contributes little to observed polarisation). The charges redistribute themselves once the electric field is removed and the material regains electro-neutrality at the pore scale. The time taken for electro neutrality to be achieved is theoretically the characteristic electrical relaxation time τ_c.

To reiterate, this is either controlled by the grain size in the case of Stern layer polarisation or by the lengths of the idealized pore throats along which clay counter ions are displaced in the case of membrane polarisation. These are simplified conceptualisations of what occurs but they do capture what the length scales are for each process. Further discussion on the role of diffusivity is presented later.

4.2.3) Characteristic Spectra

In SIP measurements, the complex resistivity is recorded over a broad range of frequencies (mHz - kHz) producing spectra for the real $\rho'(\omega)$ and imaginary $\rho''(\omega)$. Here, we attempt to distinguish between membrane polarisation and Stern layer polarisation using measurements on 8 artificial porous samples constructed from a glass beads of differing sizes mixed with small amounts of clays with varying electrochemical properties. These SIP measurements were conducted in a frequency range of 10 mHz to 1 kHz with the goal being to distinguish whether the dimensions of the glass beads or the surface characteristics of the clays had greater control over the observed response.

A further complication is that sediments rarely display a single relaxation time, instead tending to exhibit a distribution of times due to a distribution of length scales over which the charge imbalances develop. Fig. 4.3 shows hypothetical illustrative cases of the types of phase spectra $\theta(\omega)$ that may be expected at frequencies below 100 Hz.

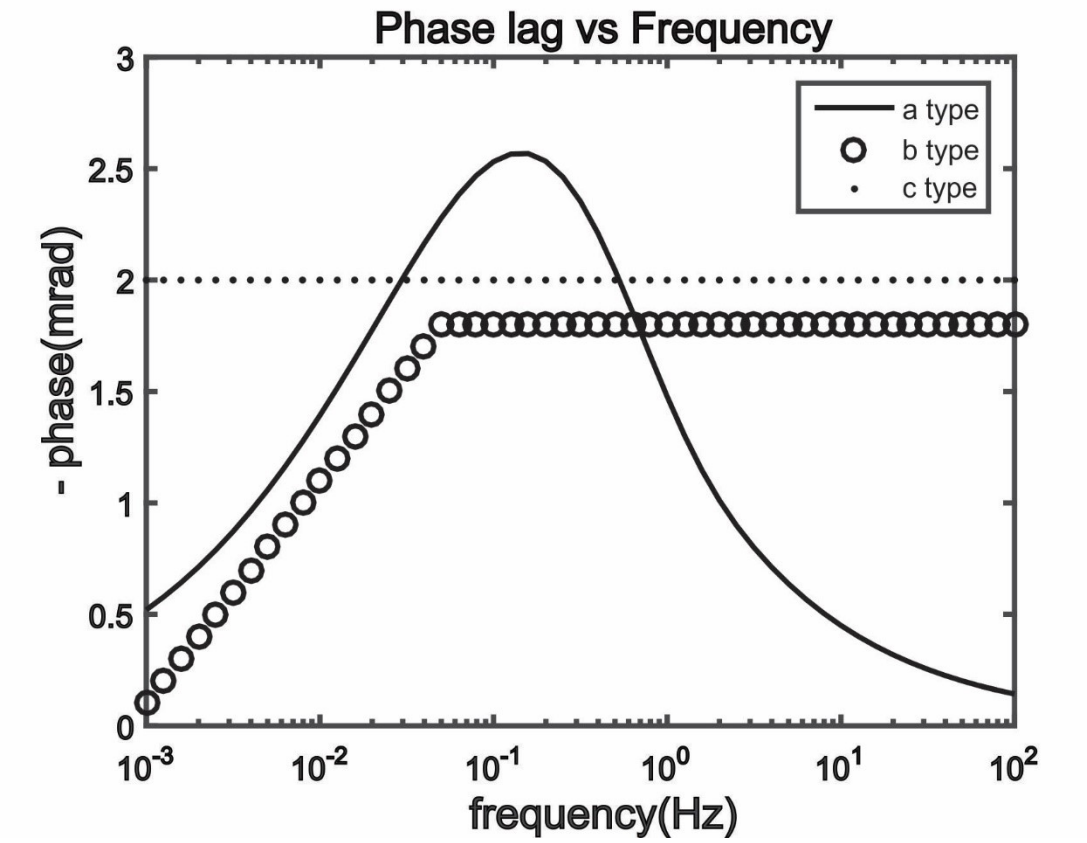

Figure 4.3- End member responses for different distribution of length scales. See text for details.

Type *a* response have a clearly defined peak frequency f_p and would be observed if only a single polarization, or a narrow closely spaced range of relaxation time distribution (RTD) exist in the material. This would be an ideal experimental response since the characteristic relaxation time τ_c can be easily found from frequency of the spectral peak.

Type *b* responses suggest the pore space is characterized by a broad distribution of length scales. The corresponding spectrum is essentially constant at higher frequencies but has a minimum

frequency threshold below which the phase lag decays to zero, this threshold would indicate the largest length scale. One might expect a similar maximum threshold for the smallest length scale existing in such a distribution but at the higher frequencies its effect is obscured by the further contributions to the phase lag from additional polarization processes that become more active. Type *b* responses have been observed (Lesmes and Frye, 2001) with some authors (Revil et al., 2015) suggesting that the corner frequency gives f_p and is indicative of the material's characteristic relaxation time τ_c. In that case it would be interpreted as the largest length scale over which polarisation occurs.

Finally, the type *c* response is indicative of a broad distribution of length scales such that the phase lag is almost constant across all frequencies; in the absence of any clear extremum or threshold finding a clear f_p indicative of a characteristic relaxation time is difficult or impossible.

Real phase lag spectra $\theta(\omega)$, or more precisely the $\rho''(\omega)$ as used below, *may* follow these illustrative cases or some combination of them. However, it is important to keep in mind that the functional goal of analysing the spectra in practical applications is to obtain an estimate of τ_c that can then be used to predict permeability. For this reason, we investigate use of a Debye decomposition as a possible way to standardize the estimation of characteristic relaxation times for permeability prediction.

4.2.4) Spectra Decomposition

For a single Debye-like relaxation associated with only one characteristic relaxation time τ_c, the frequency-dependent complex electrical resistivity $\rho^*(\omega)$ of a material would be (Nordsiek and Weller, 2008):

$$\rho^*(\omega) = \rho_0 \left(1 - M \left(1 - \frac{1}{1 + (i\omega\tau_c)^\alpha} \right) \right) \tag{4.9}$$

where ρ_0 is the DC resistivity, M is the chargeability, ω is angular frequency and α=1. Various empirical approaches for fitting data that do not conform to Eqn. 4.9 exist where $0 < \alpha < 1$ (e.g. Pelton et al., 1978). The corresponding $\rho'(\omega)$ and $\rho''(\omega)$ spectra for such a single Debye-like relaxation of Eqn. 4.9 are shown in Fig. 4.4 where the peak frequency f_p is clearly interpretable at the maxima of $\rho''(\omega)$. The essential idea behind Debye decomposition then is that a real observed spectrum consists of a linear superposition of numerous individual Debye spectra corresponding to a distribution of relaxation times and as weighted by their respective chargeabilities, as discussed in more detail later. Debye decomposition is a technique that has been standard practice for curve fitting of time-domain induced polarization data (Tarasov and Titov, 2007). Nordsiek and Weller (2008) assumed that their material could be characterized using a distribution of Debye-like relaxations instead of just one and introduced this fitting procedure as an alternative empirically based model (e.g. Lukichev, 2014).

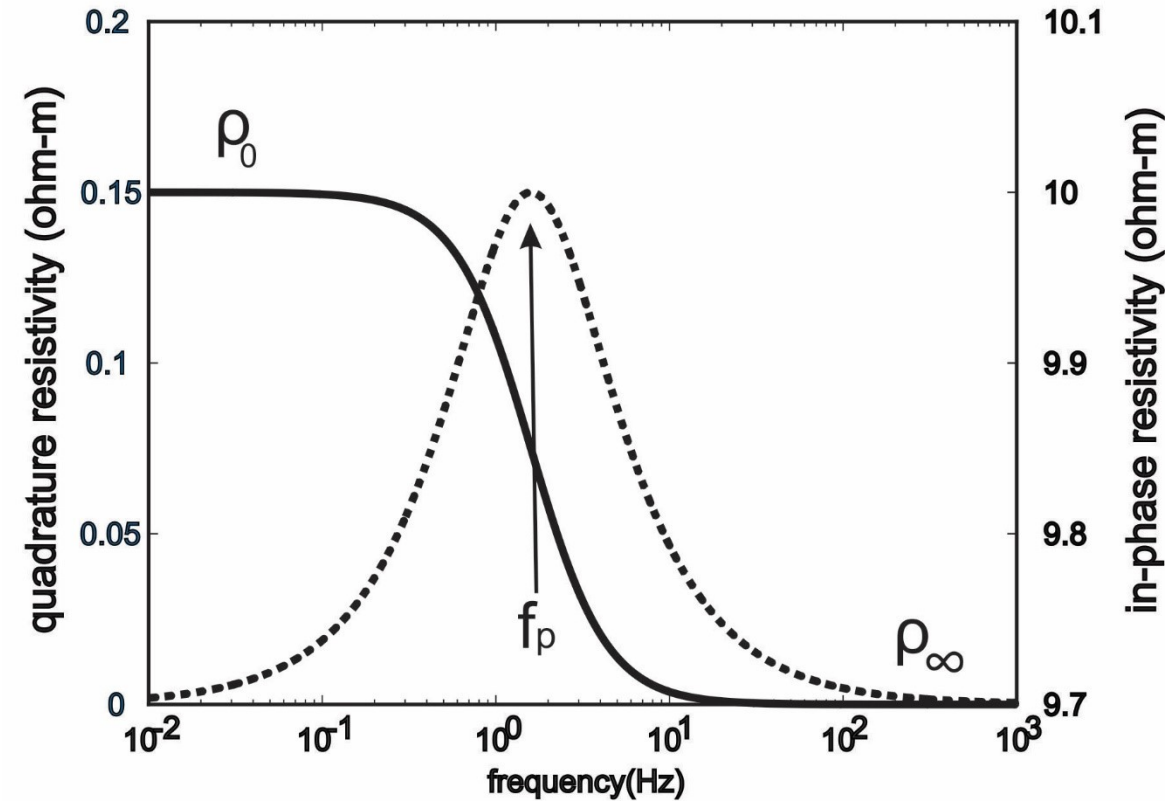

Figure 4.4. In-phase (solid line) and quadrature (dotted line) resistivity spectrum of a material with a single Debye characteristic relaxation time $\tau_c = 1/2\pi f_p$.

4.2.5) Previous work

Other workers have attempted to design experiments to shed light on the polarization mechanisms controlling electrical relaxation in sandy sediments. Klein and Sill (1982) conducted similar measurements on clay and glass bead mixtures with the goal of investigating how clay content and grain size affected characteristic relaxation times. They demonstrated that the glass bead size controlled the relaxation times but only did so for one clay type. They also showed an increase in relaxation time with increasing clay content going from 3% to 12% clay by weight.

Scott (2006) conducted an experiment on rock samples saturated with a viscous gel intending to increase the electrolyte viscosity to reduce the ionic mobility with the goal to assess the degree to which it influenced the polarization process. The characteristic frequency or relaxation times of the gel-saturated samples' complex conductivity did not vary with mobility leading the authors to conclude that membrane mechanisms do not significantly affect polarization. They reasoned that reduced ionic mobility leads to a longer time for charges to redistribute themselves once a charge imbalance is developed. However, they altered both the ionic mobility and the diffusion coefficient of the electrolyte (the two are related by the Einstein-Smoluchowski diffusion relation (Islam, 2004)). This affects both the accumulation of charge imbalances and diffusion of those charges under the induced concentration gradients. Additionally, they conceded that the effect of the gel very close to the pore wall is not known and the ionic strength of the gel cannot be determined. How exactly these different effects and properties of the gel compete against each other is not known. These uncertainties make it difficult to interpret their results. They do agree with the general consensus that this is a diffusion-controlled process but further experiments like those performed on a larger number of samples may prove insightful along with tests on the wettability of the gel on the different mineral surfaces in the rock. However, the fact that rocks must first be saturated with an electrolyte and then later with the gel is a major limiting factor for these types of experiments.

Weller et al. (2016) further investigated the relationship between induced polarization and pore radii by indirectly calculating diffusion coefficients for a database of rocks using a well-known relationship between pore radius and relaxation time (Schwarz,1962). Results suggested that either the pore throat radii are not the controlling length scale such that the actual length scale is much greater, or that the diffusion coefficient is highly variable depending on mineralogy (both may be

true as well). The latter is almost certainly true given that the mineralogy affects the properties of the electrical double layer (among which is the diffusion coefficient within the EDL) and the topology of the pore space which affects the bulk diffusion coefficient of the entire rock. The relevance of the former is still debated and is the main subject of this paper. Regardless, they did not find two distinct diffusion coefficients based on clay content as other authors have suggested (e.g., Revil, 2013), however the point that mineralogy affects the diffusion coefficient stands.

Joseph et al. (2016) in measurements on sieved sands found that the Cole-Cole (1941) relaxation times depend on the grain sizes in agreement with other numerous authors (e.g., Leroy et al., 2008; Titov et al., 2002). They did not, however, attempt to control the mineralogy of their samples and so isolating whether grain or membrane polarization governs the responses is difficult.

Breede et al. (2012) conducted SIP measurements on variably saturated sand and clay mixtures finding that the relaxation time decreased with decreasing saturation. They did not control for the effects of grain sizes in the sand but did vary the clay content. They suggest that their results are best explained by polarisation mechanisms in the pore space and not grain based models.

Okay et al. (2014) investigated the effect of clay content on SIP measurements on sand and clay mixtures to examine the effect of increasing clay content on the IP response. Their samples produced complicated spectra which was modelled based on a combined Stern layer polarisation model and a Donnan (1924) equilibrium model for the surfaces of clay and sand. Their model fit the higher frequency data well (> 0.1Hz) but it failed at lower frequencies. They concluded that that this failure was due to the presence of a membrane polarisation mechanism at low frequency. The complicated nature of their spectra made it difficult to distinguish whether grain sizes or surface areas affected relaxation times.

Leroy et al. (2008) reproduced the spectra observed on a glass beak packs saturated with NaCl electrolytes with conductivities of 5 mS/m by convolving the grain size distribution obtained from laser granulometry with the IP response of a single bead. Their model was based entirely on polarisation of the Stern layer.

With these issues in mind, here we attempt to use a variety of clays of differing surface charge densities and surface areas in mixtures with glass beads of different sizes in order both to isolate the factors controlling the observed polarisations and to identify the associated length scales.

4.3) Methods

In this section we give an overview of the experimental details including the specifics of the acquisition system and the samples used in this study. In the case of the acquisition system this includes the components as well as the design and testing of the system. For the samples this includes their contents and the manufacturing procedure.

Acquisition system

A simplified diagram of the 4-electrode experimental configuration and a diagram of its equivalent circuit is shown in Fig. 4.5. The system is activated with a constant AC current source (Keithly 6221) and the resultant voltages recorded using a lock-in-amplifier (Stanford Research Systems SR830). The current source sets the current's magnitude I_o and frequency f and communicates the input current phase to the amplifier as represented by the blue connection in Fig. 4.5a. Measurements were made for a range of frequencies between 10 mHz and 1 kHz for each sample. The use of a current source is advantageous in that it eliminates the need to measure signals across a shunt resistor minimizing the number of wires and connections required. The amplifier measures the RMS voltage V_o with 1% uncertainty and its phase lag θ relative to that for the known injected

current. The complex resistivities or conductivities may then be calculated following Eqns. 4.2 to 3.5. To avoid non-linear effects the current density was kept below 0.003 A/m^2.

Non-polarising Ag/AgCl electrodes are used for the potential electrodes to avoid polarisation effects. They are constructed using commercially available electrodes (3M™ Red Dot medical ECG electrodes) consisting of a 10 mm diameter Ag/AgCl pellet with a metal disk on top of the conductive gel in which the pellet sits. Both the metal disk and gel are removed before the electrode is attached to the measuring cell since exposure of the metal disk to the electrolyte during measurements would lead to polarisation. Each set of electrodes was used only once in order to avoid a reduction in measurement quality from one sample to another. To further reduce the risk of sample-electrode contact impedances, brine buffers containing the same electrolyte saturating the sample isolated the ends of the sample from the current electrodes.

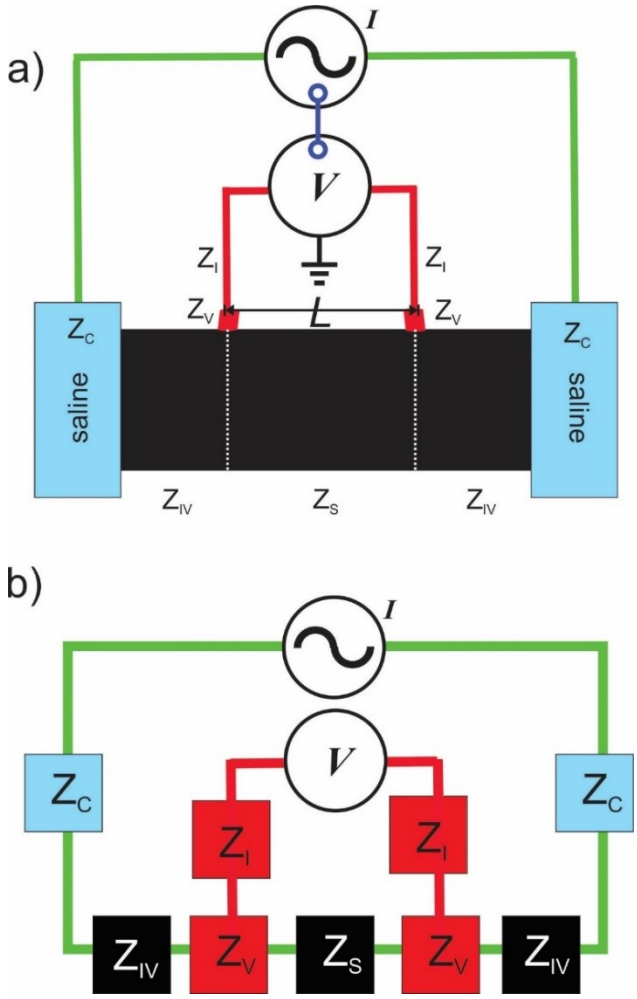

Figure 4.5. a) Simplified diagram of the experimental 4-electrode configuration with the sample (black) sandwiched between two saline buffers that inject current. The voltage difference is measured by a lock in amplifier between the two red electrodes separated a distance *L* axially along the sample. . The constant current source is connected to the lock in amplifier to provide phase references. The various impedances that need to be considered include those for the current electrodes including the saline buffer Z_C, the lock-in-amplifier Z_I, the voltage electrodes Z_V. the portions of the sample between the saline buffers and the voltage electrodes Z_{IV}, and the desired sample impedance Z_S. b) Simplified equivalent circuit showing the arrangement of the expected impedances in the system.

To understand the importance of eliminating contact impedances it is necessary to consider the equivalent circuit of a rock during the 4-electrode measurement technique, a complete and general review of which can be found in Zimmermann et al. (2008). Bona et al. (2008) gives a simpler analysis in which common electrodes (either potential or voltage) are assumed to have the same contact impedance. The equivalent circuit of Bona et al (2008) for the 4-electrode system is shown in Fig 4.5b where Z_c is the contact impedance of the current electrode, Z_{IV} is the impedance of the portion of the sample lying between current and voltage electrodes, Z_v is the contact impedance of the voltage electrodes, Z_s is the sample impedance, and Z_I is the input impedance of the signal analyser or amplifier. For the simplified case of Fig. 4.5b the impedance Z_m actually measured is:

$$Z_m = Z_s\left(1 + \frac{Z_c + Z_v + Z_{IV}}{Z_I}\right) \tag{4.10}$$

which makes apparent that the larger the input impedance Z_I of the signal analyser, the closer the measured value is to the actual desired sample impedance Z_s. The input impedance of the lock-in amplifier is 10 MΩ which is sufficient in the measurement of the relatively conductive samples used here.

The stated phase accuracy for the lock-in amplifier of +/-0.01 degrees from the manufacturer's specifications (~0.17 mrad). However, at frequencies above 100 Hz the observed phase lags exceed these accuracies, and they deviate rapidly from the lower-frequency trend apparent in the phase spectrum observed for weak test electrolytes made by adding small amounts of NaCl to distilled water (Fig. 4.6). The conductivities for these test electrolytes were 0.09 and 0.03 S/m. Ideally, for pure water no dispersion is expected at frequencies below 10 kHz This problem is believed to stem from contact impedances of the voltage electrodes, similar to behaviours seen by Huisman et al (2014) for both metallic and non-polarising electrodes. Above 100 Hz, this phase

error is also larger for the more resistive sample (Fig. 4.6) meaning that phase errors greater than 10 mrad are expected at the higher frequencies.

Conversely, instrumental drift was a concern for frequencies below 0.1Hz. That said this drift never exceeded 1 mrad.

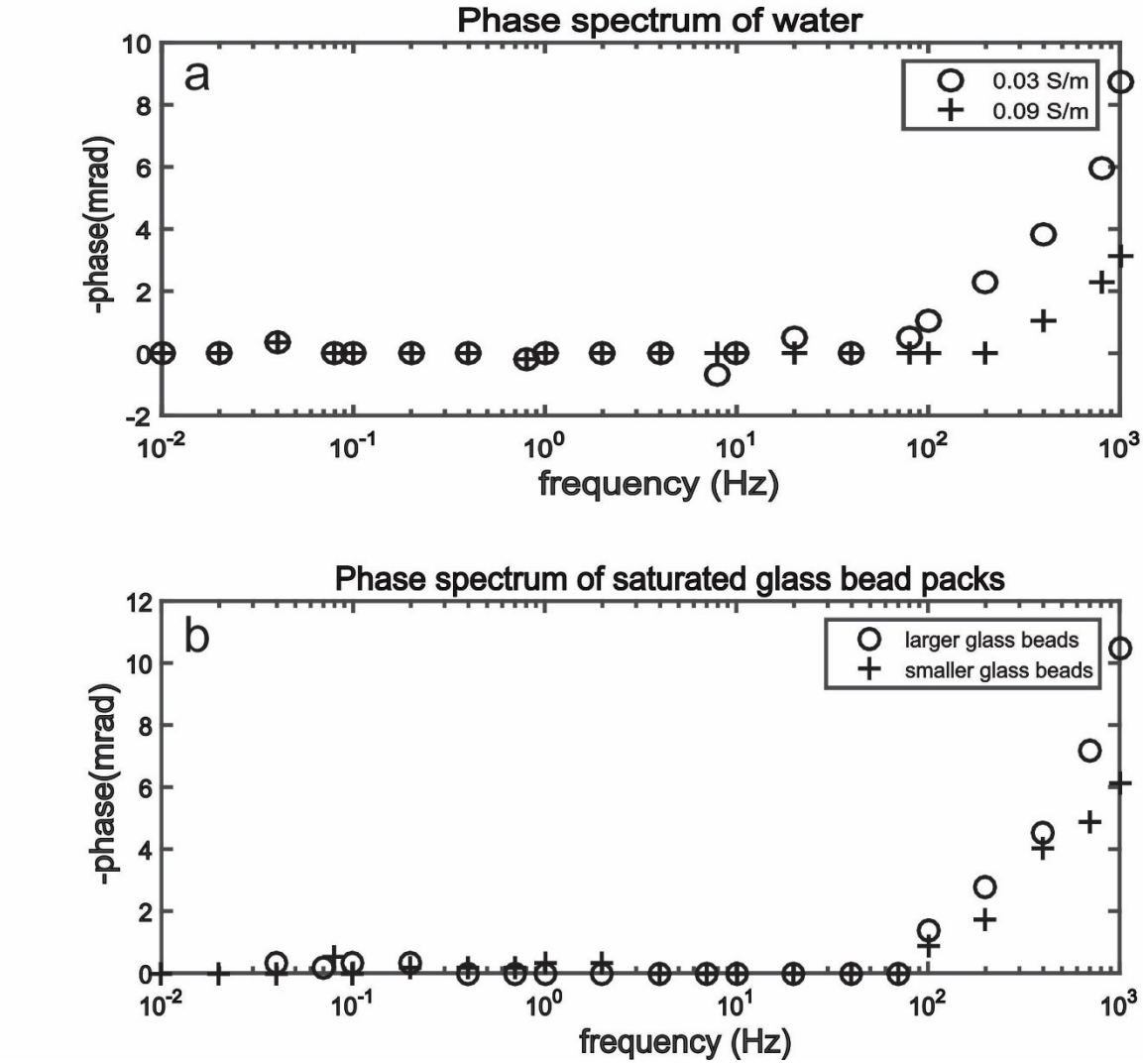

Figure 4.6. (a) Phase spectrum for two water samples with different conductivities. (b) Phase spectra of clay-free glass bead packs.

4.3.1) Sample construction

The commercially available glass beads, typically used for sand-blasting, came in a large #1 (0.420 - 0.841 mm) and small #2 (0.074 - 0.125 mm) distributions of diameters. Previous work (Bouzidi, 2003) indicated that each set may contain some beads smaller than that specified by the manufacturer. SIP measurements were made with glass beads that were either washed or not with deionized water, this washing did not seem to be critical as identical responses were seen. The complex conductivity measured on "clean" samples consisting of only packed glass beads did not display any significant polarization below 100 Hz (Fig. 4.6b). This behaviour contrasts with that seen later for the "dirty" samples containing clay. Consequently, the glass beads may be referred to as "passive grains" while the clay minerals are called "active grains" to emphasize the role each plays in obtaining a non-zero quadrature conductivity. Active grains are those which are primarily responsible for the observed response while passive grains are those which do to contribute to the observed phase lags.

The dried clays employed originated from quarries in the Late Cretaceous Ravenscrag and Whitemud Formations of southern Saskatchewan. The four samples, provided by Plainsman Clay Ltd, Alberta, are primarily intended for ceramic manufacturing. These samples were characterized using a variety of methods (Table 4.1). The minerals contained in each sample were detected by standard XRD in the Dept. of Earth and Atmospheric Sciences at the University of Alberta. Quantitative modal analysis was not conducted. Cation exchange capacity (CEC), which describes the total number of cations that can be adsorbed to the surface of a material per unit mass, was provided by routine agronomy measurements at the Natural Resources Analytical Laboratory at the University of Alberta. The specific surface areas of the sample were obtained using an Autosorb automated gas sorption analyser with nitrogen as the adsorbent gas as interpreted using

Brunauer, Emmett and Teller (BET) theory (Brunauer et al.,1938). Measurements were performed at the National Institute for Nano Technology (NINT).

The electrolytes were prepared by adding laboratory grade NaCl (Fisher Scientific) to distilled water. The NaCl concentrations for electrolytes that were finally used in the experiments were determined by trial and error because if the electrolyte conductivity is too high then little or no phase lag across the spectrum can be observed. An electrolyte conductivity of ~0.02 S/m was found to reliably produce observable phase lags for all of the samples. The electrolytes were prepared by mixing small amounts of reagent grade NaCl into the distilled water until this desired conductivity was reached. This electrolyte was then sealed in a container for later use. The electrolyte's conductivity was retested immediately before use to ensure that it had not changed.

Bairlein et al. (2014) suggest four methods of sample preparation when forming their mixtures of natural quartz sands and clays into unconsolidated sediment samples for their SIP measurements; and we built on their efforts by combining elements of each as well as from our own experience. First, the glass beads and clay were wetted and mixed by hand in a small container (separate from the eventual sample holder) with the saturating electrolyte; we found that this ensured a more homogeneous distribution of clay and reduced the variations in clay distribution between samples, an example of the microscopic structure of a typical sample (Fig. 4.7) shows a uniform distribution of clay throughout. The material was then loaded into the cylindrical 3.52 cm diameter, ~10 cm length PVC sample holder and the electrolyte was added as necessary to ensure that the sample would be completely saturated. While material was being added, the sample holder was tapped to facilitate compaction and the mixture and was stirred occasionally as new material was added. The material was gently compressed with a plunger. The sample holder was then sealed at both ends with filter paper.

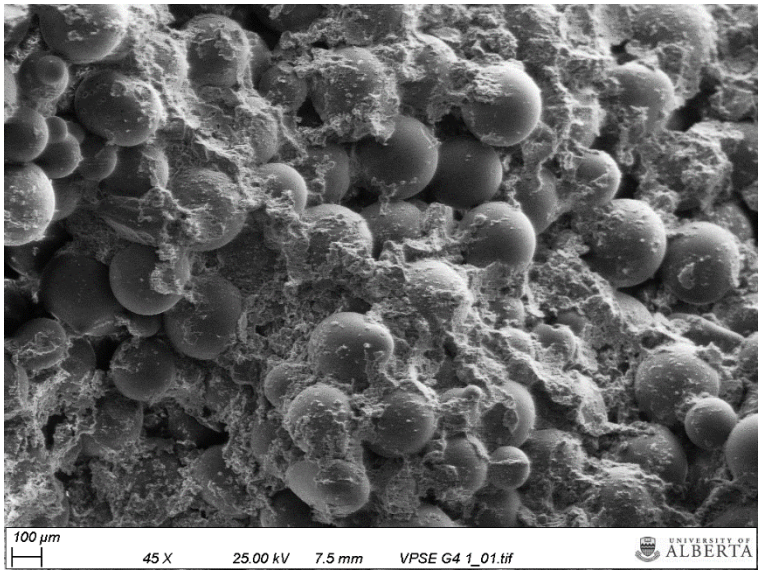

Figure 4.7. SEM image of a sample constructed using a mixture of glass beads with varying sizes and 10% clay by weight.

The properties of the four clays used are summarised in Table 4.1. The clays used were selected to provide distinct ranges of cation exchange capacities (CEC) and specific surface areas (SSA). The four clays combined with 2 sets of glass beads to give 8 samples (samples S1-S8) that were all 8% clay by weight. These were the samples used to study what controls the occurrence of a peak frequency. Clay #2 differs from the others in that it is the only one that contained nontronite, a swelling clay within the montmorillonite family. This made Clay #2 distinctive in terms of its CEC and SSA.

Table 4.1. Characteristics of clay samples employed

Clay #	Cation Exchange Capacity CEC - cmol/kg	Specific Surface Area SSA - m^2/g	Effective Surface Charge Density Q_S cmol/m^2 x 10^3	XRD minerals present
Clay 1	7.56	11.19	0.676	Qz[a], Ms[b], Sa[c]
Clay 2	24.50	32.60	0.752	Qz[a], Kln[d], Ilt[e], non[f]
Clay 3	8.87	14.88	0.596	Qz[a], Kln[d], Ms[b]
Clay 4	4.83	4.80	1.01	Kln[d], Qz[a], Ms[b], Mc[g]

[a]quartz, [b]muscovite, [c]sanidine, [d]kaolinite, [e]illite, [f]nontronite, [g]microcline

Table 4.2 provides the petrophysical properties of the samples. Porosities were obtained using simple mass differences together with the known internal volume V_s of the sample holder. The mass of the saturated sample mixture M_t was determined as the difference of the measured masses of the holder when filled with the mixture and the holder's mass. Upon completion of the measurements, the sample's sediments were removed from their PVC sample holder and then slowly air dried under ambient conditions in the laboratory. This mass was repeatedly measured during this drying period until no further changes was found and this final value gave the solid mass M_s. The porosity is then simply

$$\varphi = \frac{(M_t - M_s)}{V_s \rho_f} \tag{4.11}$$

where ρ_f is the density of the electrolyte. To ensure that this method was appropriate, in two of these cases the sample sediments were further dried in an oven at ~ 70˚C for an additional 24 hours, and no change in mass was measured. Repeatedly repacking the sample and drying suggests that the error in the porosity was less than $\pm$2% porosity.

Table 4.2. Summary table for samples measured in this work. Glass beads diameter ranges are 0.420 - 0.841 mm for #1, 0.074 - 0.125 mm for #2.

Sample#	Glass beads used	Clay used (weight percent during packing)	Porosity (%) (+/- 2%)
S1	#1	Clay 3(8%)	30
S2	#2	Clay 3(8%)	34
S3	#1	Clay 2(8%)	29
S4	#2	Clay 2(8%)	35
S5	#1	Clay 1(8%)	32
S6	#2	Clay 1(8%)	-
S7	#1	Clay 4(8%)	30
S8	#2	Clay 4 (8%)	36

Ideally, we would have obtained measurements of each sample's formation factors, *F,* and surface conductivities. However, this was not possible as on the basis of experience we were unable to replace the saturating electrolyte with second one with differing conductivity without considerably altering the clay distribution.

The pH of selected samples was measured after electrical measurements were completed using Fischer scientific litmus paper. Additionally, the pH of water with the different mixtures in it was monitored of 2 days. All of the measurements showed pH's between 6 and 7.

4.3.2) Debye Decomposition

As mentioned earlier, Debye decomposition is a technique for fitting SIP spectra to obtain distributions of relaxation times. The utility of this is that average relaxation times (or a dominant

relaxation time) can then be used for permeability prediction assuming knowledge of grain or pore sizes. The decomposition presumes that the observed spectrum is described by a superposition of the appropriately weighted Debye curves associated with N relaxation times τ_k, and chargeabilities M_k.

$$\rho^*(\omega) = \rho_0 \left(1 - \sum_{k=1}^{N} M_k \left(1 - \frac{1}{1 + i\omega\tau_k} \right) \right) \tag{4.12}$$

Given that the functional goal of Debye decomposition is to ultimately obtain a single representative relaxation time that can then be used to predict permeability, it is worthwhile to consider how that relaxation times are determined. Different estimates of the relaxation times or their distributions will depend on:

1. The decomposition procedure employed and whether it assumes a discrete or a continuous RTD and,

2. the selection criterion (e.g. mean or maximum chargeability) and the range of frequencies used for the determination.

Here, we test these various methodologies to determine the relaxation times or their distributions using the complex conductivities measured in the laboratory. It is worthwhile to review the different approaches that have been applied in determining RTD.

Nordsiek and Weller (2008) method, modified slightly by Zisser et al. (2010), assumes a continuous distribution of relaxation times on the full recorded spectrum. They estimate a mean relaxation time ($\bar{\tau}$) and take every measured frequency into account.

$$\bar{\tau} = e^{\frac{\sum_k M_k \ln(\tau_k)}{\sum_k M_k}} \tag{4.13}$$

This approach involves a linear transformation of the measured data according to

$$\rho^*_{norm}(\omega) = \frac{\rho_0 - \rho^*(\omega)}{\rho_0} \tag{4.14}$$

with real

$$\rho'_{norm}(\omega) = \sum_{k=1}^{n} M_k * (\omega\tau_k)^2 * (1 + (\omega\tau_k)^2)^{-1} \tag{4.15a}$$

and imaginary parts

$$\rho''_{norm}(\omega) = \sum_{k=1}^{n} M_k * (\omega\tau_k) * (1 + (\omega\tau_k)^2)^{-1} \tag{4.15b}$$

giving a system of linear equations which can be inverted via a non-negative least square fitting routine.

$$\begin{pmatrix} \frac{(\omega_1\tau_1)^2}{1+(\omega_1\tau_1)^2} & \cdots & \frac{(\omega_1\tau_n)^2}{1+(\omega_1\tau_n)^2} \\ \vdots & \ddots & \vdots \\ \frac{(\omega_p\tau_1)^2}{1+(\omega_p\tau_1)^2} & \cdots & \frac{(\omega_p\tau_n)^2}{1+(\omega_p\tau_n)^2} \\ w\frac{(\omega_1\tau_1)}{1+(\omega_1\tau_1)^2} & \cdots & w\frac{(\omega_1\tau_n)}{1+(\omega_1\tau_n)^2} \\ \vdots & \ddots & \vdots \\ w\frac{(\omega_p\tau_1)}{1+(\omega_p\tau_1)^2} & \cdots & w\frac{(\omega_p\tau_n)}{1+(\omega_p\tau_n)^2} \end{pmatrix} * \begin{pmatrix} M_1 \\ \vdots \\ M_n \end{pmatrix} = \begin{pmatrix} \rho'_{norm}(\omega_1) \\ \vdots \\ \rho'_{norm}(\omega_p) \\ w\rho''_{norm}(\omega_1) \\ \vdots \\ w\rho''_{norm}(\omega_p) \end{pmatrix} \tag{4.16}$$

where

$$w = s\frac{\sum_{k=1}^{p}\rho'}{\sum_{k=1}^{p}\rho''}.$$

The difference between the inversions performed by Nordsiek and Weller (2008) and Zisser et al (2010) is simply a weighting factor *w* that allows for the misfit function to reliably fit both the real and imaginary data at the same time since they differ by orders of magnitude. The constant *s* in the expression for the weighting factors in Eqn. 4.16 was typically assigned a value of 1 but for some of the samples values between 0.6 and 3 were used (note *s* is simply a scaling factor).

We initially used the method of Zisser et al. (2010) to estimate the true DC resistivity ρ_o although the observed in-phase value at the lowest recorded frequency allowed for a better final fit. Florsch et al. (2014) alternatively proposed to use a Warburg decomposition model that they compared against a Debye decomposition. The Warburg model is simply an end-member (Cole-Cole parameter $\alpha = ½$) Cole-Cole distribution (Cole and Cole 1941), which is a modification of the Debye distribution. Their procedure assumes a continuous distribution of relaxation times. In their approach they compute the response of a single relaxation time and deconvolve it from the complex conductivity spectrum to obtain the relaxation time distribution. The Debye decomposition performs similarly to the Warburg decomposition but they recommend the Warburg distribution since it gives a distribution that is more compatible with pore throat size distributions obtained from mercury porosimetry.

Ustra et al. (2016) suggested a slightly different method in which a minimum number of relaxation times are used to fit the observed spectra. This represents a discrete distribution of relaxation times where the probability distribution function (pdf) is given by a series of weighted Dirac-δ. Whether or not the distribution is discrete or continuous is open for debate but the distinction is likely arbitrary as a good fit can be obtained with either method.

We attempted a few different fitting procedures, including one that implemented a high-order least-squares regularization scheme. The differences in the results of the fitting procedures will be

discussed later but all of the relaxation times presented below were obtained using, essentially, the method of Zisser et al. (2010). We supply the algorithm with $N = 1000$ relaxation times distributed equally over the frequency range measured. We then invert for the corresponding chargeabilities with the physical constraint that they be positive.

For purposes of comparative assessment, each sample's characteristic relaxation time τ_c was determined using two different criteria for determining τ_c. In the first, a peak or a corner frequency was hand-picked from the quadrature spectre (τ_{hp}) following Revil et al's (2015) guidelines; a polynomial is fit to the data and the maximum of that function is chosen as the peak frequency. Alternatively, the frequency with the highest recorded phase lag can be used but this may lead to errors due to under-sampling.

These are compared with estimates of the mean relaxation times calculated (Eqn. 4.13) from the RTD obtained by fitting simultaneously the in-phase $\rho'(\omega)$ and quadrature $\rho''(\omega)$. It is important to note that only those values of the in-phase or quadrature resistivities at frequencies below 100 Hz were used in order to avoid nonelectrochemical relaxation processes, such as Maxwell-Wagner and spurious experimental electrode polarizations (Fig. 4.6). Fortunately, this lower frequency range of 0.01-100 Hz is most applicable to field measurements (Slater and Lesmes, 2002).

4.4) Results

Before looking at the results of the Debye decomposition, it is useful to examine some of the data in a Cole-Cole diagram. This diagram plots the real and imaginary data against each other. Materials which exhibit a single Debye type relaxation time plot as a semicircle with the 2 x-intercepts giving the high and low frequency cut-offs for the real part of the resistivity. Sample S5 which exhibits the most Debye like spectrum, can be seen in Fig. 4.8 along with a Debye

model and Cole-Cole model. The Cole-Cole model is a variant of Eqn. 4.9 where α is an adjustable parameter meant to account for materials with a distribution of relaxation times as opposed to one. Fig. 4.8 shows a Cole-Cole model with $\alpha = .7$. Minimum and maximum resistivities for both models were adjusted to fit the data. Although the Cole-Cole diagram provides a somewhat satisfactory fit, it is apparent that a single relaxation time does not describe the material and the remaining data is poorly fit by either model. This provides further justification for the use of multiple Debye relaxation times to describe the samples.

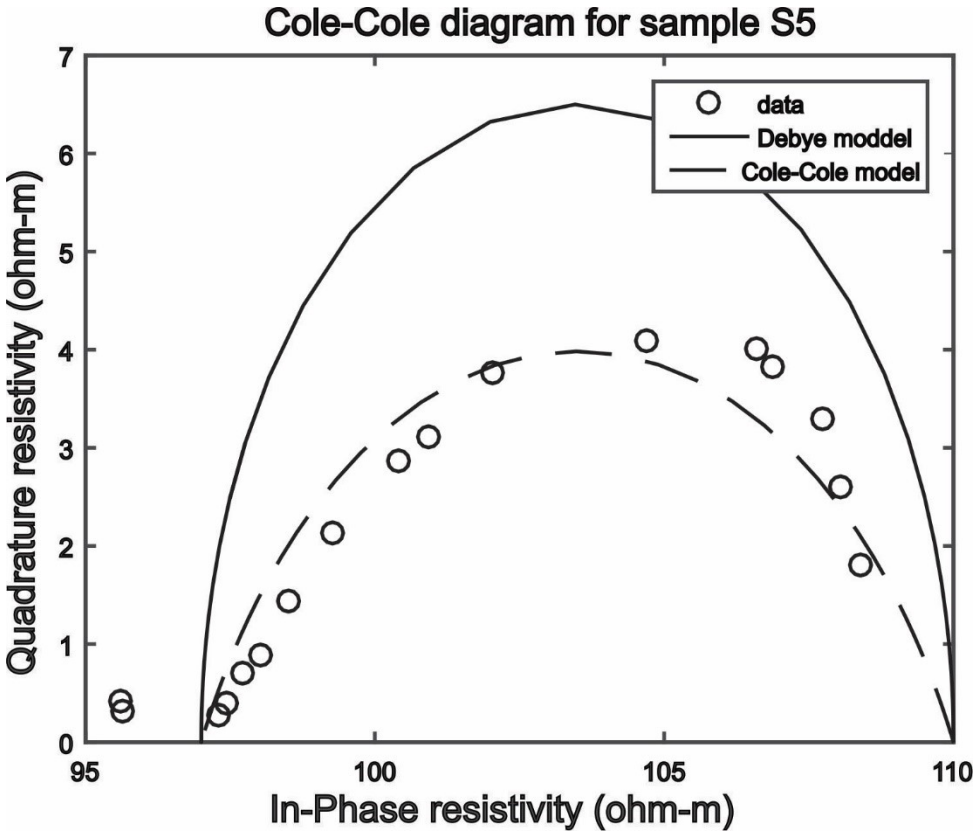

Figure 4.8- Cole-Cole diagram for sample S5 showing Debye and Cole-Cole models for comparison.

The complex resistivity spectra obtained from inverting the entire dataset below 100 Hz for samples S1-S8 (Figs. 4.9-4.12) exhibit either Type *a* (clear peak) or Type *b* (corner frequency)

responses. As mentioned earlier, a peak frequency f_p is interpreted to mean that there is a dominant polarization length scale, while a corner frequency indicates the largest polarization length scale within a distribution. The best-fit Debye decompositions are shown in Figs. 4.9-4.12 as histograms of the chargeability vs relaxation time. For most of the samples, the characteristic frequency is interpreted from a clear peak in the quadrature spectrum. The fit qualities do vary, however. In particular, samples S1 and S2 exhibit more complicated spectra (Fig. 4.11) where determining a corner frequency is difficult. Identifying the corner frequency in sample S2 was the most problematic; and the inflection point at which the quadrature spectrum rapidly tends to zero was chosen. One notable result from the Debye decompositions is that the inversions tend to produce discrete relaxation times similar to those discussed in Ustra et al (2016). Regularization (1st order Tikhonov regularization) produced more continuous RTDs but did not greatly affect the mean relaxation times which are the important parameter gained from the inversion; as this approach did not improve the analysis it was abandoned. Figs. 4.9-4.12 also show that the resistivity varied from sample to sample. The small difference in salinity of the electrolytes used for some samples accounts for some of this but it is mostly due to the different surface conductivities for the different samples (relevant to note that salinity in turn affects surface conductivity). Samples with smaller glass beads had significantly higher surface conductivities and thus have lower resistivities.

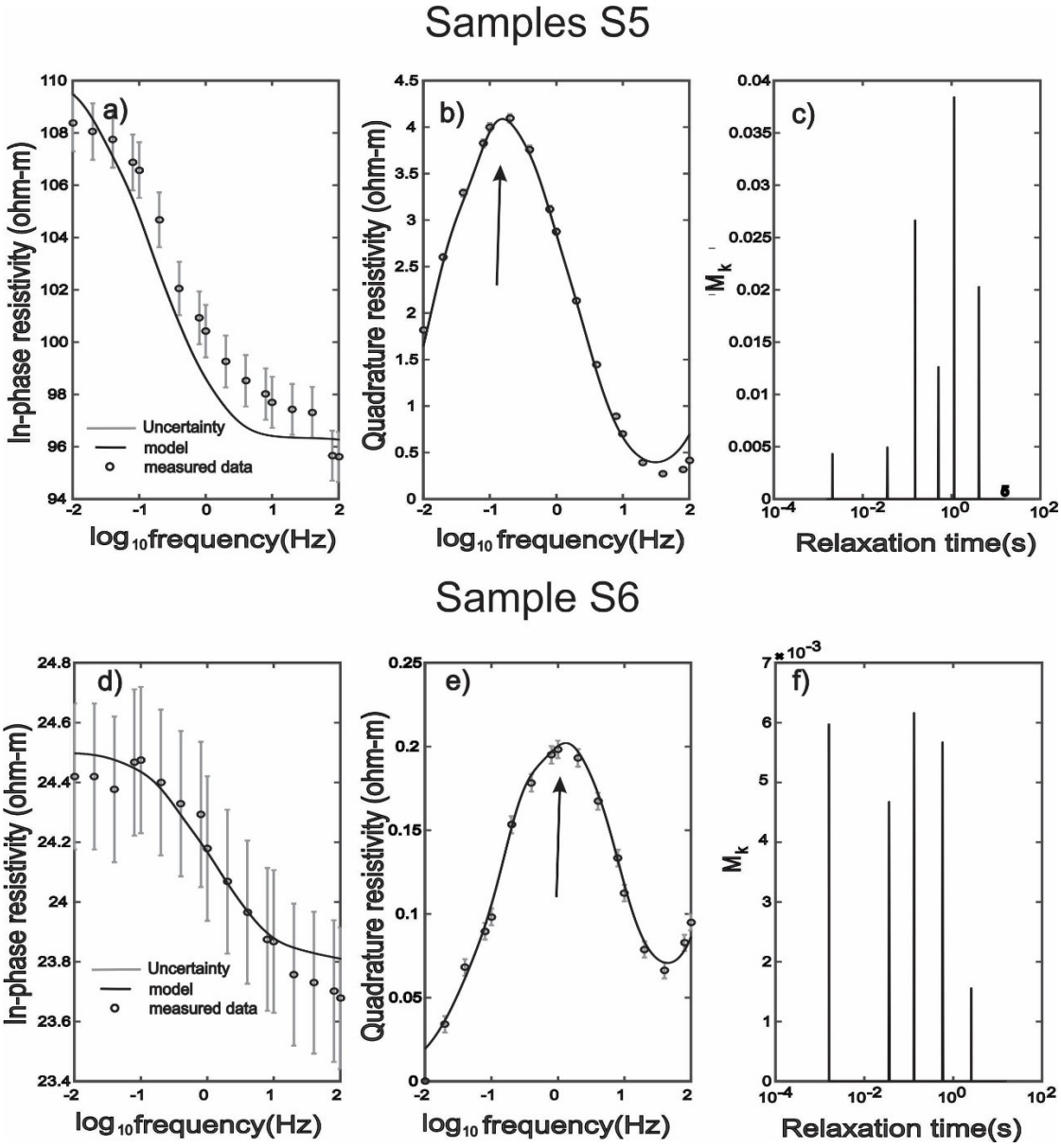

Figure 4.9. Data and Debye decomposition result for samples incorporating clay 1. (a) In-phase resistivity spectrum for sample using larger glass beads. (b) Quadrature resistivity spectrum for sample using larger glass beads. (c) Relaxation time distribution for sample using larger glass beads. (d) In-phase resistivity spectrum for sample using smaller glass beads. (e) Quadrature resistivity spectrum for sample using smaller glass beads. (f) Relaxation time distribution for sample using smaller glass beads. Arrow indicates the location of the "hand picked" characteristic frequency.

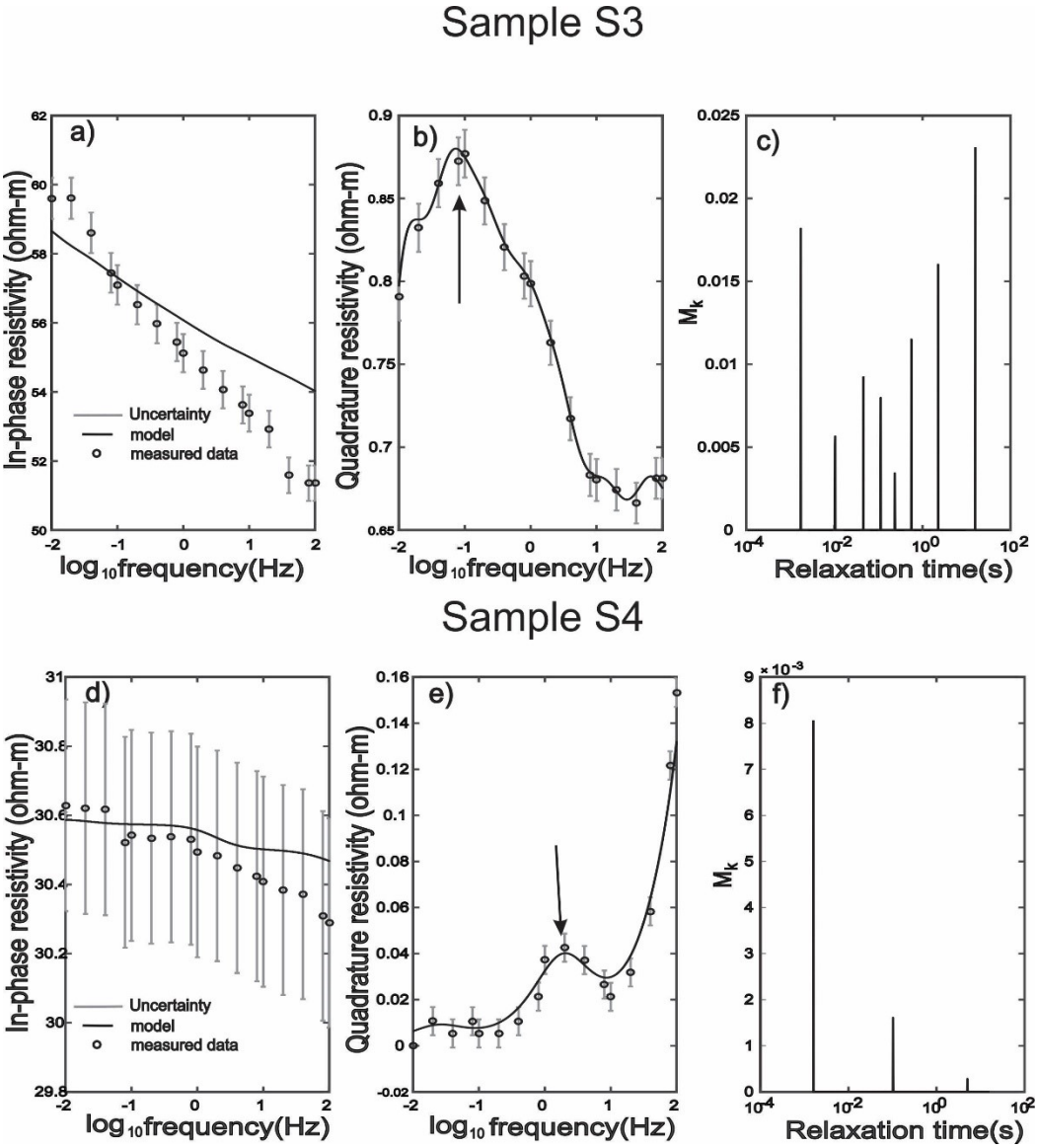

Figure 4.10. Data and Debye decomposition result for samples incorporating clay 2 (a) In-phase resistivity spectrum for sample using larger glass beads. (b) Quadrature resistivity spectrum for sample using larger glass beads. (c) Relaxation time distribution for sample using larger glass beads. (d) In-phase resistivity spectrum for sample using smaller glass beads. (e) Quadrature resistivity spectrum for sample using smaller glass beads. (f) Relaxation time distribution for sample using smaller glass beads. Arrow indicates the location of the "hand picked" characteristic frequency.

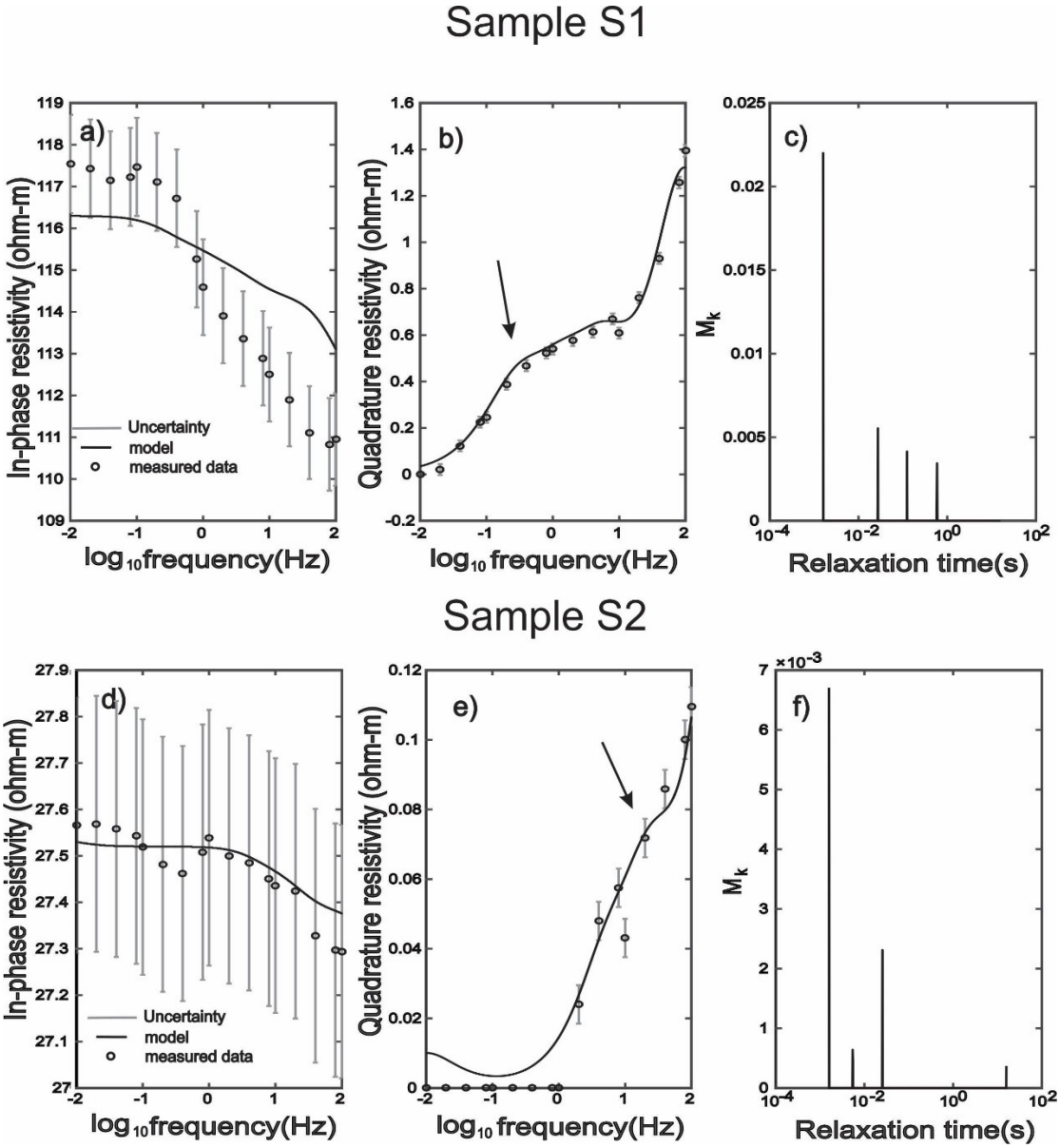

Figure 4.11. Data and Debye decomposition result for samples incorporating clay 3. (a) In-phase resistivity spectrum for sample using larger glass beads. (b) Quadrature resistivity spectrum for sample using larger glass beads. (c) Relaxation time distribution for sample using larger glass beads. (d) In-phase resistivity spectrum for sample using smaller glass beads. (e) Quadrature resistivity spectrum for sample using smaller glass beads. (f) Relaxation time distribution for sample using smaller glass beads. Arrow indicates the location of the "hand picked" characteristic frequency.

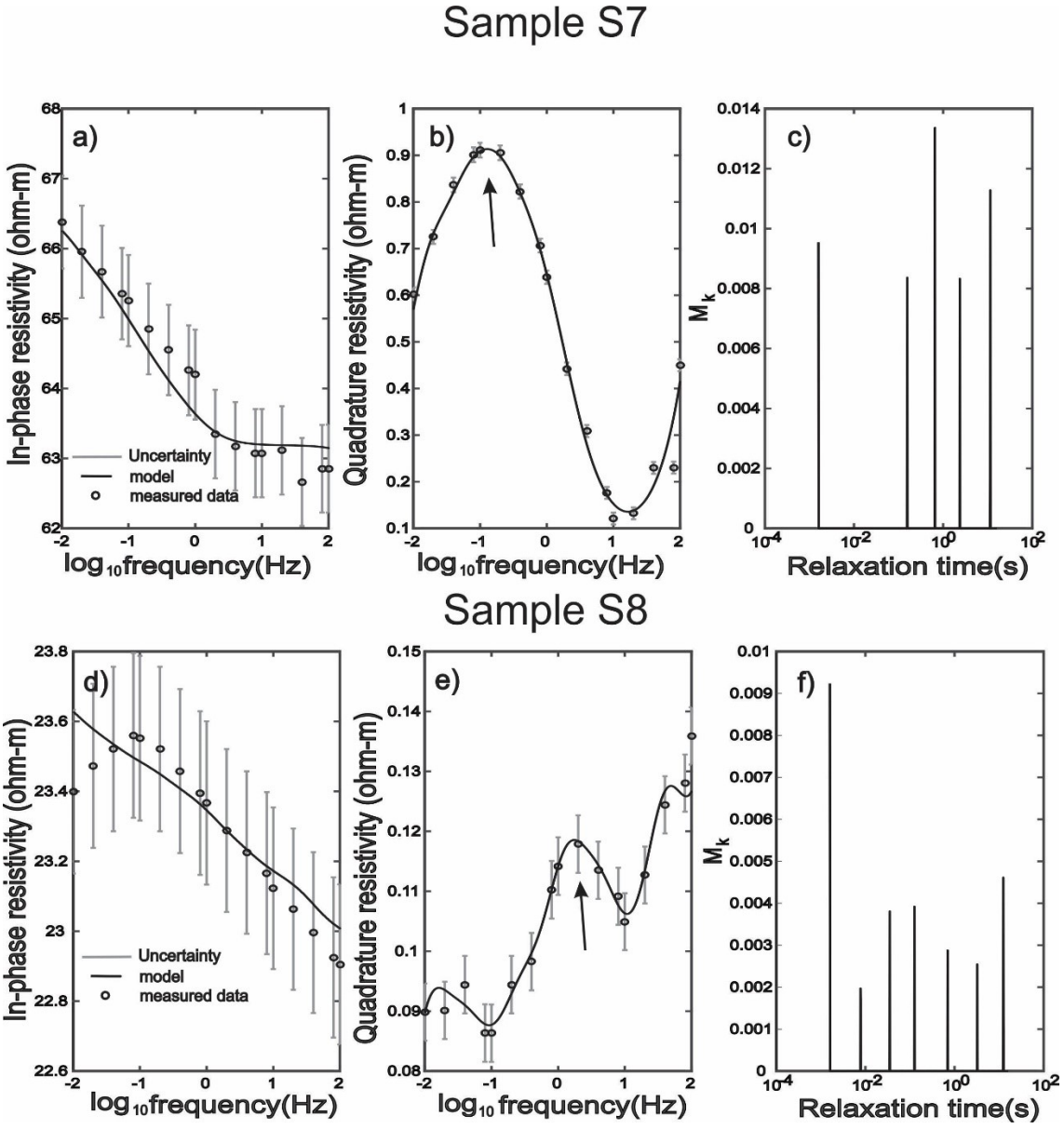

Figure 4.12. Data and debye decomposition result for samples incorporating clay 4. (a) In-phase resistivity spectrum for sample using larger glass beads. (b) Quadrature resistivity spectrum for sample using larger glass beads. (c) Relaxation time distribution for sample using larger glass beads. (d) In-phase resistivity spectrum for sample using smaller glass beads. (e) Quadrature resistivity spectrum for sample using smaller glass beads. (f) Relaxation time distribution for sample using smaller glass beads. Arrow indicates the location of the "hand picked" characteristic frequency.

Table 4.3. Summary of the relaxation times obtained from hand picking and from fitting real and imaginary spectra.

Sample	τ_{hp}(s)	τ_b(s)
S1	1.81	0.0154
S2	0.0316	0.00851
S3	2.14	0.211
S4	0.0784	0.00641
S5	1.01	0.471
S6	0.131	0.0766
S7	1.18	0.615
S8	0.09	0.0871

The obtained relaxation times are summarized in Table 4.3. The mean relaxation times calculated applying Eqn. 4.13 to the RTD obtained from the Debye decomposition were generally lower than those determined from direct hand picking of a peak or a corner frequency. Further, the smaller bead samples generally have shorter relaxation times than their coarse-grained counterpart (Fig. 4.13). Overlap in the relaxation times between the small and large bead samples comes from samples S1 and S2 for which the relaxation times determined by hand-picking of a corner frequency are most discrepant with those calculated from the RTD. If only considering samples with a clear peak frequency response, the trend from the "handpicked" values that shows a clear division in relaxation time based on glass bead size remains. Fig. 4.14 shows the ratios of relaxation times for pairs of samples with the same clay type ($Ratio = \frac{Relaxtion\ time\ for\ corse\ grained\ sample}{Relaxation\ time\ for\ fine\ grained\ sample}$). This result makes it apparent that hand picking resulted in the most similarity between estimates. Fig. 4.15 shows no apparent trends between specific surface area and relaxation times for any picking method.

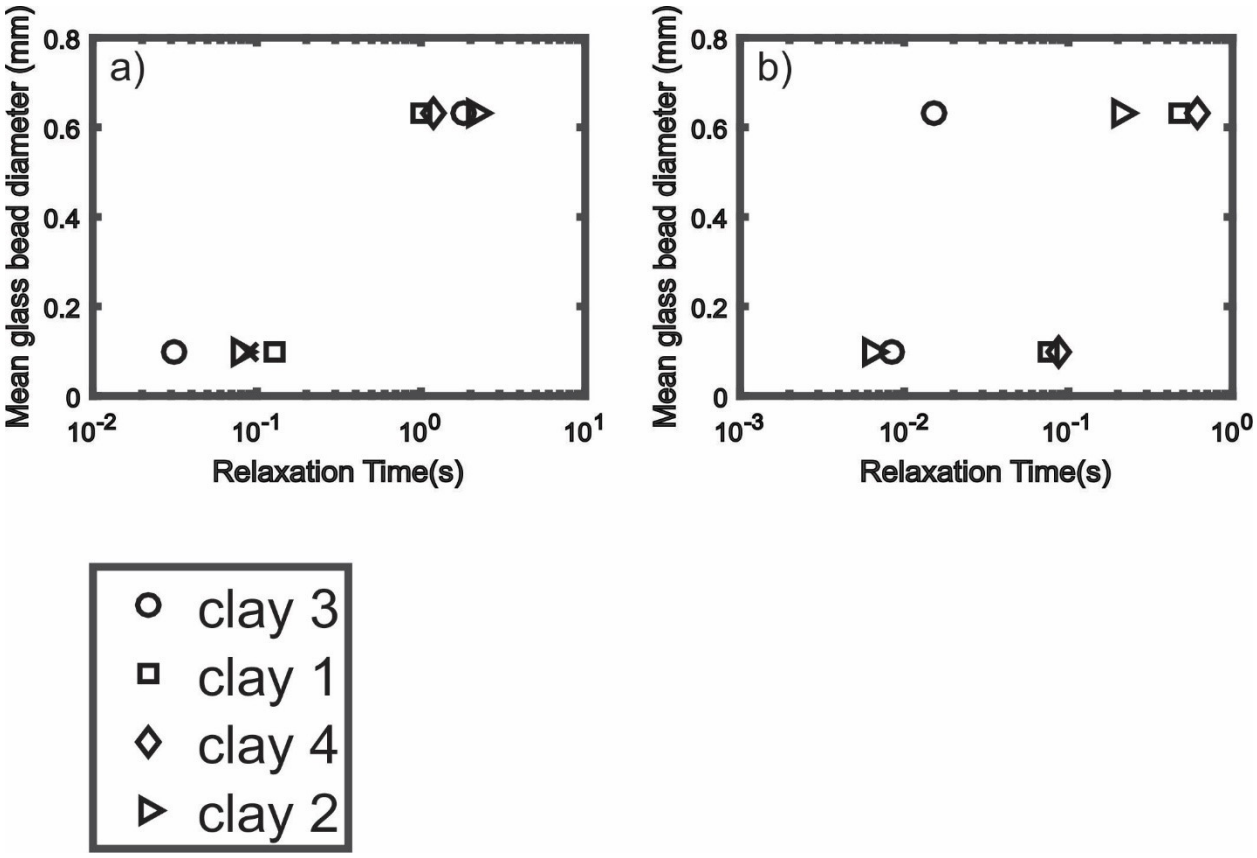

Figure 4.13. Comparison of relaxation times estimated using different inversions of the complex resistivity versus mean glass bead diameter by (a) hand picking and (b) Debye decomposition of the in-phase and quadrature resistivity spectrum.

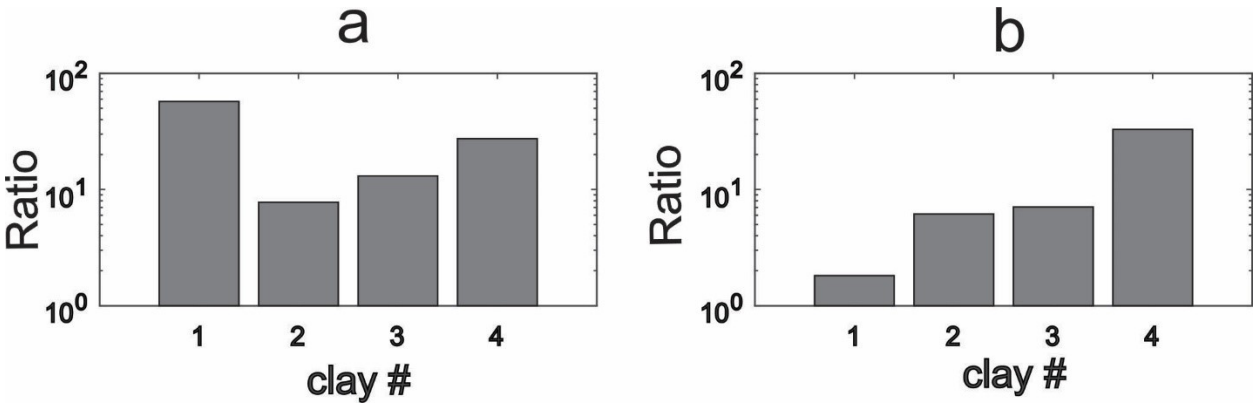

Figure 4.14. Ratio of relaxation times for samples with the same clay type but different glass bead sizes for (a) hand picked values and (b) fitting both real and imaginary spectra.

Fig. 4.15 shows the relaxation times as estimated by the different methods as a function of the clay specific surface area. Both show no clear relationship to the specific surface area of the clay. This is not an obvious result because despite the fact that the observed responses require clay be incorporated to the mix, the relaxation times appear to depend on the glass bead dimensions.

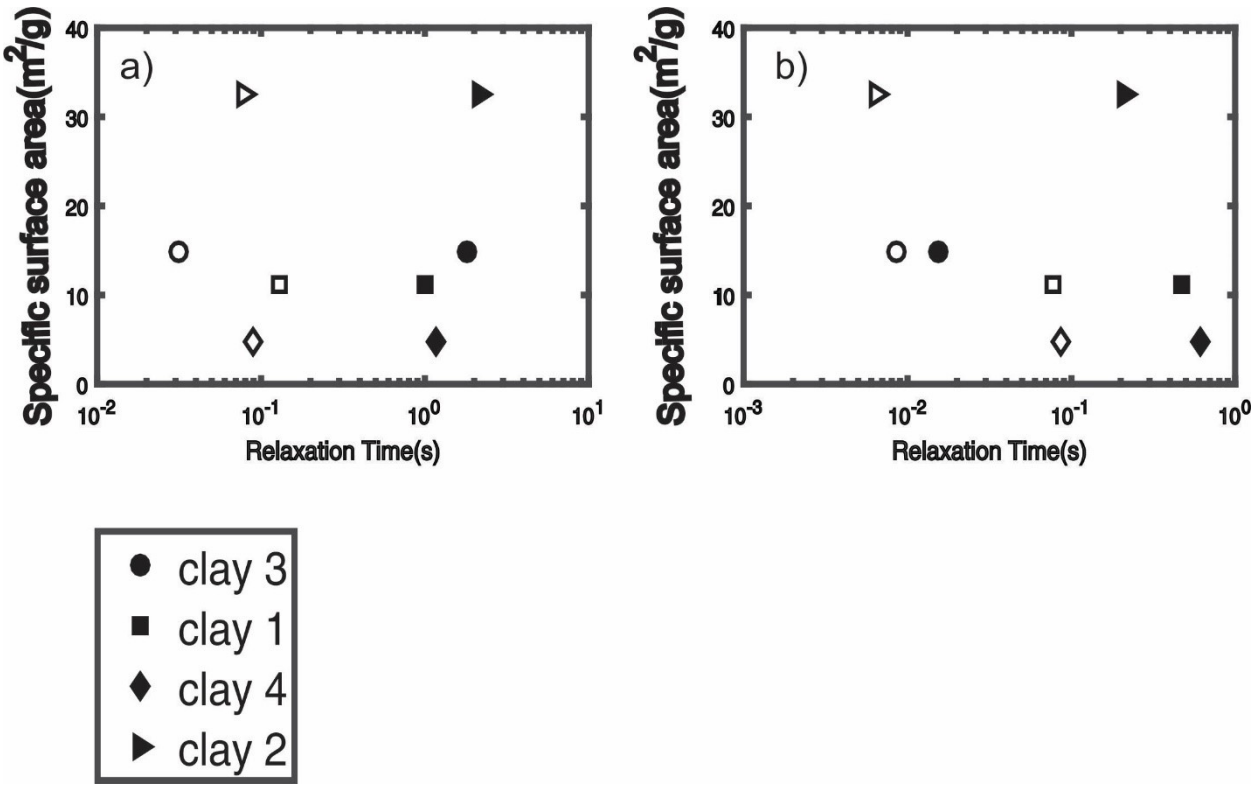

Figure 4.15. Relaxation time vs the clay specific surface area for relaxation times calculated by (a) hand picking and (b) Debye decomposition of the in-phase and quadrature resistivity spectrum. Filled and open symbols represent the samples composed of the larger and smaller beads, respectively.

4.5) Discussion

In this section we compare our results to the observations of earlier workers and interpret them within the context of various mechanistic models. To facilitate this, we will first qualitatively

outline the existing mechanistic models particularly paying attention to their presumed dominant length scales. We will then examine our results along with existing results from literature in order to determine which mechanistic models are most likely to be correct, if any.

4.5.1) Membrane polarization models

In membrane polarization models the characteristic length scales controlling the relaxation processes depend on the idealized lengths l_1 and l_2 of, respectively, the large open pores and the narrow, ion-selective pore throats as outlined in Fig 4.16. It must be remembered that real pore structures have quite different geometries and the model of Fig. 4.16 was used to allow for development of tractable solutions. For simplicity, this discussion is limited to Madden and Marshall's (1959) model (MM) and to Titov et al.'s (2002) short and narrow pores model (SNP). However, all membrane polarization models have the same basic components shown in Fig. 4.16. The open pore regions denoted A in Fig. 4.16 are "passive"; the electrolyte ions move freely and are uniformly concentrated. The narrow ion-selective passages denoted B in Fig. 4.16, in contrast, have a higher concentration of counterions due to overlapping grain boundaries (and thus EDLs). This means that when a current is applied, the counterions are preferentially displaced in the direction of the current creating a surplus on one side of the pore throat relative to the other.

Because these are charged particles, the concentration gradient results in a space charge that is measured as the IP effect.

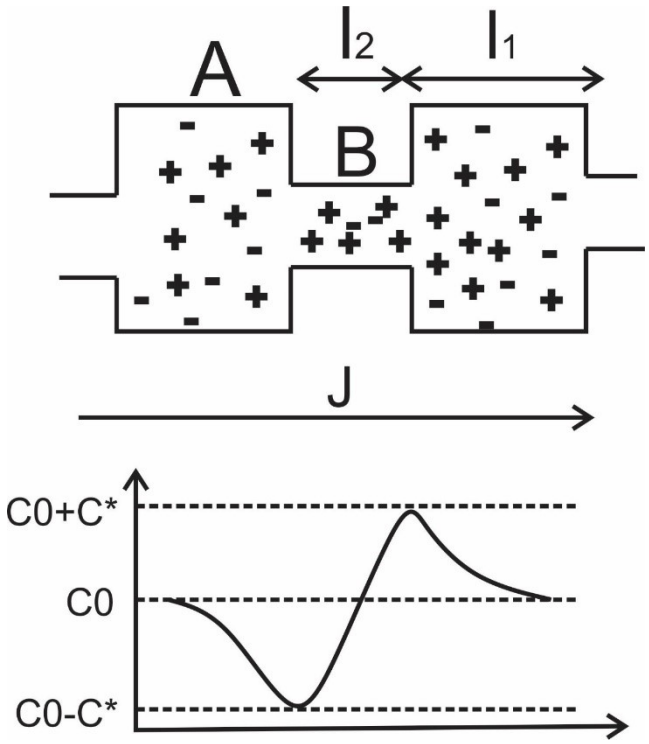

Figure 4.16. Idealized pore system (top) and concentration distribution when electric current flows (bottom). C0 – equilibrium concentration, C* additional concentration under electric field. J is the current density. Region A denotes large open pores while region B denotes narrow, ion-selective pores.

Although all membrane models have essentially these same characteristics, the specifics in the derivations of the relaxation time expressions lead to different conclusions about what length scale controls the relaxation time. This is true for the two membrane polarization models discussed here. MM produces a relaxation time that depends primarily on the length l_1 of the passive zone A. For the SNP, the relaxation time instead depends on the length l_2 of active zone B. This problem was resolved by Bücker and Hördt (2013a, 2013b) who demonstrated that both behaviours can coexist

under limiting conditions of validity. Klein and Sill (1982) point out that some of the simplifying assumptions made in the MM model derivation prevent it from making accurate quantitative predictions. The same thing may be said about the SNP model. However, these models can still give insight into the length scales that control characteristic relaxation times. Interested readers are directed to the original papers mentioned above for a full derivation. Here we will go through the main results (in frequency domain) simply to illustrate what they predict as controlling the relaxation time.

The MM model considers a series combination of clay free (denoted by subscript 1) and clay rich (denoted by subscript 2) pore throats to give a complex impedance following Klein and Sill (1982):

$$Z^*(\omega) = \frac{l_A}{\beta_A \mu_+ Fa}\left[\frac{1}{S_A\theta_A} + \frac{J}{HS_B\theta_B} + \frac{(S_B - S_A)^2}{S_B^2 S_A^2 \theta_B\theta_A\left(\frac{X_A\theta_B}{\tanh X_A} + \frac{X_2\theta_A H}{B\tanh X_B}\right)}\right] \tag{4.17}$$

where

$$H = \frac{l_A}{l_B}$$

$$J = \frac{D_A}{D_B}$$

$$S = \frac{t^-}{t^+}$$

$$X_i = \frac{r_i l_i}{2}$$

$$\theta_i = \frac{s_i + 1}{s_i}$$

$$r_i = (\frac{i\omega\theta_i}{2D_i})^{1/2}$$

and l is the length of a pore throat, β(units m^2/V-s) is the ionic mobility, μ_+ is the bulk concentration of cations (units mol/m^3), D is the diffusivity (m^2/s), and t is the unitless transference number for cations (positive super script) and anions (negative superscript). The subscripts A and B denote the clay-free and clay-rich zones, respectively. Fa is Faraday's constant (96500 Coulomb/mol) and i is an index that can be A or B. Although this is not easily obvious from examination of the equations, Klein and Sill (1982) provided a series of examples to demonstrate that the relaxation time depends on the characteristic length l_A for the clay free zone. This is an important point that should be kept in mind when we look at the SNP model.

The SNP model also consists of series combination of short and narrow pores containing clay (Region B in Fig. 4.16) and large and open pores that are clay-free (Region A in Fig. 4.16). The SNP model further assumes that the lengths of the clay-free zones are much greater than those containing clay; and means that it is only applicable to sediments with a small amount of clay. This is appropriate for the samples used in this study. In the SNP model the complex resistivity is given by:

$$\rho^*(\omega) = \rho_0\left(1 - M\left(1 - \frac{1 - e^{-2(i\omega\tau)^{\frac{1}{2}}}}{2(i\omega\tau)^{\frac{1}{2}}}\right)\right) \tag{4.18}$$

where

$$M = 4\frac{l_2\Delta n^2}{A_A + A_B + \left(\frac{1}{L_A} + \frac{1}{a_B L_B}\right)}$$

$$\tau_c = \frac{l_B^2}{4D}$$

$$L_i = A_i / l_i$$

where A is a pore's cross-sectional area, ρ_0 is the DC resistivity, Δn is the difference in ion transport numbers for large and narrow capillaries, a_B is defined as the coefficient of efficiency of the active zone equal to the ratio between the conductivity of an average capillary and that of the bulk solution, all remaining parameters have been defined previously. From Eqn. 4.18 it should be apparent that the relaxation time τ_c in the SNP model depends on the characteristic length l_2 of clay filled pore throats. This is what distinguishes it from the MM model and, as will be discussed later that has serious implications on the interpretation of the experimental results.

4.5.2) Stern layer polarization models

Numerous mathematical descriptions of the complex conductivity have emerged from variations of the Stern model (Leroy et al, 2008; Jougnot et al., 2010; Revil, 2012; Okay et al., 2014), and have been used successfully to describe complex conductivity in a variety of sandy clayey materials including those which exhibit a type *c* constant phase angle spectrum (Fig. 4.3).

The Stern layer models presume that the continuity of the diffuse layer through the porous material controls the migration of charges and hence the real part of the surface conductivity. Polarization of the less mobile Stern layer, as illustrated (Fig. 4.1c) by the migration of the charges within the EDL closest to the mineral surface to one side of the mineral grain, controls the capacitance associated with the surface conductivity. The characteristic relaxation time (τ_c) therefore has a dependence on the perimeter or surface area of the grain being polarized. Thus, if the polarization is due to the polarization of clay particles, and not the pore throat length, which is controlled by

the glass beads, we will expect the characteristic relaxation time to correspond to the specific surface area of the clays and not the size of the glass beads.

4.5.3) Comparison to Experimental results

As mentioned earlier, Klein and Sill (1982) demonstrated that the characteristic relaxation time was most influenced by glass bead size for samples similar to those used here. They also showed the relaxation times increased with increasing clay content. Revil et al. (2015) noted the increase in τ_c with increased clay content, but instead explained this in terms of the decreased diffusion coefficient for counter ions in the Stern layer of clay particles. If we interpret the change in τ_c as a change in length instead of a change in D, the MM model suggests the increased relaxation times indicate larger separation distances between the ion selective zones (i.e. the clay filled pore throats). In this light, interpreting Klein and Sill's result based on the MM model seems counterintuitive as the distance between ion selective zones should logically decrease upon the addition of clay.

The SNP model, in which the relaxation times correspond to the "length" of the ion selective zones as opposed to the distances between them, may be more consistent with the observations. In this scenario, added clay allows larger areas of the passive grains to be coated such that the length of the ion selective zone increases. This happens regardless of any changes to the diffusion coefficients. This occurs only to a point, however, in that the addition of further clay leads to a breakdown in the key assumption that the ion selective zones be much smaller than the passive zones. This agrees with observations that clay-rich rocks are the least likely to exhibit a clear peak frequency f_p.

Our results for samples S1-S8 show that the influence of the glass bead sizes on τ_c dominates that of clay specific surface areas SSA (Figs. 4.13, 4.14). This is despite the fact that measurable phase lags were not observed until clay was introduced to the glass beak packs. Further, in the tests with the differing clays, the observed τ_c do not appear to be affected by the clays' SSA (Fig. 4.15). This suggests that the Stern layer polarizations, in which the ions are confined close to the clay surfaces, do not significantly contribute to the observed polarizations.

At this point it seems clear that Stern layer polarization does not explain the difference in τ_c for our samples. Also, the results for studies using samples with glass beads (Klein and Sill, 1982); Titov et al, 2002; Leroy et al,2008) can be explained by a membrane polarization model. That said, the majority of SIP data is collected on rocks where it is impossible to completely separate constituent minerals. Thus, sieve analysis and mercury injection have been the preferred methods for inferring characteristic pore length scales against which SIP relaxation times might be interpreted.

When particle size distribution (PSD) is well characterized, workers (e.g. Leroy et al.,2008; Jougnout et al.,2010) have used the PSDs to fit the observed spectra well. Authors have interpreted this as support for Stern layer polarization. This neglects the differing effects different minerals may have on pore structure and electro-chemical properties.

Scott and Baker (2003) obtained pore throat diameters using Hg injection porosimetry and showed a correlation between the pore throat diameters and τ_c. Scott (2006) later suggested that there is a polarization mechanism at work in the pore space, although they did not hypothesize what the responsible mechanism might be. They suggested, on the basis that the dimensions of the pore throats measured by the mercury injection greatly exceeded the expected EDL thickness of ~100

nm (Lesmes and Frye, 2001), that membrane polarization was impossible. However, their interpretation neglects the likely occurrence of membrane polarization at the small dimensions along grain contacts and the narrowest pore throats, and not in large open pores which are included in the mean.

The concept of a pore throat length (l_B) is illustrated in Fig. 4.16. While this provides a useful framework that allows for the development of analytic expressions, it is impossible to actually measure an average pore throat length in a granular material in order to demonstrate an association between it and τ_c experimentally, and the current observations together with earlier glass bead and clay mixture experiments (Vaquier,1957; Klein and Sill, 1982; Titov et al,2002) are all consistent with SNP model. Our results cannot be explained by the Stern layer model because, although the polarization is caused by the clay particles, the relaxation times do not correlate to the length scale of the clay. This means that the grains themselves do not polarize as the Stern layer model assumes. Other experimental observations (Klein and Sill, 1982) are inconsistent with the MM model. Consequently, the SNP model appears to be most consistent with all results examined here.

4.6) Conclusion

Seeking additional insight into the origins of low frequency (<100 Hz) electrical polarisations in porous sandy-sediments saturated with a weak NaCl electrolyte, we conducted experiments on packed mixtures of glass beads with small amounts of different clays. Specifically, the measurements attempted to address whether the pore scale ionic displacements, that control the sediment's characteristic relaxation time τ_c, are most consistently described by either the membrane or the Stern-layer polarization models. The two primary observations are:

1) The clay-free glass bead packs display little SIP response within the experimental detection limits, but clearly observable polarizations appear upon the addition of small amounts of clay.

2) In the clay-containing samples, the observed characteristic relaxation times τ_c increase with the radii of the non-clay solid passive grains. However, τ_c is essentially independent of the differences in the clays as quantified by their significantly varying specific surface areas (SSA) and cation exchange capacities (CEC).

Taken together, these observations suggest that Stern layer polarisation, that would depend on clay surface dimensions, cannot explain the observed τ_c. Membrane polarisation models, that depend primarily on the length of pore throats in the direction of current flow, most appropriately explain our observations. Observed correlations between pore throat diameter and τ_c result from the correlation between an idealized pore throat length and the measurable pore throat diameter.

Further studies of this type using a greater variety of glass bead sizes with better known grain size distributions can be used to constrain the relationship between grain size and relaxation time more precisely.

The results presented here should influence the interpretation of IP data when conductive or semi-conductive grains can be assumed absent. Changes in quadrature conductivity magnitudes may indicate a change in the surface properties of the grains which is influenced by the pore fluid chemistry. On the other hand, changes in the relaxation times indicate changes in polarization length scales which can be related to chemically inactive grains. An example of what my cause this is fractures, which, create a new network of narrow pore throats which can affect average relaxation times for the material.

Acknowledgements – This work was funded within Dr. Schmitt's NSERC Discovery Grant.

Special thanks to Randolf Kofman for his assistance with the lab work.

Appendix

Table 4.A1. Measured in-phase and quadrature resistivities at various frequencies for sample S1

Frequency (Hz)	In-Phase resistivity (ohm-m)	Quadrature Resistivity (ohm-m)
0.01	118	0
0.02	117	0.02
0.04	117	0.12
0.08	117	0.23
0.1	117	0.25
0.2	117	0.39
0.4	117	0.47
0.8	115	0.52
1	115	0.54
2	114	0.58
4	113	0.61
8	113	0.67
10	113	0.61
20	112	0.76
40	111	0.93
80	111	1.26
100	111	1.39
200	110	1.83
400	110	2.62
800	109	3.93
1000	108	4.53

Table 4.A2. Measured in-phase and quadrature resistivities at various frequencies for sample S2

Frequency (Hz)	In-Phase resistivity (ohm-m)	Quadrature Resistivity (ohm-m)
0.01	27.6	0
0.02	27.6	0
0.04	27.6	0
0.08	27.5	0
0.1	27.5	0
0.2	27.5	0
0.4	27.5	0
0.8	27.5	0
1	27.5	0
2	27.5	0.024

4	27.5	0.048
8	27.5	0.057
10	27.4	0.043
20	27.4	0.072
40	27.3	0.086
80	27.3	0.100
100	27.3	0.110
200	27.2	0.138
400	27.2	0.256
800	27.1	0.402
1000	27.1	0.482

Table 4.A3. Measured in-phase and quadrature resistivities at various frequencies for sample S3

Frequency (Hz)	**In-Phase resistivity (ohm-m)**	**Quadrature Resistivity (ohm-m)**
0.01	59.6	0.79
0.02	59.6	0.83
0.04	58.6	0.86
0.08	57.5	0.87
0.1	57.1	0.88
0.2	56.5	0.85
0.4	56.0	0.82
0.8	55.4	0.80
1	55.1	0.80
2	54.6	0.76
4	54.1	0.72
8	53.6	0.68
10	53.4	0.68
20	52.9	0.67
40	51.6	0.67
80	51.4	0.68
100	51.4	0.68
200	51.1	0.68
400	50.8	0.85
800	50.5	0.94
1000	50.5	0.99

Table 4.A4. Measured in-phase and quadrature resistivities at various frequencies for sample S4

Frequency (Hz)	In-Phase resistivity (ohm-m)	Quadrature Resistivity (ohm-m)
0.01	30.6	0
0.02	30.6	0.011
0.04	30.6	0.005
0.08	30.5	0.011
0.1	30.5	0.005
0.2	30.5	0.005
0.4	30.5	0.011
0.8	30.5	0.021
1	30.5	0.037
2	30.5	0.043
4	30.5	0.037
8	30.5	0.027
10	30.4	0.021
20	30.4	0.032
40	30.4	0.058
80	30.3	0.122
100	30.3	0.153
200	30.2	0.232
400	30.1	0.341
800	30.0	0.570
1000	30.0	0.663

Table 4.A5. Measured in-phase and quadrature resistivities at various frequencies for sample S5

Frequency (Hz)	In-Phase resistivity (ohm-m)	Quadrature Resistivity (ohm-m)
0.01	108	1.82
0.02	108	2.60
0.04	108	3.29
0.08	107	3.83
0.1	107	4.00
0.2	105	4.09
0.4	102	3.76
0.8	101	3.12
1	100	2.88
2	99	2.13
4	99	1.44
8	98	0.89
10	98	0.70
20	97	0.39
40	97	0.27
80	96	0.32

100	96	0.42
200	95	0.78
400	95	1.58
800	95	3.14
1000	95	3.91

Table 4.A6. Measured in-phase and quadrature resistivities at various frequencies for sample S6

Frequency (Hz)	In-Phase resistivity (ohm-m)	Quadrature Resistivity (ohm-m)
0.01	24.4	0
0.02	24.4	0.034
0.04	24.4	0.068
0.08	24.5	0.090
0.1	24.5	0.098
0.2	24.4	0.153
0.4	24.3	0.178
0.8	24.3	0.195
1	24.2	0.198
2	24.1	0.193
4	24.0	0.167
8	23.9	0.133
10	23.9	0.112
20	23.8	0.0788
40	23.7	0.066
80	23.7	0.083
100	23.7	0.095
200	23.7	0.116
400	23.6	0.214
800	23.5	0.308
1000	23.50	0.349

Table 4.A7. Measured in-phase and quadrature resistivities at various frequencies for sample S7

Frequency (Hz)	In-Phase resistivity (ohm-m)	Quadrature Resistivity (ohm-m)
0.01	66.4	0.60244
0.02	67.0	0.72524
0.04	65.7	0.83675
0.08	65.4	0.90121
0.1	65.3	0.9112
0.2	64.9	0.90552
0.4	64.6	0.82251
0.8	64.3	0.70661
1	64.2	0.63869

2	63.3	0.44225
4	63.2	0.30872
8	63.1	0.17614
10	63.1	0.12109
20	63.1	0.13219
40	62.7	0.22967
80	62.9	0.23037
100	62.9	0.44981
200	62.6	0.68857
400	62.5	1.0693
800	62.3	1.958
1000	62.2	2.3679

Table 4.A8. Measured in-phase and quadrature resistivities at various frequencies for sample S8

Frequency (Hz)	**In-Phase resistivity (ohm-m)**	**Quadrature Resistivity (ohm-m)**
0.01	23.4	0.090
0.02	23.5	0.090
0.04	23.5	0.094
0.08	23.6	0.086
0.1	23.6	0.086
0.2	23.5	0.094
0.4	23.5	0.098
0.8	23.4	0.110
1	23.4	0.114
2	23.3	0.118
4	23.2	0.114
8	23.2	0.109
10	23.1	0.105
20	23.1	0.113
40	23.0	0.124
80	22.9	0.128
100	22.9	0.136
200	22.8	0.152
400	22.8	0.195
800	22.7	0.290
1000	22.7	0.349

4.7) References

Archie, G. E. (1942). The electrical resistivity log as an aid in determining some reservoir characteristics. *Transactions of the American Institute of Mining and Metallurgical Engineers* 146: 54-62

Atekwana, E. A., and D. L. Slater (2009). Biogeophysics: A New Fronteir in Earth Science Research. *Reviews of Geophysics* 30.

Avellaneda, M., and S. Torquato (1991). Rigorous link between fluid permeability, electrical conductivity, and relaxation times for transport in porous media. *Physics of fluids* 3 (11): 2529-2540.

Bairlein, K., A. Hordt, and S. Nordsiek (2014). The influence on sample preparation on spectral induced polarization of unconsolidated sediments. *Near Surface Geophysics* 12 (5): 667-677.

Bona, N., E. Rossi, S. Capaccioli, and M. Lucchesi. (2008) Electrical Measurements : Considerations on the Performance of 2- and 4-Contact Systems. Abu Dhabi: International Symposium of the Society of Core Analysts. 1-12.

Bouzidi, Y. (2003). *The acoustic reflectivity and transmissivity of liquid saturated porous media: experimental tests of theoretical concepts.* Ph.D Thesis, Edmonton: Department of Physics, University of ALberta.

Brady, P., R. Cygan, and K. Nagy (1996). Molecular Controls on Kaolinite Surface Charge. *Journal of Colloid and Interface Science* 183 (2): 356-364.

Breede, K., A. Kemna, O. Esser, E. Zimmermann, H. Vereecken, and J. A. Huisman (2012). Spectral induced polarization measurements on variably saturated sand-clay mixtures." *Near Surface Geophysics* 10 (6): 479-489.

Bruggeman, D. (1935). Berechnung Verschiedeneren Physicalischer Konstanten von Heterogenen Substanzen. *Annals of Physics* 24: 636-679.

Brunauer, S., P. Emmett, and E. Teller. (1938) Adsorption of Gases in Multimolecular Layers. *Journal of the American Chemical Society* 60 (2): 309-319.

Bucker, M., and A. Hordt (2013a). Analytical modelling of membrane polarization with explicit parametrization of pore radii and the electrical double layer. *Geophysical Journal International* 194 (2): 804-813.

Bucker, M., and A. Hordt (2013b). Long and short narrow pore models for membrane polarization. *Geophysics* 78 (6).

Bussian, A. (1983). Electrical conductance in a porous medium. *Geophysics* 48 (9): 1258-1268.

Chelidze, T., and Y. Gueguen (1999). Electrical spectroscopy of porous rocks: a review—I.Theoretical models. *Geophysical Journal International* 137 (1): 1-15.

Cole , K., and R. Cole (1941). Dispersion and absorption in dielectrics. *Jorunal of Chemical Physics* 9: 341-351.

Donnan, F. G (1924). The theory of membrane equilibria. *Chemical Reviews* 1: 73-90.

Florsch, N., A. Revil, and C. Camerlynck (2014). Inversion of generalized relaxation time distributions with optimized dampling parameter. *Journal of Applied Geophysics* 109: 119-132.

Hanai, T. (1968). Electrical properties of emulsions. Edited by P. Sherman. *Emmulsion Science* (Academic Press) 354-478.

Huisman, J. A., E. Zimmermann, O. Esser, F. Haegel, A. Treichel, and H. Vereecken (2015). Evaluation of a novel correction procedure to remove electrode impedance effects from broadband SIP measurements. *Journal of Applied Geophysics* 135: 466-473.

Islam, M. A. (2004). Einstein–Smoluchowski Diffusion Equation: A Discussion. *Physica Scripta* 70 (120): 120-125.

Joseph, S., I. Malcolm, and G. Gouws (2016). Spectral-induced polarization measurements on sieved sands and the relationship to permeability. *Water Resources Research* 52: 1-20.

Jougnot, D., A Ghorbani, A. Revil, P. Leroy, and P. Cosenza (2010). Spectral induced polarization of partially saturated clay-rocks: A mechanistic approach. *Geophysical Journal International* 180: 210-224.

Klein, J., and W. Sill (1982). Electrical properties of Artificial clay-bearing sandstone. *Geophysics* 47 (11): 1593-1605.

Leroy, P., A. Revil, A. Kemna, P. Cosenza, and A. Ghorbani (2008). Complex conductivity of water-saturated packs of glass beads. *Journal of Colloid and Interface Science* 321: 103-117.

Lesmes, D., and K. Frye (2001). Influence of pore fluid chemistry on the complex conductivity and induced polarization responses of Berea sandstone. *Journal of Geophysical Research* 106 (B3): 4079-4090.

Lukichev, A. (2014). Relaxation function for the non-Debye relaxation spectra sescription. *Chemical Physics* 428: 29-33.

Marshall, D. J., and T. R. Madden (1959). Induced polarisation, a study of its causes. *Geophysics* XXIV (4): 790-816.

Nordsiek, S., and A. Weller (2008). A new approach to fitting induced-polarization spectra. *Geophysics* 73 (6): F235-F245.

Okay, G., P. Leroy, A. Ghorbani, P. Cosenza, C. Camerlynck, J. Cabrera, N. Florsch, and A. Revil (2014). Spectral induced polarization of clay-sand mixtures: Experiments and modeling. *Geophysics* 79 (6): E353-E375.

Pelton, W.H., S.H. Ward, P.G. Hallof, W.R. Sill and P.H. Nelson (1978). Mineral discrimination and removing of inductive coupling with multifrequency IP. *Geophysics* 43: 588-609.

Revil, A. (2012). Spectral induced polarization of shaly sands: Influence of the electrical double layer. *Water Resources Research* 48: W02517.

Revil, A. (2013). Effective conductivity and permittivity of unsaturated porous materials in the frequency range 1 mHz-1GHz. *Water Resources Research* 49 (1): 306-327.

Revil, A., and L. M. Cathles (1999). Permeability of shaly sands. *Water Resources Research* 35 (3): 651-662.

Revil, A., and P. Glover (1998). Nature of surface electrical conductivity in natural sands, sandstones, and clays. *Geophysical research letters* 25 (5): 691-694.

Revil, A., K. Koch, and K. Holliger (2012). Is it the grain size or the characteristic pore size that controls the induced polarization relaxation time of clean sands and sandstones? *Water Resources Research* 48 (5): 1-7.

Revil, A., A. Binley, L. Mejus, and P. Kessouri (2015). Predicting permeability from the charactaristic relaxation time and intrinsic formation factor of complex conductivity spectra. *Water Resources Research* 51: 6672-6700.

Schwarz, G. (1962). A theory of the low frequency dielectric dispersion of colloidal particles in electrolyte solutions. *Journal of Physical Chemistry* 66: 2626-2635.

Scott, J. (2006). The origin of the observed low-frequency electrical polarization in sandstones. *Geophysics* 71 (5): G235-G238.

Scott, J., and R. Barker (2003). Determining pore-throat size in Permo-Triassic sandstones from low-frequency electrical spectroscopy. *Geophysical Research Letters* 30 (9): 1-4.

Sen, P., C. Scala, and M. Cohen (1981). A self-similar model for sedimentary rocks with application to the dielectric constant of fused glass beads. *Geophysics* 46 (5): 781-795.

Slater, Lee, and David P. Lesmes (2002). Electrical- hydraulic relationships observed for unconsolidated sediments. *Water Resources Research* 38 (10): 1-13.

Sumner, J. S. (1976). *Principals of induced polarisation for geophysical exploration.* Elsevier.

Tarasov, A., and K. Titov (2007). Relaxation time distribution from time domain induced polarization measurements. *Geophysics Journal International* 170 (1): 31-43.

Titov, K., V. Komarov, V. Tarasov, and A. Levitski (2002). Theoretical and experimental study of time domain-induced polarization in water-saturated sands. *Journal of Applied Geophysics* 50: 417-433.

Ustra, Andrea, Alberto Mendonca, Ntarlagiannis Dimitrios, and Lee D. Slater (2016). Relaxation time distribution obtained by Debye decomposition of spectral induced polarisation data. *Geophysics* 81 (2): E129-E138.

Vacquier, V., C. Holmes, P. Kitzinger, and M. Lavergne (1957). Prospecting for groundwater by induced polarization. *Geophysics* 22: 660-687.

Van Genuchten, M.Th. (1980). A closed-form equation for predicting the hydraulic conductivity of unsaturated soils. *Soil Science Society of America* 892-898.

Vanhala, H. (1997). Mapping oil-contaminated sand and tillwith the spectral induced polarization (SIP) method. *Geophysical Prospecting* 45: 303-326.

Wang, M., J. Lui, and S. Chen (2008). Electric potential distribution in nanoscale electroosmosis: from molecules to continuum. *Molecular Simulation* 34 (5): 509-514.

Waxman, M. H., and L. J.M. Smits (1968). Electrical Conductivities in Oil-Bearing Shaly Sands . *Society of Petroleum Engineers Journal* 107-122.

Weller, A., L. Slater, and S. Nordsiek (2013). On the relationship between induced polarization and surface conductivity: Implications for petrophysical interpretation of electrical measurements. *Geophysics* 78 (5): D315-D325.

Weller, A., Z. Zhang, L. Slater, S. Kruschwitz and M. Halisch (2016).Induce polarization and pore radius – A discussion. *Geophysics* 81 (5): D519-D526.

Williams, Kenneth H., Andreas Kemna, Michael J. Wilkins, Jennifer Druhan, Evan Arntzen, Lucie N'Guessan, Philip E. Long, Susan S. Hubbard, and Jillian F. Banfield (2009). Geophysical monitoring of coupled microbial and geochemical processes during simulated subsurface bioremediation. *Environmental Science and Technology* 43: 6717-6723.

Zimmermann, E., A. Kemna, J. Berwix, W. Glaas, H. Munch, and J. Huisman (2008). A high-accuracy impedance spectrometer for measuring sediments with low polarizability. *Measurement Science and Technology* 19: 9pp.

Zisser, N., A. Kemna, and G. Nover (2010). Relationship between low-frequency electrical properties and hydraulic permeability of low-permeability sandstones. *Geophysics* 75 (3): E131-E141.

Chapter 5

Conclusions and directions for future research

5.1) Contributions of Work Described Here

Electrical measurements hold a wealth of information on fluid properties and pore geometry. However, there remains a lack of understanding on how best to extract this information. To this end, the work presented has made 3 contributions by: i) Demonstrating how electrical properties can be used to help constrain inversions for elastic parameters, ii) providing a novel experimental setup for studying the effects of fracture induced anisotropy and iii) providing measurements which suggest that a membrane polarization mechanism is responsible for observed induced polarization responses.

First, we contribute a set of measurements that show the nature of the pressure dependence for elastic wave velocities and electrical resistivities. Both are pressure dependent due to the opening and closing of microcracks. By treating the cracks as nominally flat, rough surfaces in contact, we were able to combine models for electrical conductivity and elastic stiffness of cracked/fractured rock. Doing this allowed us to constrain the microstructural parameters of the model better than had been done by previous workers while still fitting the data well. The model can be used to help predict changes in surveys (seismic and electrical) expected after well production or injection.

We then presented a novel experimental set up for studying the effects of fractures on electrical anisotropy. The use of artificial samples allowed us to definitively show that the observed anisotropy was caused by fractures. It also allowed us to know the specific orientation of the

fracture and the crack porosity of that sample. The measured anisotropy ratios were used to provide an empirical equation that gives the anisotropy ratio as a function of the ratio of crack porosity to total porosity. It was also shown that the change in the inverse formation factors (in directions perpendicular and parallel to the fracture) were all quite close to the crack porosity. This supports the idea that the inverse formation factor is a measure of the porosity connected by lines of current. This work can be used to model the change in anisotropy expected in reservoirs after they have been fractured.

Finally, we provided spectral induced polarisation measurements on artificial sediments. The sediments were composed of one of four types of clay and one of two sizes of glass beads. The experiment was designed to determined weather the observed response was most likely due to Stern layer polarization of membrane polarization. The results suggested that, although the clay grains caused the observed polarization, the glass bead size controlled the characteristic relaxation time. This along with other results in the literature suggest that membrane polarization is responsible for the observed relaxation times in rocks and sediments. An examination of Debye decomposition suggested that hand-picked relaxation times from observed spectra are more reliable than those picked from averaging relaxation times obtained from inversions. This work should affect the way changes in SIP spectra are interpreted.

5.2) Suggestions for Future Research

The first two chapters both dealt with the effects of cracks and fractures on electrical properties. The problems of pressure dependence and anisotropy were therefore examined independently. However, future research should integrate these two problems since they both are caused by cracks

and fractures. The following is a list of topics that we were unable to complete and remain to be done:

- Further constrain the relationship between the anisotropy ratio and the ratio of crack porosity to total porosity in an environment with oriented fractures.
- Perform elastic wave velocity and electrical conductivity measurements at elevated pressures to obtain full elastic stiffness and conductivity tensors for anisotropic rocks.
- Model the effects of fractures on conductivity in terms of a crack density tensor like that used by Kachanov (1992). This would allow for better integration of the effective medium models for elastic parameters with an electrical conductivity model of cracked solids.

The third chapter dealt with the mechanism behind induced polarization in sediments. Because of the measurement is so sensitive to noise (owing to very small phase lags that have to be measured), much of the time was dedicated to learning how to do the measurement accurately. Because of this there were several topics of interest that were not done. The following is a list of topics that we were unable to complete and remain to be done:

- Examine the effects of cracks and fractures on induced polarization in rocks that typically show a clear peak frequency.
- Examine the effects of different biofilm growths on characteristic relaxation time. This has been proposed as a mechanism for fracture healing in concrete and SIP is a suggested way of monitoring it.

5.3) Bibliography

Abousrafa, E. M., J. M. Somerviller, S. A. Hamilton, and P. W.H. Olden (2013). A laboratory measurement technique for axial and radial resistivity at ambient or reservoir stress state conditions. *Journal of Petroleum Science and Engineering* 102: 57-65.

Adams, L. H., and E. D. Williamson. (1923). Compressibility of minerals and rocks at high pressures. *Journal of the Franklin Institute* 195: 475-529.

Anderson, B., B. Bryant, M. Lu ling, B. Spies, and K. Helbig (1994). Oilfield anisotropy: Its origins and electrical characteristics. *Oilfield Review:* 48–56.

Aquino-Lopez, A., A. Mousatov, and M. Markov. (2011). Model of sand formations for joint simulation of elastic moduli and electrical conductivity. *Journal of Geophysics and Engineering* 8 (4): 568-578.

Archie, G. E. (1942). The electrical resistivity log as an aid in determining some reservoir characteristics. *Transactions of the American Institute of Mining and Metallurgical Engineers* 146: 54-62

Asami, K. (2002). Asami, K. (2002). "Characterization of heterogeneous systems by dielectric spectroscopy. *Progress in Polymer Science* 27 (8): 1617-1659.

Atekwana, E. A., and D. L. Slater (2009). Biogeophysics: A New Fronteir in Earth Science Research. *Reviews of Geophysics* 30.

Avellaneda, M., and S. Torquato (1991). Rigorous link between fluid permeability, electrical conductivity, and relaxation times for transport in porous media. *Physics of fluids* 3 (11): 2529-2540.

Bachrach, R. (2011). Elastic and resistivity anisotropy of shale during compaction and diagenesis : Joint effective medium modeling and field observations. *Geophysics* 76 (6): E175-E186.

Bairlein, K., A. Hordt, and S. Nordsiek (2014). The influence on sample preparation on spectral induced polarization of unconsolidated sediments. *Near Surface Geophysics* 12 (5): 667-677.

Batzle, M., and Z. Wang. (1992). Seismic properties of pore fluids. *Geophysics* 57 (11): 1396-1408.

Bernabe, Y. (1991). Pore Geometry and pressure-dependence of the transport-properties in sandstones. *Geophysics* 56 (4): 436-446.

Bona, N., E. Rossi, S. Capaccioli, and M. Lucchesi. (2008) Electrical Measurements : Considerations on the Performance of 2- and 4-Contact Systems. Abu Dhabi: International Symposium of the Society of Core Analysts. 1-12.

Bouzidi, Y. (2003). *The acoustic reflectivity and transmissivity of liquid saturated porous media: experimental tests of theoretical concepts.* Ph.D Thesis, Edmonton: Department of Physics, University of Alberta.

Brace, W F, and A S Orange. (1968). Further Studies of the Effects of Pressure on Electrical Resistivity of Rocks. *Journal of Geophysical Research* 73 (16): 5407-5420.

Brace, W. F., A. S. Orange, and T. R. Madden. (1965). Effect of pressure on electrical resistivity of water-saturated crystalline rocks. *Journal of Geophysical Research* 70 (22): 5669-5678.

Brady, P., R. Cygan, and K. Nagy (1996). Molecular Controls on Kaolinite Surface Charge. *Journal of Colloid and Interface Science* 183 (2): 356-364.

Breede, K., A. Kemna, O. Esser, E. Zimmermann, H. Vereecken, and J. A. Huisman (2012). Spectral induced polarization measurements on variably saturated sand-clay mixtures." *Near Surface Geophysics* 10 (6): 479-489.

Brown, V., M. Hoversten, K. Key, and J. Chen (2012). Resolution of reservoir scale electrical anisotropy from marine CSEM data. *Geophysics* 77 (2): E147-E158.

Brown, V., K. Key, and S. Singh. (2012). Seismically regularized controlled-source electromagnetic inversion. *Geophysics* 77 (1): 1JF-Z19.

Bruggeman, D. (1935). Berechnung Verschiedeneren Physicalischer Konstanten von Heterogenen Substanzen. *Annals of Physics* 24: 636-679.

Brunauer, S., P. Emmett, and E. Teller. (1938) Adsorption of Gases in Multimolecular Layers. *Journal of the American Chemical Society* 60 (2): 309-319.

Bucker, M., and A. Hordt (2013a). Analytical modelling of membrane polarization with explicit parametrization of pore radii and the electrical double layer. *Geophysical Journal International* 194 (2): 804-813.

Bucker, M., and A. Hordt (2013b). Long and short narrow pore models for membrane polarization. *Geophysics* 78 (6).

Burns, D. R., C. H. Cheng, and R. H. Wilkins. (1990). Sandstone Pore Aspect Ratio Spectra from Direct Observations and Velocity Inversion. *International Journal of Rock Mechanics and Mining Sciences & Geomechanics Abstracts* 27 (4): 315-323.

Bussian, A. (1983). Electrical conductance in a porous medium. *Geophysics* 48 (9): 1258-1268.

Carcione, Jose, Bjorn Ursin, and Janniche Nordskeg (2007). Cross-property relations between electrical conductivity and the seismic velocity of rocks. *Geophysics* 72 (5): E193-E204.

Carlson, R. L., and A. F. Gangi (1985). Effect of cracks on the pressure-dependence of P-wave velocities in crystalline rocks. *Journal of Geophysical Research-Solid Earth and Planets* 90 (NB10): 8675-8684.

Chapman, M. (2003). Frequency-dependent anisotropy due to meso-scale fractures in the presence of equant porosity. *Geophysical Prospecting* 51 (5): 369-379.

Chelidze, T L, and Y. Gueguen (1999). Electrical spectroscopy of porous rocks: a review -I Theoretical models. *Geophysical Journal International* 137: 1-15.

Cheng, C. H., and M. N. Toksoz (1979). Inversion of seismic velocities for the pore aspect ratio spectrum OF a rock. *Journal of Geophysical Research* 84 (NB13): 7533-7543.

Cole , K., and R. Cole (1941). Dispersion and absorption in dielectrics. *Jorunal of Chemical Physics* 9: 341-351.

David, C., P. Robion, and L. Laurent (2017). "A single laboratory setup for investigating the anisotropy of both seismic and electrical properties in core samples." *Geophysical Journal International* 210: 1595-1608.

David, E. C., and R. W. Zimmerman (2012). Pore structure model for elastic wave velocities in fluid-saturated sandstones. *Journal of Geophysical Research-Solid Earth* 117: B07210.

De Lima O. A. L., M.M. Sharma A generalized Maxwell-Wagner theory for membrane polarization in shaly sands. *Geophysics* 57(3): 431-440

Donnan, F. G (1924). The theory of membrane equilibria. *Chemical Reviews* 1: 73-90.

Doyen, P. M. (1987). Crack geometry in igneous rocks - a maximum-entropy inversion of elastic and transport-properties. *Journal of Geophysical Research-Solid Earth and Planets* 92 (B8): 8169-8181.

Durr, O., W. Dieterich, P. Maass, and A. Nitzan (2002). Effective Medium Theory of Conduction in Stretched Polymer Electrolytes. *Journal of Physical Chemistry B* 106: 6149-6155.

Ellis, M., M. Sinha, and R. Parr (2010). Role of fine-scale layering and grain alignment in the electrical anisotropy of marine sediments. *First Break* 28 (9): 49-57.

Fatt, I., and D. H. Davis (1952). Reduction in permeability with overburden pressure. *Transactions of the American Institute of Mining and Metallurgical Engineers* 195: 329-329.

Florsch, N., A. Revil, and C. Camerlynck (2014). Inversion of generalized relaxation time distributions with optimized dampling parameter. *Journal of Applied Geophysics* 109: 119-132.

Gangi, A. F (1978). Variation of whole and fractured porous rock permeability with confining pressure. *International Journal of Rock Mechanics and Mining Sciences & Geomechanics Abstracts* 15 (5): 249-257.

Gangi, Anthony, and Richard Carlson (1996). An asperity deformation model for effective pressure. *Tectonophysics* 256: 241-251.

Gao, K., and R. L. Gibson Jr. (2012). Pressure-dependent seismic velocities based on effective compliance theory and an asperity deformation model. *Geophysics* 77 (6): D229-D243.

Gassmann, F. (1951). Elastic Waves through packing of spheres. *Geophysics* 16 (4).

Glover, P. W.J., and F. J. Vine (1995). Beyond KTB - electrical conductivity of the deep continental crust. *Surveys in Geophysics* 16 (1): 5-36.

Glubokovskikh, S., B. Gurevich, M. Lebedev, V. Mikhaltsevitch, and S. Tan (2016). Effect of asperities on stress dependency of elastic properties of cracked rocks. *International Journal of Engineering Science* 98: 116-125.

Gomez, C. T., J. Dvorkin, and T. Vanorio (2010). Laboratory measurements of porosity , permeability , resistivity , and velocity on Fontainebleau sandstones. *Geophysics* 75 (6): E191-E204.

Greenwood, J. A., and J. B. Williamson (1966). Contact of nominally flat surfaces. *Proceedings of the Royal Society of London Series a-Mathematical and Physical Sciences* (295): 300-310.

Han, T.C. (2018). Joint Elastic-Electrical Properties of Artificial Porous Sandstone With Aligned Fractures. *Geophysical Research Letters* 45 (7): 3051-3058.

Han, T. C. (2018). An effective medium approach to modelling the pressure-dependent electrical properties of porous rocks. *Geophysical Journal International* 214 (1): 70-78.

Han, T. C. (2016). Are self-consistent models capable of jointly modeling elastic velocity and electrical conductivity of reservoir sandstones? *Geophysics* 81 (4): D377-D382.

Han, T.C., M. Josh, and H. Liu (2019). Effects of aligned fractures on the dielectric properties of synthetic porous sandstones. *Journal of Petroleum Science and Engineering* 172: 436-442.

Han, T.C., A. Best, J. Sothcott, and L. Macgregor (2011). Joint elastic-electrical properties of reservoir sandstones and their relationships with petrophysical parameters. *Geophysical Prospecting* 59: 518-535.

Hanai, T. (1968). Electrical properties of emulsions. Edited by P. Sherman. *Emmulsion Science* (Academic Press) 354-478.

Hashin, Z. (1988). The differential scheme and its application to cracked materials. *Journal of Mechanics and Physics of Solids* 36: 719-734.

Hill, D. G. 1972. Laboratory investigation of electrical anisotropy in precambrian rocks. *Geophysics* 37 (6): 1022-1038.

Honig, B., and A. Nicholls (1995). Classical electrostatics in biology and chemistry. *Science* 268(5214): 1144-1149.

Huisman, J. A., E. Zimmermann, O. Esser, F. Haegel, A. Treichel, and H. Vereecken (2015). Evaluation of a novel correction procedure to remove electrode impedance effects from broadband SIP measurements. *Journal of Applied Geophysics,* 135, 466-473

Islam, M. A. (2004). Einstein–Smoluchowski Diffusion Equation: A Discussion. *Physica Scripta* 70 (120): 120-125.

Izumotani, S., and S. Onozuka (2013). Elastic moduli and the aspect ratio spectrum of rock using simulated annealing. *Geophysical Prospecting* 61: 489-504.

Jensen, E. H., L. J. Gelius, T. A. Johansen, and Z. Wang (2013). Consistent joint elastic-electrical differential effective-medium modelling of compacting reservoir sandstones. *Geophysical Prospecting* 61 (4): 788-802.

Joseph, S., I. Malcolm, and G. Gouws (2016). Spectral-induced polarization measurements on sieved sands and the relationship to permeability. *Water Resources Research* 52: 1-20.

Jougnot, D., A Ghorbani, A. Revil, P. Leroy, and P. Cosenza (2010). Spectral induced polarization of partially saturated clay-rocks: A mechanistic approach. *Geophysical Journal International* 180: 210-224.

Johnson, D. L., T. J. Plona, and H. Kojima (1986). Probing porous media with 1st sound, 2nd sound, 4th sound and 3rd sound. Edited by R. Jayanth, J. Banavar and K. W. Winkler. *Physics and Chemistry of Porous Media.* New York. 243-277.

Kachanov, Mark (1992). Effective elastic properties of cracked solids: critical review of some basic concepts. *Applied Mechanics Reviews* 45 (8): 304-335.

Karaoulis, M, A. Revil, D.D. Werkema, B.J. Minsley, W.F. Woodruff, A. Kemna (2011). Time-lapse three-dimensional inversion of complex conductivity data using an active time constrained (ATC) approach. *Geophysics Journal International* 187 (1): 237-251.

Kazatchenko, E., M. Markov, A. Mousatov, and J. O. Parra (2006). Carbonate microstructure determination by inversion of acoustic and electrical data: Application to a south Florida aquifer. *Journal of Applied Geophysics* 59 (1): 1-15.

Klein, J., and W. Sill (1982). Electrical properties of Artificial clay-bearing sandstone. *Geophysics* 47 (11): 1593-1605.

Kozlov, E. (2004). Pressure-dependent seismic response of fractured rock. *Geophysics* 69 (4): 885-897.

Leroy, P., A. Revil, A. Kemna, P. Cosenza, and A. Ghorbani (2008). Complex conductivity of water-saturated packs of glass beads. *Journal of Colloid and Interface Science* 321: 103-117.

Lesmes, D., and K. Frye (2001). Influence of pore fluid chemistry on the complex conductivity and induced polarization responses of Berea sandstone. *Journal of Geophysical Research* 106 (B3): 4079-4090.

Leibecker, J., A. Gatzemeier, M. Honig, O. Kuras, and S. Wolfgang (2002). Evidence of electrical anisotropic structures in the lower crust and the upper mantle beneath the Rhenish Shield. *Earth and Planetary Science Leters* 202: 289-302.

Liu, Y., A. Kitanidis, P.K. (2013). Tortuosity and Archie's Law. In: Mishra P., Kuhlman K. (eds) Advances in Hrdrogeology. Springer, New York, NY.

Louis, L., C. David, and P. Robion (2003). Comparison of the anisotropic behaviour of undeformed sandstones under dry and saturated conditions. *Tectonophysics* 370 (1-4): 193-212.

Lukichev, A (2014). Relaxation function for the non-Debye relaxation spectra sescription. *Chemical Physics* 428: 29-33.

MacBeth, C., J. Stammeijer, and M. Omerod (2006). Seismic monitoring of pressure depletion evaluated for a United Kingdom continental-shelf gas reservoir. *Geophysical Prospecting* 54 (1): 29-47.

Marquis, G., and R. D. Hyndman (1992). Geophysical support for aqueous fluids in the deep crust: seismic and electrical relationships. *Geophysical Journal International* 110 (1): 91-105.

Marshall, D.J., and T. R. Madden (1959). Induced polarisation, a study of its causes. *Geophysics* XXIV (4): 790-816.

Marti, A (2014). The Role of Electrical Anisotropy in Magnetotelluric Responses : From Modelling and Dimensionality Analysis to Inversion and Interpretation. *Surveys in Geophysics* 35: 179-218.

Mavko, G. M., and A. Nur (1978). Effect of non-elliptical cracks on compressibility of rocks. *Journal of Geophysical Research* 83 (NB9): 4459-4468.

Mendelson, K., and M. Cohen (1982). The effect of grain anisotropy on the electrical properties of sedimentary rocks. *Geophysics* 47 (2): 257-263.

Moorkamp, M., A. G. Jones, and S. Fishwick (2010). Joint inversion of receiver functions, surface wave dispersion, and. *Journal of Geophysical Research* 115: B04318.

Newman, G., M. Commer, and J. Carazzone (2010). Imaging CSEM data in the presence of electrical anisotropy. *Geophysics* 75 (2): F51-F61.

North, L., A. Best, J. Sothcott, and L. Macgregor (2013). Laboratory determination of the full electrical resistivity tensor of heterogeneous carbonate rocks at elevated pressures. *Geophysical Prospecting* 61: 458-470.

North, L., and A. Best (2014). Anomalous electrical resistivity anisotropy in clean reservoir sandstones. *Geophysical Prospecting* 62: 1315-1326.

Nordsiek, S., and A. Weller (2008). A new approach to fitting induced-polarization spectra. *Geophysics* 73 (6): F235-F245.

Okay, G., P. Leroy, A. Ghorbani, P. Cosenza, C. Camerlynck, J. Cabrera, N. Florsch, and A. Revil (2014). Spectral induced polarization of clay-sand mixtures: Experiments and modeling. *Geophysics* 79 (6): E353-E375.

Pelton, W.H., S.H. Ward, P.G. Hallof, W.R. Sill and P.H. Nelson (1978). Mineral discrimination and removing of inductive coupling with multifrequency IP. *Geophysics* 43: 588-609.

Prasad, M., and M. Manghnani (1997). Effects of pore and differential pressure on compressional wave velocity and quality factor in Berea and Michigan sandstones. *Geophysics* 62 (4): 1163-1176.

Pride, S. R., J. G. Berryman, M. Commer, S. Nakagawa, G. A. Newman, and D. W. Vasco (2017). Changes in geophysical properties caused by fluid injection into porous rocks: analytical models. *Geophysical Prospecting* 65 (3): 766-790.

Rathore, J S, E Fjaer, R M Holt, and L Renlie (1994). P- and S- wave anisotropy of synthetic sandstone with controlled crack geometry. *Geophysical Prospecting* 43: 711-728.

Revil, A. (2012). Spectral induced polarization of shaly sands: Influence of the electrical double layer. *Water Resources Research* 48: W02517.

Revil, A. (2013). Effective conductivity and permittivity of unsaturated porous materials in the frequency range 1 mHz-1GHz. *Water Resources Research* 49 (1): 306-327.

Revil, A., and L. Cathles (1999). Permeability of shaly sands. *Water Resources Research* 35 (3): 651-662.

Revil, A., J.D. Eppehimer, M. Skold, M., Karaoulis, L. Godinez and M. Prasad (2013). Low-frequency complex conductivity of sandy and clayey materials. *Journal of Colloid and Interface Science* 398: 193-209.

Revil, A., and N. Florsch (2010). Permeability of shaly sands. *Geophysical Journal International* 181 (3): 1480-1498.

Revil, A., and P. Glover (1998). Nature of surface electrical conductivity in natural sands, sandstones, and clays. *Geophysical research letters* 25 (5): 691-694.

Revil, A., K. Koch, and K. Holliger (2012). Is it the grain size or the characteristic pore size that controls the induced polarization relaxation time of clean sands and sandstones? *Water Resources Research* 48 (5): 1-7.

Revil, A., A. Binley, L. Mejus, and P. Kessouri (2015). Predicting permeability from the charactaristic relaxation time and intrinsic formation factor of complex conductivity spectra. *Water Resources Research* 51: 6672-6700.

Revil, A., W. Woodruff, and M. Prasad (2013). Complex conductivity tensor of anisotropic hydrocarbon-bearing shales and mudrocks. *Geophysics* 78 (6): D403-D418.

Robion, P., F. Humbert, J. C. Colombier, S. Leghay, and D. Frizon de Lamotte (2012). Relationships between pore space anisotropy and anisotropy of physical properties of

silicoclastic rocks from the Corbi??res-Minervois fold-and-thrust-belt (north-east Pyrenees, France). *Tectonophysics* 576-577: 63-77.

Saeger, E H, and S A Shapiro (2002). Effective velocities in fractured media: a numerical study using rotated staggered finite-difference grid. *Geophysical Prospecting* 50: 183-194.

Sayers, Colin M, and Mark Kachanov (1995). Microcrack-induced elastic wave anisotropy of brittle rocks. *Journal of Geophysical Research* 100 (B3): 4149-4156.

Schlumberger, C., M. Schlumberger, and E. G. Leonardon (1934). Some Observations Concerning Electrical Measurements in Anisotropic Media and Their Interpretations. *Trans, AIME* 110: 159-182.

Schmitt, D. R. 2015. Geophysical Properties of the Near Surface Earth: Seismic Properties. Edited by G. Schubert. *Treatise in Geophysics (2nd edition)* (Elsiver) 11 (2): 43-87.

Schwarz, G. (1962). A theory of the low frequency dielectric dispersion of colloidal particles in electrolyte solutions. *Journal of Physical Chemistry* 66: 2626-2635.

Scott, J. (2006). The origin of the observed low-frequency electrical polarization in sandstones. *Geophysics* 71 (5): G235-G238.

Scott, J., and R. Barker (2003). Determining pore-throat size in Permo-Triassic sandstones from low-frequency electrical spectroscopy. *Geophysical Research Letters* 30 (9): 1-4.

Sen, P., C. Scala, and M. Cohen (1981). A self-similar model for sedimentary rocks with application to the dielectric constant of fused glass beads. *Geophysics* 46 (5): 781-795.

Slater, Lee, and David P. Lesmes (2002). Electrical- hydraulic relationships observed for unconsolidated sediments. *Water Resources Research* 38 (10): 1-13.

Stesky, R M. (1985). Compressional and shear velocities of dry and saturated jointed rock: a laboratory study. *Geophysical Journal of the Royal astronomical Society* 83: 239-262.

Stesky, R M. (1986). Electrical conductivity of brine-saturated fractured rock. *Geophysics* 51 (8): 1585-1593.

Stesky, R. M., and S. S. Hannan (1989). A new theory for the static contact between rough, unmated surfaces in non-elastically deforming rock and its implications for rock friction. *Journal of Structural Geology* 11 (7): 787-798.

Sumner, J S. (1976). *Principles of induced polarization for geophysical exploration.* Elsiver.

Tarasov, A., and K. Titov (2007). Relaxation time distribution from time domain induced polarization measurements. *Geophysics Journal International* 170 (1): 31-43.

Titov, K., V. Komarov, V. Tarasov, and A. Levitski (2002). Theoretical and experimental study of time domain-induced polarization in water-saturated sands. *Journal of Applied Geophysics* 50: 417-433.

Tranter, T. G., M. Tam, and J. T. Gostick (2018). The Effect of Cracks on the In-plane Electrical Conductivity of PEFC Catalyst Layers. *Electroanalysis* 30: 1-6.

Ustra, Andrea, Alberto Mendonca, Ntarlagiannis Dimitrios, and Lee D. Slater (2016). Relaxation time distribution obtained by Debye decomposition of spectral induced polarisation data. *Geophysics* 81 (2): E129-E138.

Vacquier, V., C. Holmes, P. Kitzinger, and M. Lavergne (1957). Prospecting for groundwater by induced polarization. *Geophysics* 22: 660-687.

Van Genuchten, M.Th. (1980). A closed-form equation for predicting the hydraulic conductivity of unsaturated soils. *Soil Science Society of America* 892-898.

Vanhala, H. (1997). Mapping oil-contaminated sand and tillwith the spectral induced polarization (SIP) method. *Geophysical Prospecting* 45: 303-326.

Vinegar, H.J., M.H. Waxman (1984). Induced Polarization of shaley sands. *Geophysics* 49: 1267-1287

Walsh, J B. (1981). Effect of pore pressure and confining pressure on fracture permeability. *International Journal of Rock Mechanics and Mining Sciences and Geomechanics Abstracts* 18: 429-435.

Walsh, J. B., and M. A. Grosenbaugh (1979). New model for analysing the effect of fractures on compressibility. *Journal of Geophysical Research* 84 (NB7): 3532-3536.

Wamsley, P., and R. Fisher (2017). Determination of the resistivity anisotropy of orthorhombic materials via transverse resistivity measurements. *Review of Scientific Instruments* 88 (4): 9.

Wang, M., J. Lui, and S. Chen (2008). Electric potential distribution in nanoscale electroosmosis: from molecules to continuum. *Molecular Simulation* 34 (5): 509-514.

Wang, Z., and L. J. Gelius (2010). Electric and elastic properties of rock samples: a unified measurement approach. *Petroleum Geoscience* 16 (2): 171-183.

Wang, Zhong, Leiv Gelius, and Fan-Nian Kong (2009). Simultaneous core sample measurements of elastic properties and resistivity at reservoir conditions employing a modified triaxial cell- a feasibility study. *Geophysical Prospecting* 57: 1009-1026.

Wang, Z., R. Wang, T. Li, and M. Zhao (2017). The combined effects of pore structure and pore fluid on the acoustic properties of cracked and vuggy synthetic rocks. *Journal of Petroleum Science and Engineering* 156: 202-211.

Wang, Z., D. Schmitt, and R. Wang (2015). Does wettability influence seismic wave propagation in liquid saturated porous rocks. *Geophysical Journal International* 203: 2182-2188.

Waxman, M. H., and L. J.M. Smits (1968). Electrical Conductivities in Oil-Bearing Shaly Sands . *Society of Petroleum Engineers Journal* 107-122.

Weller, A., and L. Slater (2015). Induced polarisation dependence on pore space geometry: Empirical observations and mechanistic predictions. *Journal of Applied Geophysics* 123: 310-315.

Weller, A., L. Slater, and S. Nordsiek (2013). On the relationship between induced polarization and surface conductivity: Implications for petrophysical interpretation of electrical measurements. *Geophysics* 78 (5): D315-D325.

Weller, A., Z. Zhang, L. Slater, S. Kruschwitz and M. Halisch (2016).Induce polarization and pore radius – A discussion. *Geophysics* 81 (5): D519-D526.

Williams, Kenneth H., Andreas Kemna, Michael J. Wilkins, Jennifer Druhan, Evan Arntzen, Lucie N'Guessan, Philip E. Long, Susan S. Hubbard, and Jillian F. Banfield (2009). Geophysical monitoring of coupled microbial and geochemical processes during simulated subsurface bioremediation. *Environmental Science and Technology* 43: 6717-6723.

Woodruff, W. F., A. Revil, and C. Torres-Verdin (2014). Laboratory determination of the complex conductivity tensor of unconventional anisotropic shales. *Geophysics* 79 (5): E183-E200.

Woodruff, W. F., A. Revil, and M. Prasad (2015). Measurements of elastic and electrical properties of an unconventional organic shale under differential loading. *Geophysics* 80 (4): D363-D383.

Wong, T. F., J. T. Fredrich, and G. D. Gwanmesia (1989). Crack aperture statistics and pore space fractal geometry of westerly granite and rutland quartzite: Implications for an elastic contact model of rock compressibility. *Journal of Geophysical Research Solid Earth* 94 (B8): 10267-10278.

Wyllie, M. R.J., A. R. Gregory, and L. W. Gardner (1956). Elastic wave velocities in heterogenious and porous media. *Geophysics* 21 (1): 41-70.

Wyllie, M R., and W. D. Rose (1950). Some theoretical considerations related to the quantitative evaluation of the physical charactaristics of reservoir rock from electrical log data. *Journal of Petroleum Technology* 2 (4): 105-118.

Yam, H. (2011). *CO2 rock physics: A laboratory Study.* MSc Thesis, Edmonton: Department of Physics, University of Alberta.

Yan, P., T. Kalscheuer, P. Heidin, and M. A.G. Juanatey (2017). Two-dimensional magnetotelluric inversion using reflection seismic data as constraints and application in the COSC project. *Geophysical Research letters* 44 (8): 3554-3563.

Zaitsev, V. Y., A. V. Radostin, E. Pasternak, and A. Dyskin (2017). "Extracting shear and normal compliances of crack-like defects from pressure dependences of elastic-wave velocities." *International Journal of Rock Mechanics and Mining Sciences* 97: 122-133.

Zhang, L., J. Ba, L. Fu, J. M. Carcione, and C. Cao (2019). Estimation of pore microstructure by using the static and dynamic moduli. *International Journal of Rock Mechanics and Mining Sciences* 113: 24-30.

Zimmermann, E., A. Kemna, J. Berwix, W. Glaas, H. Munch, and J. Huisman (2008). A high-accuracy impedance spectrometer for measuring sediments with low polarizability. *Measurement Science and Technology* 19: 9pp.

Zisser, N., and G. Nover (2009). Anisotropy of permeability and complex resistivity of tight sandstones subjected to hydrostatic pressure. *Journal of Applied Geophysics* 68 (3): 356-370.

Zisser, N., A. Kemna, and G. Nover (2010). Relationship between low-frequency electrical properties and hydraulic permeability of low-permeability sandstones. *Geophysics* 75 (3): E131-E141.